Cu_2O Heterojunction Photovoltaics

Thesis by

Yulia Tolstova

In Partial Fulfillment of the Requirements for the
Degree of
Doctor of Philosophy

California Institute of Technology
Pasadena, California
2016
Defended May 27, 2016

To my mother

Acknowledgements

This thesis would not have been possible without the contributions of many, many people.

First, I would like to thank my adviser, Harry Atwater, for being so incredibly inspiring and supportive for all these years. There were so many times when I went into Harry's office feeling defeated and walked out actually wanting to get back to work. I am also grateful for having the freedom to explore and make (so many) mistakes.

I would like to thank my thesis committee — Professors Bill Johnson, Julia Greer, and Austin Minnich — for their helpful feedback and taking the time to review my thesis.

My research experience would not have been the same without mentorship from several people. Ali Ghaffari has been an incredible source of support, vacuum system knowledge, and optimism. I want to thank Carol Garland for her mentorship at the TEM and also giving me the opportunity to help teach the TEM lab. I learned so much from this experience (including the best recipe for brownies).

There are many people at Caltech whose assistance is essential to the success of many research projects: Mike Roy (CCE Instrument shop), Rick Gerhart (Glass shop), Rick Germond (Facilities stockroom), Joe Haggerty and Ali Kiani (GALCIT shop), Mike Walsh (Biology electronics shop), Chi Ma (GPS SEM facility), Nils Asplund (KNI), Bruce Brunschwig, and all the GLAs at the MMRC.

I would like to thank all the members of the Earth Abundant semiconductor project with whom I've had the privilege of working: Samantha Wilson, Amanda Shing, Greg Kimball, Davis Darvish, Chengxiang Xiang, Naomi Coronel, Jeff Bosco, and Faisal Tajdar. It was great to collaborate with several scientists from Dow, including Rebekah Feist, Robert Wright, Melissa Mushrush, Manish Sharma, Jim Stevens, Pete Nickias, and Steve Rozeveld. I would also

like to acknowledge my WAVE student Raymond Blackwell. I would like to especially thank Stefan Omelchenko for collaboration and friendship and sharing pots of tea during the last several years.

Many other members of the Atwater, Lewis, and other groups have been incredibly helpful throughout the years. Chris Chen, Hal Emmer, Rebecca Saive, Sunita Darbe, Jung-Shun Huang, Ron Grimm, Nick Strandwitz, Seokmin Jeon, Ragip Pala, Victor Brar, Woochul Jung, Anna Beck, Kate Fountaine, Ana Brown, Carissa Eisler, Cris Flowers, John Lloyd, Dagny Fleishman, Michelle Sherrott, Krishnan Thyagarajan, and so many others. Thank you all for making my time at Caltech what it was. I would also like to acknowledge the denizens of Watson 250, it was a pleasure to share an office with you guys: Seyoon Kim, Colton Bukowsky, Nick Batara, Muhammad Alam (thank you for providing a broader perspective on life after grad school and lots of useful advice). My daily experiences would not have been the same without the help of Tiffany Kimoto, Jennifer Blankenship, Christy Jenstad, Lyra Haas, Mabel Chik, Michelle Aldecua, Connie Rodriguez, Liz Jennings, and Lyann Lau. Your support has made all our lives easier.

Lastly, I would like to thank my family and friends for their support, especially: Amanda "Woman" McNally and my second family (Roberta, Mike, Frank, Nick) — thank you for being there for me all these years; Jennifer Buz, I'm lucky to have had you by my side through high school, college, and grad school; Yinglu Tang, for somehow surviving as my roommate for 4 years and cooking delicious food together. I am most indebted to my mother, Irena Tolstova, for making so many sacrifices to make my life easier, and my grandfather, Nikolai Ostapenko, for taking care of me even from far away. And lastly I want to thank my partner Eliot Hijano for being patient and supportive during the best and worst of times.

Yulia Tolstova
April 2016
Pasadena, CA

Abstract

Cuprous oxide (Cu_2O) is an earth abundant semiconductor that has several promising photovoltaic properties, including high absorption in the visible range, high minority carrier diffusion length, and high majority carrier mobility. Cu_2O can be easily synthesized by oxidation of copper foils in air. One important advantage that makes Cu_2O highly relevant to today's solar cell markets dominated by crystalline silicon is its wide bandgap of 1.9 eV at room temperature, which makes it an ideal candidate for a top cell in tandem with a crystalline silicon bottom cell. The detailed balance efficiency of such a device exceeds 44%.

In this work we aim to address several issues that have limited Cu_2O solar cell efficiency. We address the intrinsic p-type nature and chemical instability of Cu_2O by pairing it with an appropriate n-type heterojunction partner Zn(O,S), which allows us to achieve devices with open circuit voltages exceeding 1 V. We identify presence of a current blocking layer and reduce it, which results in more than doubling the short circuit current to exceed 5 mA/cm^2. Light beam induced current measurements shed light on some of the issues inherent to polycrystalline Cu_2O solar cells, including grain dependent collection and current losses due to presence of grain boundaries.

In order to address the issues affecting Cu_2O made by thermal oxidation we also develop thin film growth of Cu_2O by molecular beam epitaxy on several substrates including MgO and heteroepitaxial noble metal templates that act as ohmic back contacts. These studies culminate in achievement of the first Cu_2O/Zn(O,S) solar cells incorporating an absorber layer grown by molecular beam epitaxy.

Contents

List of Figures

List of Tables

List of Publications

Portions of this thesis have been drawn from the following publications:

Y. Tolstova, S. T. Omelchenko, and H. A. Atwater, "Light beam induced current characterization of polycrystalline Cu_2O solar cells," *in preparation.*

Y. Tolstova, S. T. Omelchenko, R. E. Blackwell, A. M. Shing, and H. A. Atwater, "Analysis of polycrystalline Cu_2O photovoltaic devices incorporating Zn(O,S) buffer layers," *in preparation.*

Y. Tolstova, S. T. Omelchenko, A. M. Shing, and H. A. Atwater, "Heteroepitaxial growth of Pt and Au thin films on MgO single crystals by bias-assisted sputtering," *Scientific Reports*, 6 (2016) 23232.

Y. Tolstova, S. S. Wilson, and H. A. Atwater, "Single phase, single orientation Cu_2O (1 0 0) and (1 1 0) thin films grown by plasma-assisted molecular beam epitaxy," *Journal of Crystal Growth* 410 (2015) 77-81.

Y. Tolstova, S. S. Wilson, S. T. Omelchenko, N. S. Lewis, and H. A. Atwater, "Molecular Beam Epitaxy of Cu_2O Heterostructures for Photovoltaics," *42nd IEEE PVSC* (2015).

S. S. Wilson, J. P. Bosco, Y. Tolstova, D. O. Scanlon, G. W. Watson, and H. A. Atwater "Interface stoichiometry control to improve device voltage and modify band alignment in ZnO/Cu_2O heterojunction solar cells," *Energy and Environmental Science*, 7 (2014), 3606-3610.

Chapter 1

Introduction

1.1 Basics of photovoltaics

A basic solar cell consists of a junction between a p-type (or hole-doped) and an n-type (or electron-doped) semiconductor, as shown in Figure 1.1. In thermal equilibrium, the potential difference between the two sides will cause holes from the p-type region to move into the n-type region, and electrons from the n-type region to move into the p-type region, establishing a depletion (or space-charge) region. At equilibrium, the electric field established by the space charge region will balance the diffusion of carriers.

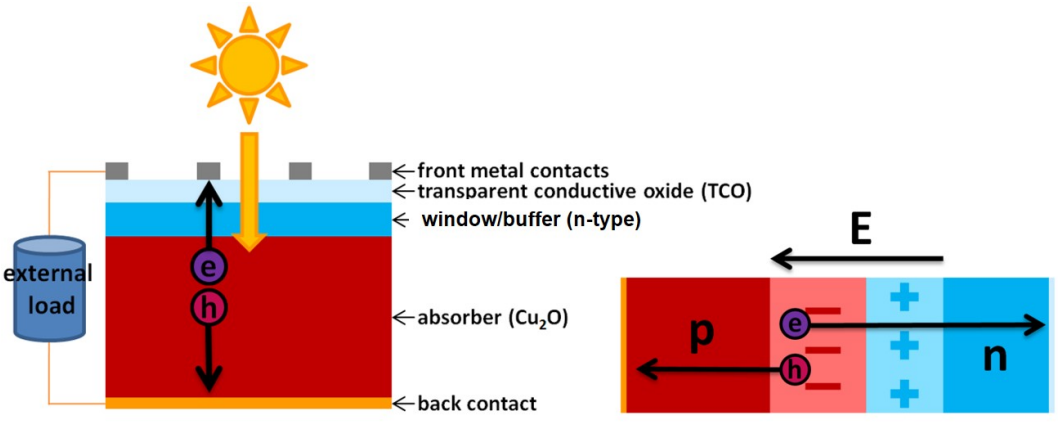

Figure 1.1: Basic solar cell schematic.

Absorption of photons with energies above the band gap will excite an electron from the valence band of the semiconductor to the conduction band, leaving behind a hole. These generated charges will then diffuse until they enter the space charge region, where electrons will be swept by the electric field towards the n-type layer and holes will be swept towards the p-type layer and eventually to the contacts to drive an external load.

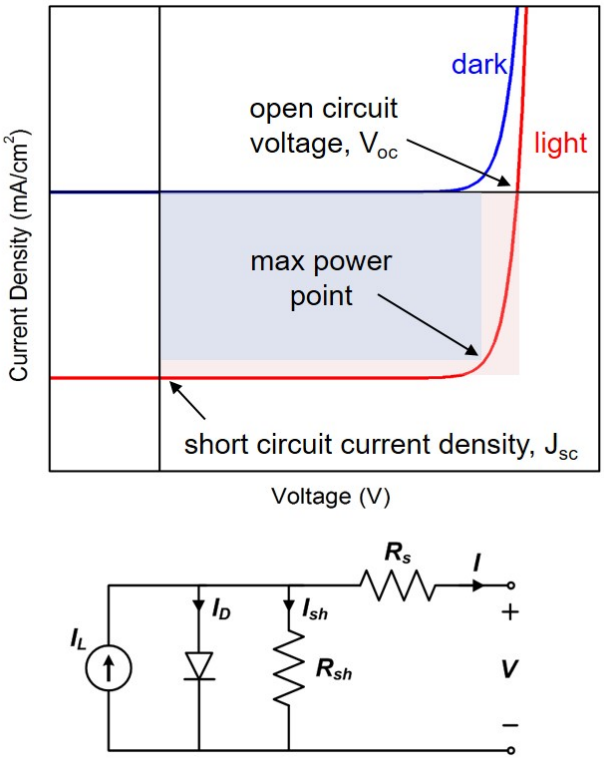

Figure 1.2: Current-voltage behavior and equivalent circuit of a solar cell.

Figure 1.2 shows the current-voltage behavior of a solar cell and illustrates some important parameters that define solar cell performance. The open-circuit voltage (V_{OC}) is related to the band offsets between the n and p-type materials as well as the quality of the interface. The short circuit current (J_{SC}) is a measure of the photocurrent collected by the solar cell. In addition, the fill factor (FF) is a measure of the squareness of the J-V curve and is typically reduced by high series resistance (R_s) or low shunt resistance (R_{sh}).

1.2 Motivation for Cu_2O photovoltaics

Cuprous oxide (Cu_2O) was one of the first known semiconductors, but its potential application in photovoltaics was not seriously explored until alternative materials for solar first garnered attention during the oil crisis of the 1970s. [1] Many of Cu_2O's photovoltaic properties were characterized at that time, however device efficiencies were limited by several factors, many of which are still pertinent today. The second wave of research on earth-abundant solar materials came during the silicon crisis of the mid-2000s; however, current trends seem to indicate that silicon is going to remain the dominant player in the solar industry. One interesting advantage held by semiconductors like Cu_2O that have large bandgaps is that instead of competing with the dominant silicon technologies, the addition of a Cu_2O top cell to make a tandem cell stack can potentially improve upon the performance of a crystalline silicon bottom cell. In such a tandem configuration, the Cu_2O solar cell needs to have a power conversion efficiency above 8%. As we will see shortly, this is already a reality, which makes Cu_2O a highly relevant material. The detailed balance efficiency limit for a single junction Cu_2O solar cell has been calculated to exceed 20% and for a dual junction with a crystalline Si bottom cell, this efficiency is 44% [2].

Cu_2O is composed of earth-abundant and non-toxic elements and can be easily fabricated by oxidizing copper foils in air and cooling within the thermodynamic region of stability of the Cu_2O phase. A thermodynamic phase diagram is shown in Figure 1.3. A more detailed phase diagram of the high temperature region can be found in [3]. This method of preparation has yielded material with high absorption coefficient in the visible region, hole mobilities exceeding 100 $cm^2V^{-1}s^{-1}$, and minority carrier diffusion lengths in excess of 10 μm. [4, 5]

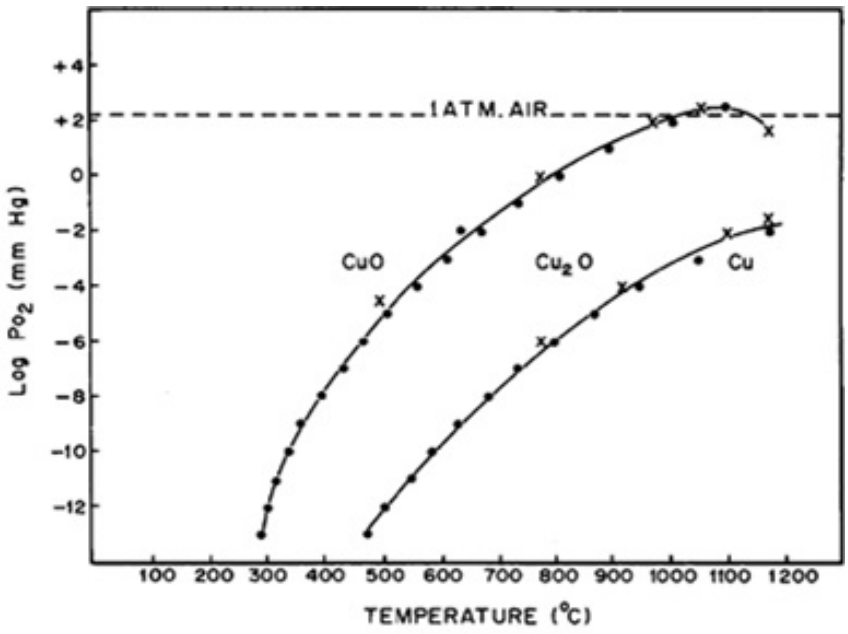

Figure 1.3: Thermodynamic phase diagram of Cu-O. [1]

1.3 Energy band alignment

Several important issues have impeded production of high efficiency Cu_2O devices. One of the main challenges stems from the intrinsically p-type nature of Cu_2O due to copper vacancy doping. This requires a heterojunction partner material with a suitable energy band alignment in order to enable charge separation in the device.

The low electron affinity of Cu_2O (3.2 eV) limits potential heterojunction candidates to those with similarly low conduction band edge energies. In addition, the small heat of formation of Cu_2O (-170.7 kJ/mol) [6] means that the surface is susceptible to reduction and oxidation. Prior work shows that a stoichiometric Cu_2O interface produces the highest efficiency devices [2, 7]. It is thus imperative to find a heterojunction partner material that has an appropriate band offset and allows formation of a stoichiometric Cu_2O interface. Much of previous work has paired Cu_2O with ZnO; however, the staggered type II band alignment between these two materials fundamentally limits the

V_{oc} to less than 600 mV, which is significantly less than the entitlement for Cu_2O of 1.5 V.

Recently, Ga_2O_3 [8, 9, 10], Zn(O,S) [2, 11, 12], and $Zn_{1-x}Ge_xO$ [13] have emerged as suitable heterojunction partner candidates for Cu_2O due to their favorable band alignment, and solar cells with open circuit voltages exceeding 1 V have been fabricated. Currently, the highest efficiency device, which incorporates a polycrystalline Cu_2O absorber and a $Zn_{1-x}Ge_xO$ buffer layer, is 8.1% [13].

What does an ideal band alignment look like for a heterojunction? Figure 1.4 shows idealized energy band positions for the components (a) in isolation, and (b) after bringing the materials together after equilibration of the Fermi level, E_F. In order to maximize the open circuit voltage of the device, the conduction band of the buffer layer needs to be slightly above the conduction band of Cu_2O, such that ΔE_C is approximately 0.3 eV or less. This ensures that electrons generated in the Cu_2O by photon absorption can travel through the buffer and window layers towards the front contact without experiencing too much of a barrier. At the same time a slightly positive ΔE_C will help minimize surface recombination between the Cu_2O and buffer. In the case of the valence band offset, ΔE_V, we want the valence band of the Cu_2O to sit much higher than the valence band of the buffer, which will block holes from traveling into the buffer and causing recombination.

The heterojunction partners that have so far produced high open circuit voltages, namely Ga_2O_3 and Zn(O,S), have demonstrated a slight positive conduction band offset and a large negative valence band offset. [11, 15, 16]

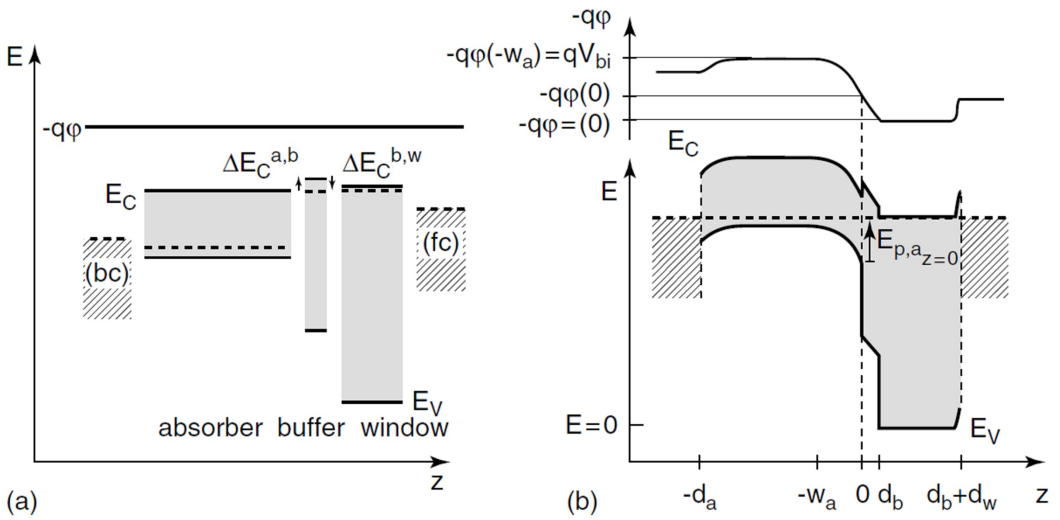

Figure 1.4: Idealized energy band positions for a heterojunciton solar cell with a p-type absorber (a) in isolation, and (b) after bringing the materials together. [14]

1.4 Scope of this thesis

This thesis seeks to identify and address the issues that limit photovoltaic efficiency of Cu_2O solar cells.

- **Development of Cu_2O growth by molecular beam epitaxy**: We have identified several undesirable properties in bulk thermally oxidized wafers, as well as sputtered and electrodeposited thin films of Cu_2O. One way to overcome these issues is to use molecular beam epitaxy, which is a UHV thin film growth technique that can potentially produce high quality material by allowing precise control of growth parameters. In chapter 2, we develop this technique to grow single phase, single orientation thin films of Cu_2O initially on MgO single crystals, which are the closest lattice matched substrates and therefore ideal for epitaxy. However, to make a solar cell we need to be able to contact the back surface of the Cu_2O film and since photolithography recipes have not been studied in great detail for this material we instead focus on growing

it heteroepitaxially on an ohmic contact material. In chapter 3, we use bias-assisted sputtering to develop such templates. In chapter 4, we explore growth of Cu_2O by molecular beam epitaxy on these templates.

- **Study of Cu_2O/Zn(O,S) heterojunctions**: In chapter 5 we explore the suitability of Zn(O,S) as a heterojunction partner using Cu_2O bulk thermally oxidized wafers. We identify sources of high series resistance, namely $ZnSO_4$, which forms at the interface between Cu_2O and Zn(O,S) at low temperature. The formation of this undesirable, yet thermodynamically favorable phase can be mitigated by depositing at elevated substrate temperatures, and we find that 100°C is the temperature at which the short circuit current and the efficiency are maximized. We also conduct light beam induced current measurements, which show that bulk polycrystalline Cu_2O devices exhibit grain-dependent photocurrent collection and identify grain boundaries are photocurrent sinks.

- **First devices incorporating MBE-grown Cu_2O absorber**: We conclude chapter 5 by fabricating and analyzing the first Cu_2O/Zn(O,S) solar cells made using molecular beam epitaxy to grow the Cu_2O absorber layer.

- **Appendices: Oxide MBE and PLD user guides**: Much of my time was spent using, fixing, and maintaining the oxide molecular beam epitaxy and the pulsed laser deposition systems. In an attempt to transfer this knowledge I have written user guides for both of these systems.

Chapter 2

Molecular Beam Epitaxy of Cu_2O Thin Films on MgO

2.1 Introduction to Molecular Beam Epitaxy

The term "epitaxy" refers to growth of a crystalline film on a crystalline substrate, such that the crystallographic structure and orientation of the substrate influences that of the film. [17, 18] Furthermore, growth of material A on substrate B is referred to as "heteroepitaxy." Molecular beam epitaxy is a physical vapor deposition technique which is typically carried out in ultra-high vacuum (UHV), i.e. at pressures below 10^{-9} Torr. The source material is typically thermally evaporated from a solid or liquid elemental source, forming a "molecular beam" that settles on the substrate. [19, 20, 21] When reactive deposition of materials is necessary, process gases or plasma sources can be added to the system. In the case of experiments detailed in this thesis, an RF atom source is used to partially split O_2 molecules into monatomic oxygen using an RF plasma. These oxygen atoms can then travel to the substrate and react to form oxides.

Figure 2.1 shows the basic layout of the system used in this thesis. The system was home built by R. T. Brewer. [22]. A detailed procedure for operation of this instrument is presented in Appendix A. Samples are loaded into the load lock and pumped down using a small turbo-drag pump. The samples are then transferred into the main chamber, which is actively pumped by a cryogenic pump operating at 11 K. The chamber is equipped with a residual gas analyzer (RGA), which detects and quantifies the gaseous species present in the chamber. The Cu source is a high temperature effusion cell with a pyrolytic boron nitride conical crucible filled with 6N pure Cu metal pellets. The vapor pressure of Cu is low in the solid phase, so the cell needs to be heated above 1200°C to achieve an appreciable Cu flux.

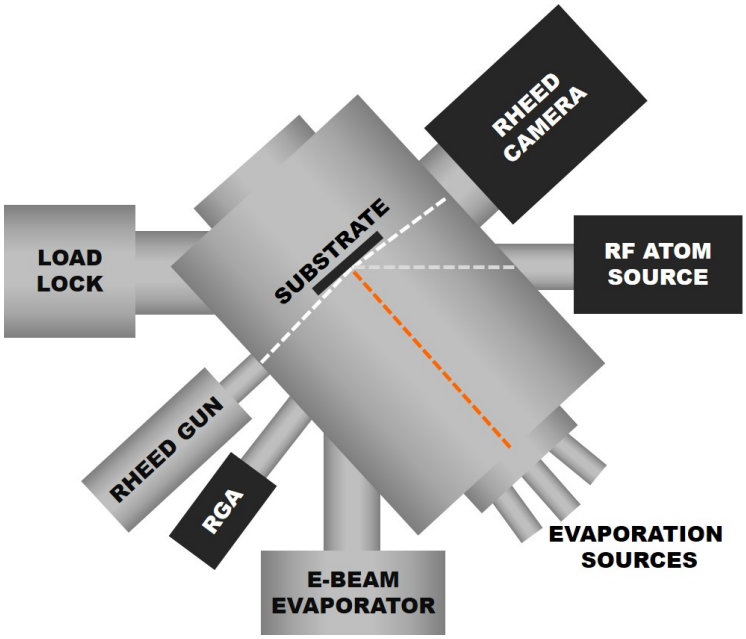

Figure 2.1: Schematic of plasma-assisted MBE chamber.

2.1.1 Reflection high energy electron diffraction

One of the most powerful *in situ* characterization techniques available in a molecular beam epitaxy system is reflection high energy electron diffraction

(RHEED). The system consists of a focused electron beam of 15 - 20 keV energy that is incident on the sample at a grazing angle θ, as shown in Figure 2.2, and a CCD camera that records the diffraction pattern incident on a phosphor screen. Diffracted intensity is seen when the reciprocal lattice of the surface material crosses the Ewald sphere. The resulting surface diffraction pattern is very useful for determining the surface structure of both the substrate and the growing film.

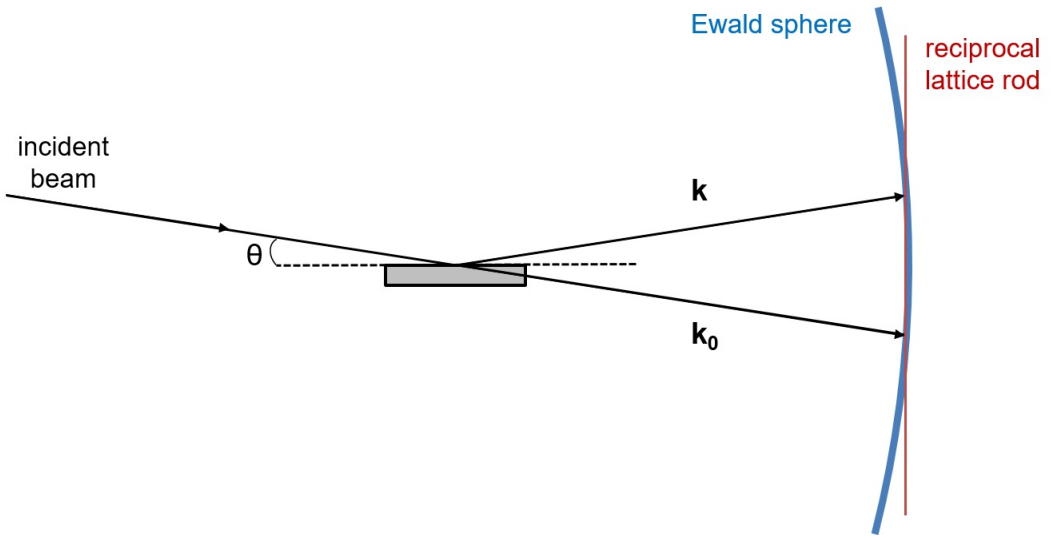

Figure 2.2: Ewald sphere construction of RHEED geometry.

Figure 2.3 shows the features typically seen in RHEED patterns. An amorphous surface would not show any features besides a diffuse scattering of electrons. A polycrystalline sample will show a RHEED pattern consisting of rings because the reciprocal space of a polycrystalline sample is a set of concentric spheres, which, when crossing the Ewald sphere will appear as rings. A rough but oriented crystalline surface will produce a three-dimensional transmission electron diffraction pattern, similar to ones seen in TEM. When the film grows in islands this is the most common pattern, as we will see later in this chapter. The reciprocal space of a perfect surface consists of infinite rods in the direction normal to the surface. These rods are broadened by thermal vibrations

and other defects in the crystal. In addition, broadening of the Ewald sphere itself can occur as a result of energy variations in the electron beam. Thus the RHEED pattern of a single crystal consists of streaks. The streaks will be shortened by presence of an non-zero offcut of the sample surface or atomic steps on the surface, with larger steps producing longer streaks.

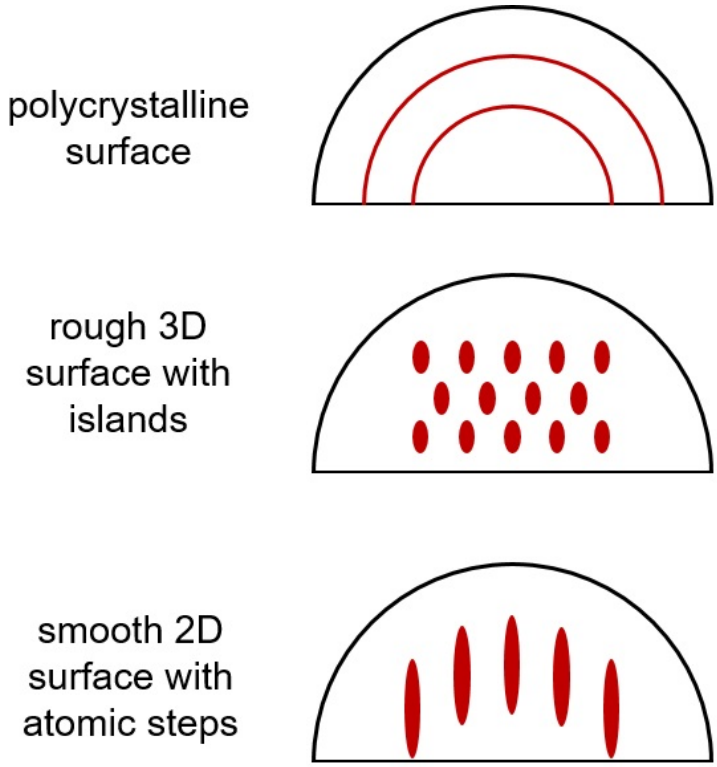

Figure 2.3: Effect of film structure on RHEED pattern.

2.1.2 Thin film growth modes

The mode of growth of an epitaxial film depends on several factors, including the surface structure and quality of the substrate, lattice mismatch between the two materials, growth conditions such as temperature and flux, and energies associated with all the possible interfaces. There are three basic growth modes that can occur, and they are shown schematically in Figure 2.4. The layer-by-layer, also known as Frank-van der Merwe, or two-dimensional mode, typically

occurs when the surface energy of the substrate is higher than the interface energy between the film and substrate and consequently the film atoms have a strong preference for binding to the substrate. This mode is also characterized by the presence of fast diffusion of surface atoms such that they can find the lowest energy sites. The two-dimensional growth mode is typically preferred because it yields the highest crystalline quality and smooth surfaces.

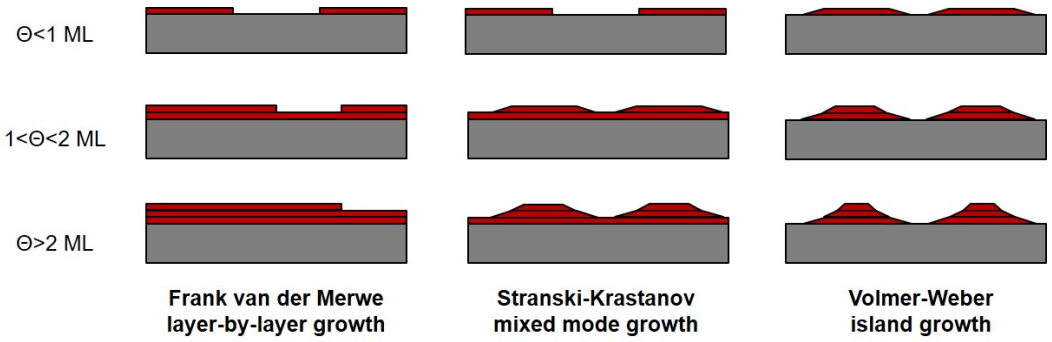

Figure 2.4: Thin film growth modes. Θ refers to monolayer (ML) coverage of the surface.

Initial layer-by-layer growth can turn into island growth in the Stranski-Krastanov growth mode. This typically occurs due to a change in energetics beyond a critical layer thickness, which is related to the chemical potential of the film as well as strain. Once layer-by-layer growth breaks down, the subsequent layers form from the nucleation and coalescence of islands. The third growth mode is the island, or Volmer-Weber mode. This arises when the film atoms are more likely to bind to each other than to the substrate. Eventually, as growth proceeds, these islands will merge to form a rough film.

2.2 Growth of Cu_2O on MgO

Arguably the strongest motivation for Cu_2O in photovoltaic applications is its relatively large band gap of 2.1 eV (and exciton gap at 1.9 eV), which make it a promising candidate as a top cell in a tandem solar cell combined with a crystalline silicon bottom cell. In order for such a tandem cell to improve upon existing Si cell efficiency, a Cu_2O cell efficiency approaching 10% is required [23]. The development of such a structure would require synthesis by thin film methods, and molecular beam epitaxy (MBE) provides precise control over many deposition parameters and generally yields high quality material. MBE synthesis of Cu_2O on MgO substrates has been demonstrated using pure atomic oxygen [24, 25, 26], however no reports of a diluted oxygen plasma have been made to date. Also, growth on MgO (1 1 0) surface has been reported by sputtering [27] and pulsed laser deposition [28], but not by MBE. DFT calculations [29] show that the Cu_2O (1 1 0) surface has the lowest energy, so it is reasonable to assume that a substrate that promotes growth in this direction may foster Cu_2O phase stability over a larger range of deposition parameters, and this is consistent with results of this work. We compare the structural properties of Cu_2O films grown using a pure oxygen atmosphere to films grown using a 90%Ar/10%O_2 premix, on (1 0 0) and (1 1 0) orientations of MgO.

2.2.1 Experimental Setup

Thin films of Cu_xO were grown in a custom molecular beam epitaxy system equipped with an Oxford RF atom source. RF atom sources dissociate molecular species (such as O_2 or N_2) into atomic species for increased reactivity while minimizing ionic species which typically have high kinetic energies and

are associated with creation of point defects. Ionic components of the plasma that escape the atom source were further filtered out by ion deflection plates. Thus the current of gas species was composed of atomic argon and/or oxygen. Oxygen (Air Liquide, 99.9999% purity) partial pressure was varied between 1×10^{-7} and 1×10^{-5} Torr. For growths with argon/oxygen premix (Air Liquide, 99.9999% purity, 10.0% oxygen, balance argon), the gas partial pressure of argon was correspondingly an order of magnitude higher. The presence of argon allowed for stability of the plasma, while decreasing the partial pressure of reactive oxygen species. Partial pressures were monitored by a residual gas analyzer (RGA). Atom source plasma power was varied between 100 and 200 W and plasma optical emission voltage ranged from 1 V to 3 V during film deposition. Plasma emission voltage corresponds to the intensity of light emitted from the plasma and correlates with the efficiency of dissociation of the molecular gas into its atomic components. The growth chamber base pressure was $< 3 \times 10^{-9}$ Torr. Copper metal (6N, Alfa Aesar) was evaporated from a high temperature effusion cell at a temperature ranging from 1250-1300 °C. Cu_xO was formed reactively at the surface of the substrate kept at a temperature ranging from 400-650 °C. MgO was chosen as a substrate because it is the closest lattice matched commercially available single crystal; it is also refractory, transparent, and non-conductive, which makes it suitable for a variety of electrical and optical characterization techniques. MgO substrates were cleaned *in situ* by annealing at deposition temperature for an hour and subsequently plasma cleaned for 10 minutes. *In situ* reflection high energy electron diffraction (RHEED, with electron beam energy of 20 keV) was used to confirm cleanliness and orientation of the substrate surface and monitor film structure at various stages of the growth. *Ex situ* characterization included high resolution x-ray diffraction (HRXRD, Panalytical XPert Pro), transmis-

sion electron microscopy (TEM, FEI Tecnai F30 with S-TWIN objective, 300 keV electron energy), and atomic force microscopy (AFM, Asylum Research MFP 3D). TEM cross sections were prepared using standard focused ion beam milling on an FEI Versa 3D).

2.2.2 Growth using pure oxygen plasma

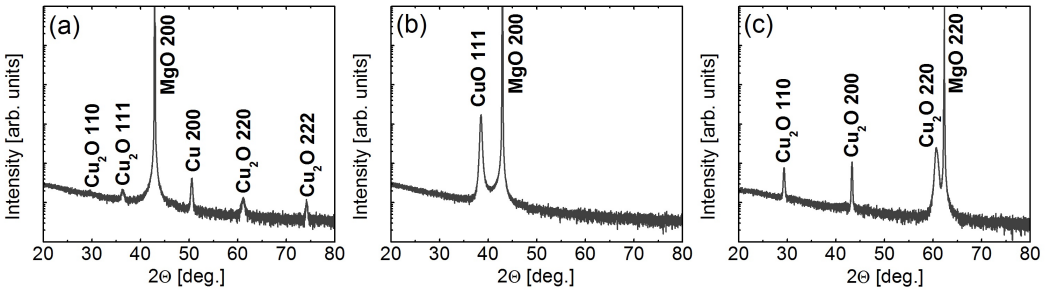

Figure 2.5: HRXRD spectra of Cu_xO films grown on MgO (1 0 0) at (a) 1×10^{-6} Torr and (b) 5×10^{-6} Torr oxygen, both cases corresponding to presence of undesirable phases and (c) pure phase Cu_2O film grown on MgO (1 1 0) at 9×10^{-6} Torr.

Growth of Cu_xO on MgO was initially studied by varying oxygen partial pressure (using pure oxygen gas) and substrate temperature, while fixing the Cu effusion cell temperature at 1275 °C, atom source plasma power at 100 W, and plasma optical emission voltage at 1 V (which corresponds to the lower range of stability of the plasma source). As illustrated in Figure 2.5 (a-b), the growth window for the Cu_2O phase on MgO (1 0 0) was found to be too narrow to reproducibly grow single phase films. Raising the pressure of oxygen by only half an order of magnitude, while maintaining otherwise identical growth parameters and low oxygen plasma power, changed the film composition from a mixture of Cu_2O and Cu to CuO. Figure 2.5 (c) shows that single-phase epitaxial growth of Cu_2O on MgO (1 1 0) is achievable within a narrow range of deposition parameters using pure oxygen. It should be noted that using pure oxygen, two orientations of Cu_2O, namely the (1 1 0) and (2 0 0)

are commonly present.

The difficulty of growing single phase, single orientation Cu_2O on MgO (1 0 0) has been demonstrated before, and it is known that the (1 1 0) MgO orientation is more amenable to unidirectional Cu_2O epitaxy, and regardless of substrate orientation, growth of Cu_2O in the (1 1 0) direction is usually preferred compared to (1 0 0). Although reasons for this are still debated and different epitaxial relationships have been reported [24, 25, 30, 31], density functional theory calculations show that the Cu_2O (1 1 0):CuO surface has the lowest energy, and generally the nonpolar Cu_2O (1 1 0) surfaces have lower energies than the polar Cu_2O (1 0 0) surfaces [29]. Lattice mismatch seems to be less important than surface energy in determining the preferential growth direction [24].

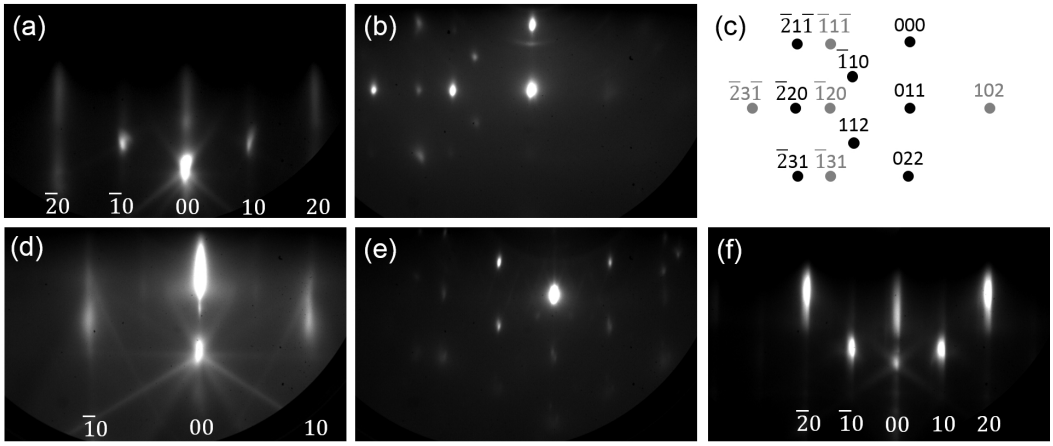

Figure 2.6: RHEED images of Cu_2O growth on MgO using pure oxygen plasma. (a) Plasma cleaned MgO (1 0 0) surface along the [1 1 0] azimuth, (b) 100 nm of Cu_2O showing growth initiates and persists in the Volmer-Weber or island regime and the pattern is a superposition of the Cu_2O [1 1 $\bar{1}$] and [2 1 $\bar{1}$] zone axis transmission patterns; (c) indexing of diffraction spots in (b) along [1 1 $\bar{1}$] zone axis (black) and [2 1 $\bar{1}$] zone axis (gray); (d) plasma cleaned MgO (1 1 0) surface along the [1 1 1] azimuth, (e) 10 nm of Cu_2O along [1 1 $\bar{1}$] again initiates with island growth (for spot indexing refer to Fig. 2.6 (f)), (f) after 100 nm of Cu_2O viewed along [1 1 $\bar{1}$], islands merge into a smooth film with steps, as evidenced by a streaky pattern.

Figure 2.6 (a-c) shows RHEED patterns for growth of Cu_2O on MgO (1 0 0).

Growth of Cu_2O initiates with islands corresponding to two symmetrically equivalent variants of the Cu_2O (1 1 0) surface such that the pattern in Figure 2.6 (b) is a superposition of the Cu_2O $[1\,1\,\bar{1}]$ and $[2\,1\,\bar{1}]$ zone axis transmission patterns. Figure 2.6 (c) shows the schematic indexing of the diffraction spots. These results are consistent with the literature results of Cu_2O growth on MgO (1 0 0) [24, 31]. Figure 2.6 (b) (d-f) shows that growth of Cu_2O on MgO (1 1 0) starts in the Volmer-Weber or island regime, and the islands eventually merge to form a smooth and continuous film with some surface disorder as evidenced by the streaky nature of the pattern [32]. Note that the RHEED pattern corresponds to only a single orientation of the film, which indicates that nucleation of the second orientation is not spatially uniform and most likely predominates away from the center of the sample.

Despite some success in growing single phase Cu_2O films on the (1 1 0) MgO orientation, reproducibility was still an issue due to the limited oxygen partial pressure growth window. The partial pressure of oxygen needed to produce a stable plasma in the RF atom source needed to exceed 1×10^{-6} Torr, and the growth window for pure Cu_2O was found to be close to this limit for pure oxygen. There are several ways to enable growth of single phase, single crystalline orientation Cu_2O, which include raising substrate temperature, raising the Cu flux, and using a different oxidant. The substrate temperature was already approaching the limits of the system, and higher growth temperature is generally undesirable in terms of substrate compatibility and cost. Raising the Cu flux by increasing source filament temperature is also problematic in terms of operation costs and effusion cell lifetime. Instead, oxygen partial pressure was diluted using an inert balance gas (90%Ar/10%O_2 premix) to enable stable plasma stability at lower oxygen partial pressures.

2.2.3 Growth using 90%Ar/10%O_2 plasma

Figure 2.7 shows HRXRD data of various films of Cu_xO grown on (a) MgO (1 0 0) and (b) MgO (1 1 0). The XRD peak intensities are lower compared to those of Figure 2.5 because film thickness is substantially reduced using a 90%Ar/10%O_2 gas mixture. Growth rate using pure oxygen at 550 °C was measured by x-ray reflectivity to be 100 nm/hr, while growth using the Ar/O_2 gas mixture was measured to be 20 nm/hr. For growth on MgO (1 0 0), Cu_2O

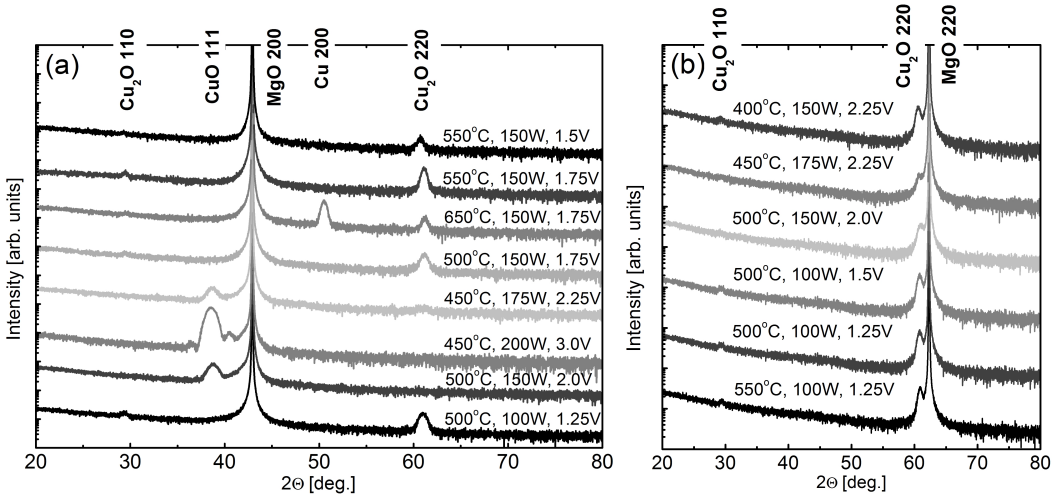

Figure 2.7: HRXRD spectra of Cu_xO grown on (a) MgO (1 0 0) and (b) MgO (1 1 0) using argon-oxygen plasma. Spectra are labeled with deposition temperature, plasma power, and plasma optical emission voltage.

films are obtained at low plasma optical voltages and powers, and intermediate substrate temperatures. Plasma emission voltage, which is a function of gas flow rate and plasma power, was found to better correlate with the epitaxial film quality than either the gas flow rate or the plasma power. The epitaxial growth phase diagram in Figure 2.8 (a) summarizes these results. As shown in Figure 2.7, films grown on MgO (1 1 0) all have a single orientation in the (1 1 0) Cu_2O direction, for a wide range of plasma parameters and substrate temperatures.

Figure 2.9 (a-c) shows representative RHEED patterns for pure Cu_2O

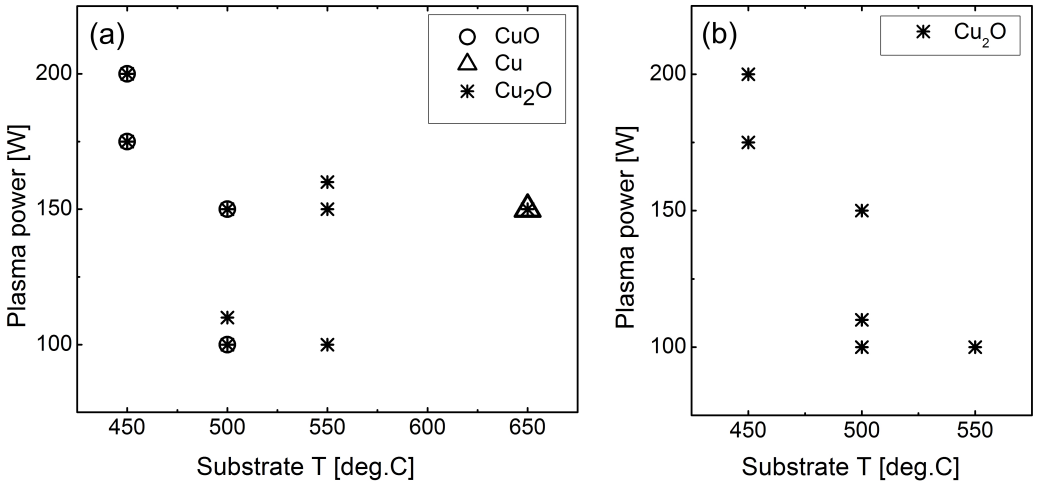

Figure 2.8: MBE regime phase diagram for growth of Cu_xO on (a) MgO (1 0 0) and (b) MgO (1 1 0), using argon-oxygen plasma.

grown on MgO (1 0 0); growth starts in the Volmer-Weber island growth mode and after 60 nm starts to smooth out into a continuous film as evidenced by the appearance of streaks. Growth on the MgO (1 1 0) surface is shown in Figure 2.9 (d-f). In contrast to films grown using pure oxygen that exhibited two variants of the Cu_2O (1 1 0) orientation, films grown using Ar/O_2 exhibit only one variant, at least within the region probed by the RHEED electron beam. Looking at the $[1\,1\,\bar{1}]$ Cu_2O azimuth in Figure 2.9 (e), all spots can be indexed to the corresponding transmission diffraction pattern shown in Figure 2.9 (f), and no extra spots corresponding to the $[2\,1\,\bar{1}]$ azimuth are present. The pattern looks very similar to that of Figure 2.6 (e). Growth remains 3-dimensional possibly due to the fact that the film thickness is not large enough to completely cover the MgO surface, as seen in AFM and TEM examination of the film in Figure 2.10.

The epitaxial relationship of Cu_2O (1 1 0) on MgO (1 1 0) was confirmed directly by TEM, as shown in Figure 5.5. The selected area diffraction pattern in Figure 5.5 (b) shows the Cu_2O lattice directly overlaps the MgO lattice and the film appears to be strained.

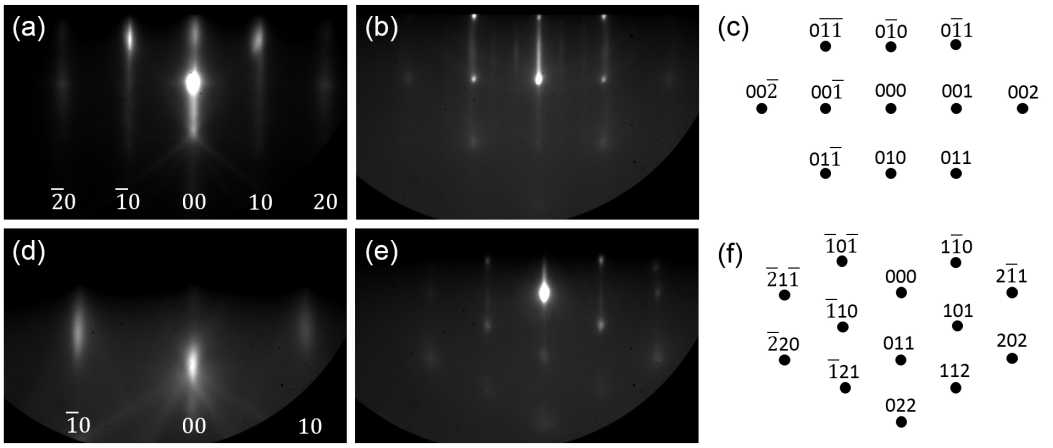

Figure 2.9: RHEED images of Cu_2O growth on MgO using argon-oxygen plasma. (a) Plasma cleaned MgO (1 0 0) surface along the [1 1 0] azimuth, (b) 60 nm of Cu_2O proceeds with island growth shown here along the [1 0 0] azimuth, and islands start to merge into a smooth film, as evidenced by the appearance of streaks, but growth remains 3-dimensional, which may be attributed to lower film thickness than in the pure oxygen films. (c) schematic spot indexing along [100] zone axis of Cu_2O. (d) Plasma cleaned MgO (1 1 0) surface along the [1 1 1] azimuth, (e) 60 nm of Cu_2O shown here along the $[1\,1\,\bar{1}]$ azimuth showing growth initiates and persists in the island regime, (f) schematic spot indexing along the $[1\,1\,\bar{1}]$ zone axis of Cu_2O.

Conclusion

Single phase, single orientation Cu_2O thin films have been grown on MgO by plasma-assisted molecular beam epitaxy using both pure oxygen and argon-oxygen gas mixtures. Growth using argon-oxygen opens up the stability window of the Cu_2O phase by giving access to lower partial pressures of oxygen while still maintaining a stable plasma. The film growth rate using argon-oxygen is reduced compared to pure oxygen; however film mosaicity and texture are also reduced, yielding a film with increased crystallinity. The results of this work facilitate the development of high quality absorber layers for an epitaxial Cu_2O solar cell device.

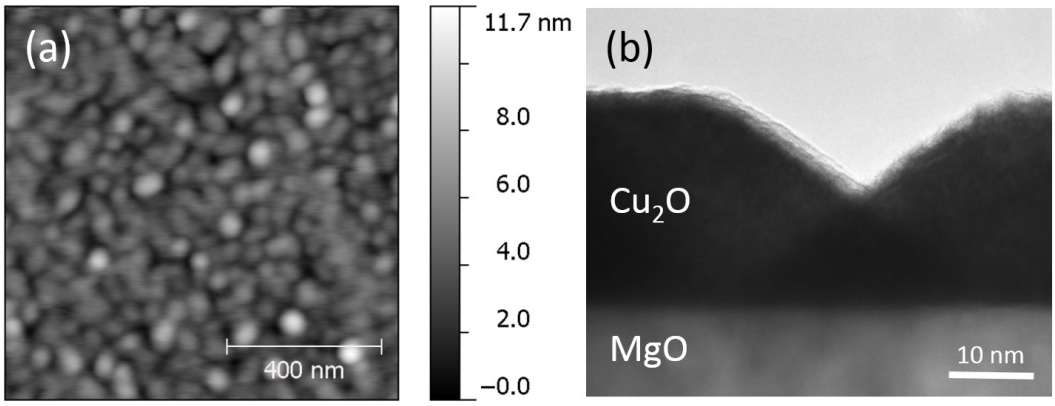

Figure 2.10: (a) AFM image of a 20 nm Cu_2O film grown on MgO (1 1 0) using an argon-oxygen plasma showing island-type film morphology. (b) TEM micrograph showing cross sectional morphology of Cu_2O on MgO (1 1 0) confirming island-growth regime.

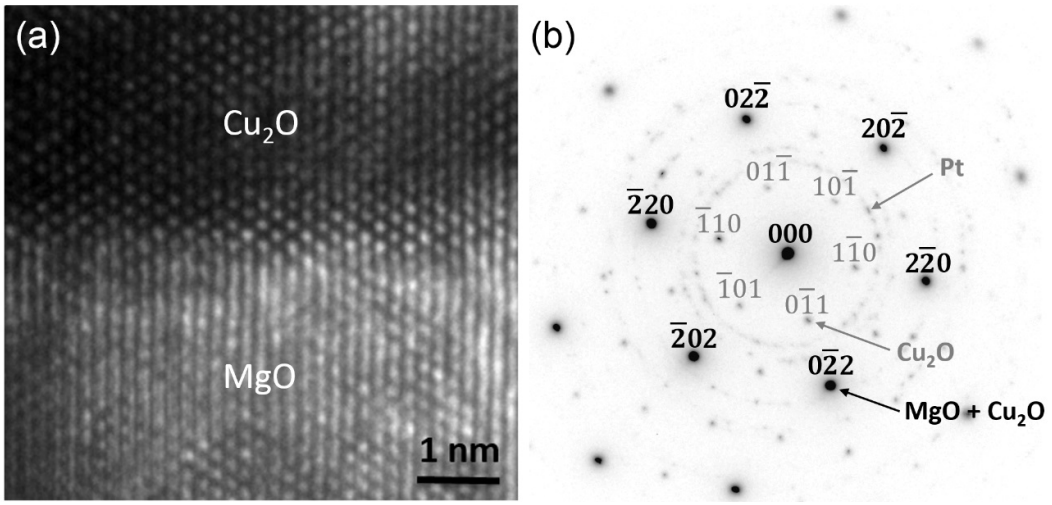

Figure 2.11: (a) High resolution cross-sectional TEM of (1 1 0) Cu_2O on MgO (1 1 0) viewed down the [1 1 1] zone axis shows epitaxial relationship between film and substrate. (b) Selected area electron diffraction pattern shows a superposition of the Cu_2O [1 1 1] and MgO [1 1 1] zone axis diffraction patterns, confirming epitaxial relationship. Note the presence of amorphous rings due to Pt protective layer.

Chapter 3

Heteroepitaxial Ohmic Templates for Cu_2O Growth

The crystallographic orientation of a metal affects its surface energy and structure, and has profound implications for surface chemical reactions and interface engineering, which are important in areas ranging from optoelectronic device fabrication to catalysis. However, it can be very difficult and expensive to manufacture, orient, and cut single crystal metals along different crystallographic orientations, especially in the case of precious metals. One approach is to grow thin metal films epitaxially on dielectric substrates. In this work, we report on growth of Pt and Au films on MgO single crystal substrates of (1 0 0) and (1 1 0) surface orientation for use as epitaxial templates for thin film photovoltaic devices. We develop bias-assisted sputtering for deposition of oriented Pt and Au films with sub-nanometer roughness. We show that biasing the substrate decreases the substrate temperature necessary to achieve epitaxial orientation, with temperature reduction from 600 to 350 °C for Au, and from 750 to 550 °C for Pt, without use of transition metal seed layers. In addition, this temperature can be further reduced by reducing the growth rate.

Biased deposition with varying substrate bias power and working pressure also enables control of the film morphology and surface roughness.

3.1 Metal Films on Dielectric Substrates

Epitaxial growth of metal films on dielectric substrates has been the subject of intense study due to its fundamental role in technologically important applications, such as optoelectronic devices and catalysis, as well as understanding crystalline growth. Material properties can vary widely with surface structure and symmetry; however, oriented single crystals are expensive and often unavailable. Therefore, thin film growth is a promising tool to study orientation dependence of material properties without having to manufacture single crystalline samples. The purpose of this study was to develop oriented thin films of Au and Pt on MgO single crystalline substrates for use as ohmic heteroepitaxial templates for growth of semiconductor oxides, such as cuprous oxide, for thin photovoltaic applications. The requirements for a heteroepitaxial template include single film orientation and minimal surface roughness. Typically, metals like Au and Pt tend to adapt the (1 1 1) orientation when substrate effects are screened by surface contaminants, so high temperature processing and careful surface preparation are required to achieve epitaxy for other crystallographic orientations [33, 34]. In this work, we grow thin films of Au and Pt in the (1 0 0) and (1 1 0) orientations with sub-nanometer surface roughness on MgO substrates while reducing the substrate temperature necessary for epitaxy using bias-assisted sputtering.

MgO is chosen as a substrate because it is transparent, refractive, insulating, and does not react with Pt or Au, forming a clean atomically flat interface. Interface mixing reactions are a common problem with metal deposition on Si,

which can form silicide precipitates at the interface and impact the epitaxial relationship [35]. MgO is also well lattice matched to many metals with face-centered-cubic symmetry and can grow biaxially textured on amorphous substrates, providing a path for large-area deposition of oriented films on amorphous substrates [36]. The use of Fe or Ni layers to seed cube-on-cube epitaxy of Pt (1 0 0) on MgO (1 0 0) has been studied for catalysis applications [35]; however, these transition metals create deep level electronic defects in many semiconductors, and so are of less interest for photovoltaic film applications.

Nucleation and growth of Pt and Au particles on MgO has been the subject of intense study, and reviews exist on the subject [37]. Thin film growth of Pt on MgO has been explored by molecular beam epitaxy [38], pulsed laser deposition [35], electron beam evaporation [39], as well as sputtering [34, 40, 41]. Fewer studies of Au thin film growth on MgO exist [42], although nucleation of Au particles has been studied extensively [43, 44, 45].

We chose sputter deposition because it is an economical and industrially scalable process. In addition, sputtering allows for the use of substrate bias, which has been shown to have many beneficial effects on film growth, including in situ substrate cleaning and control over the energy of atoms impinging on the surface citemattox. In this report, we show that substrate bias facilitates epitaxial growth of Pt and Au films on MgO by increasing mobility of surface adatoms, influencing the number and density of nucleation sites, increasing film density, and disrupting columnar grain growth. These effects result in decreasing the substrate temperature necessary to achieve epitaxial orientation.

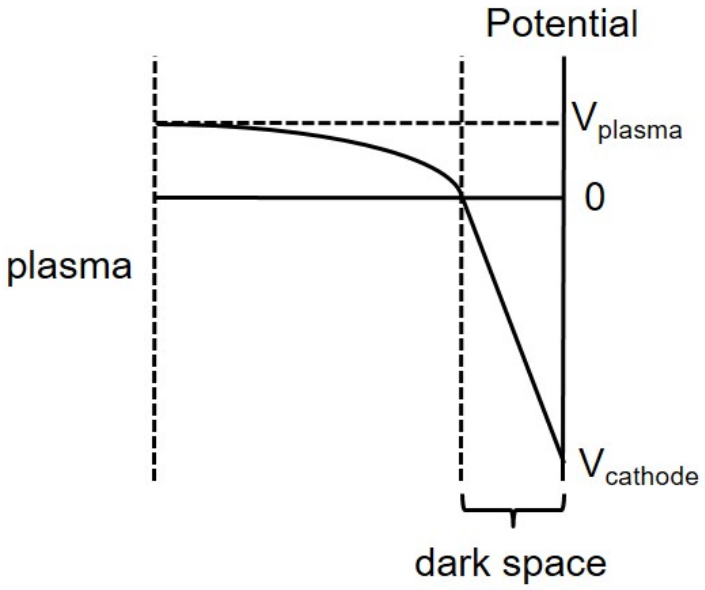

Figure 3.1: Potential variation near a cathode for a DC discharge plasma.

3.2 Bias-assisted sputtering

During sputtering, target material is ablated by bombardment of energetic ions. Ar is a common choice due to its low reactivity, low cost, and appropriate atomic weight for many elements, while Ne is better suited for sputtering lighter elements and Xe and Kr allow more efficient sputtering of heavier elements. The ejected target atoms impinge on the substrate forming a film. The substrate can be left grounded or be negatively biased using an RF power supply — RF is necessary to prevent charging in electrically insulating substrates. The purpose of negatively biasing the substrate is to modify the behavior of charged particles in the vicinity of the substrate by controlling their flux and energy. We can control and magnify the potential drop that normally occurs between the plasma, which is slightly positive, and the substrate, thus controlling the electric field that can accelerate target atoms onto the growing film. This is demonstrated schematically in Figure 3.1. In the case of RF bias, the "cathode" voltage is the DC offset of the RF waveform [46].

In order to understand the particle energies involved in sputtering, it is useful to look at the mean free path (λ), or the average distance a particle travels before colliding. The mean free path can be calculated using a simple billiard ball model [47]:

$$\lambda = \frac{1}{\sqrt{2}\pi d^2 n}$$

where d is the effective particle diameter, and n is the gas density, which can be calculated using the ideal gas law. The particle diameter of Ar is 3.64 Å [48]. The mean free path at different temperatures and pressures relevant to this study is shown in Table 3.1.

Table 3.1: Mean free path of Ar at different temperatures and pressures.

Pressure (mTorr)	25°C	350°C	550°C	700°C
1	5.2 cm	11 cm	14 cm	17 cm
3	1.7 cm	3.7 cm	4.8 cm	5.7 cm
5	1.0 cm	2.2 cm	2.9 cm	3.4 cm
7	0.7 cm	1.6 cm	2.1 cm	2.4 cm

At 1 mTorr, the mean free path of an Ar atom is approximately 5 cm at room temperature, and increases as the temperature increases [47]. Thus the mean free path is larger than the width of the dark space over which the plasma is non-neutral and the electric field is largest, which was measured to be approximately 3 cm. Thus Ar ions impinging on the substrate surface at these conditions have energies corresponding to the bias potential plus the plasma energy, which is typically on the order of 10 eV.

All of the films analyzed in this study were grown using a sputter deposition system with a base pressure of 1.3×10^{-7} Torr, shown schematically in Figure 3.2. The system is equipped with RF and DC magnetron sputtering

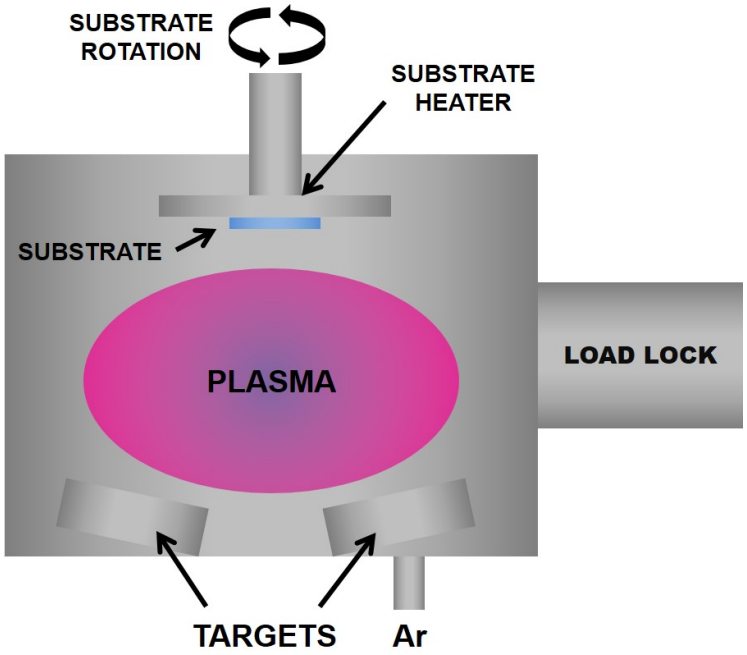

Figure 3.2: Sputtering system schematic.

sources. Substrate heating is provided by two halogen lamps situated behind the substrate chuck plate.

Single crystal MgO substrates of (1 0 0) and (1 1 0) orientation purchased commercially were annealed and cleaned in situ prior to deposition. The importance of substrate surface preparation to epitaxy cannot be overstated, particularly in the case of MgO, which is a highly hygroscopic material. Commercially available MgO crystals are typically prepared by mechanical polishing, which has been shown to amorphize the top few layers of the crystal and therefore necessitates a high temperature oxidative anneal to reconstruct the rocksalt structure and remove adventitious hydroxide. [49]

The substrates were heated to 700 °C in vacuum for an hour, and then annealed in 5 mTorr of oxygen for another hour. The temperature was then ramped down at 30 °C/minute to the deposition temperature. The substrates were plasma cleaned with a RF substrate bias of 30 W (corresponding to a bias potential of 270 eV), in 1 mTorr of 10% O_2/90% Ar gas, for 15 minutes.

This cleaning procedure was found to result in clean MgO surfaces, as evidenced by reproducibly achieving an epitaxial relationship between the film and substrate.

Pt or Au thin films were then deposited at 100 W DC power. Substrate temperature, working pressure, and RF substrate bias magnitude were varied during the study. Temperature was ramped down at a rate of 30 °C/min directly following deposition. All samples had a film thickness around 50 nm, as measured by x-ray reflectivity. Films were characterized *ex situ* using high-resolution x-ray diffractometry (HRXRD) and non-contact ambient atomic force microscopy (AFM).

3.3 Growth of Pt and Au on MgO by Bias-Assisted Sputtering

Figure 3.3 shows the orientation relationship between (a) Pt and (b) Au films grown on MgO (1 0 0) and (1 1 0) single crystals. All films in this figure were deposited with an RF substrate bias of 15W (corresponding to 180 eV impinging atom energy). For the case of Pt films, at 500 °C both MgO orientations exhibit Pt (1 1 1), which disappears completely for 550 °C, resulting in epitaxially oriented Pt films on MgO. For the case of Au films, at 300 °C, the (1 1 1) orientation has the highest intensity on both MgO (1 0 0) and (1 1 0) substrates. At 350 °C, the dominant orientation is aligned with the substrate for both (1 0 0) and (1 1 0) MgO orientations. Although we never completely eliminate the Au (1 1 1) for growth on MgO (1 0 0), the relative magnitude of this peak suggests that the fraction of (1 1 1) orientation is less than 1%. It is important to note that without substrate bias, the temperatures necessary to achieve epitaxial orientation were found to exceed 750 °C for Pt and 600 °C

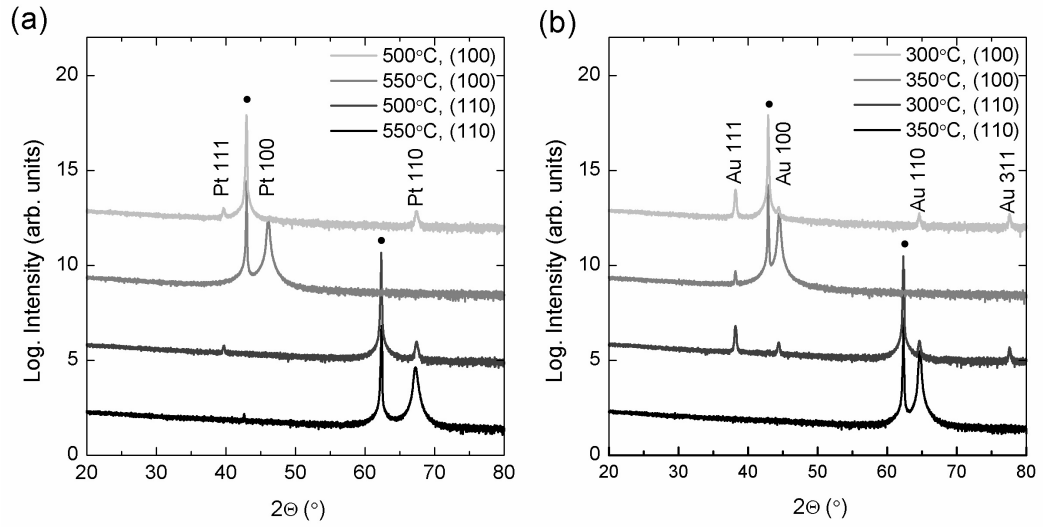

Figure 3.3: X-ray diffraction spectra of (a) Pt films on MgO (1 0 0) and (1 1 0), and (b) Au films on MgO (1 0 0) and (1 1 0). Black circles (•) indicate substrate peaks.

for Au.

Figure 3.4 (a) shows the ϕ scan of the Pt (1 0 0) film deposited at 550 °C and MgO substrate collected at a ψ tilt of 54.74° such that the {1 1 1} planes satisfy the diffraction condition. Figure 3.4 (b) shows the ϕ scan of the Pt (1 1 0) film deposited at 550 °C and MgO substrate collected at a ψ tilt of 35.26° such that the {1 1 0} planes satisfy the diffraction condition. The film is again epitaxially oriented with the substrate. The ϕ scans for Au (1 0 0) and (1 1 0) films show the same symmetry as that seen for Pt films. Based on these in-plane and out-of-plane orientation relationships, we conclude that the epitaxial relationship is cube-on-cube, i.e., (1 0 0)/(1 0 0) and (1 1 0)/(1 1 0).

In addition to being able to grow oriented Au and Pt films on MgO, it is essential for epitaxy that these films have minimum roughness. To provide a reference, AFM topography scans were used to measure the surface roughness of the MgO substrate before and after substrate cleaning by RF etching. Several literature studies suggest that an increase in substrate surface roughness can promote nucleation of the Pt (1 0 0) orientation on MgO (1 0 0) and sup-

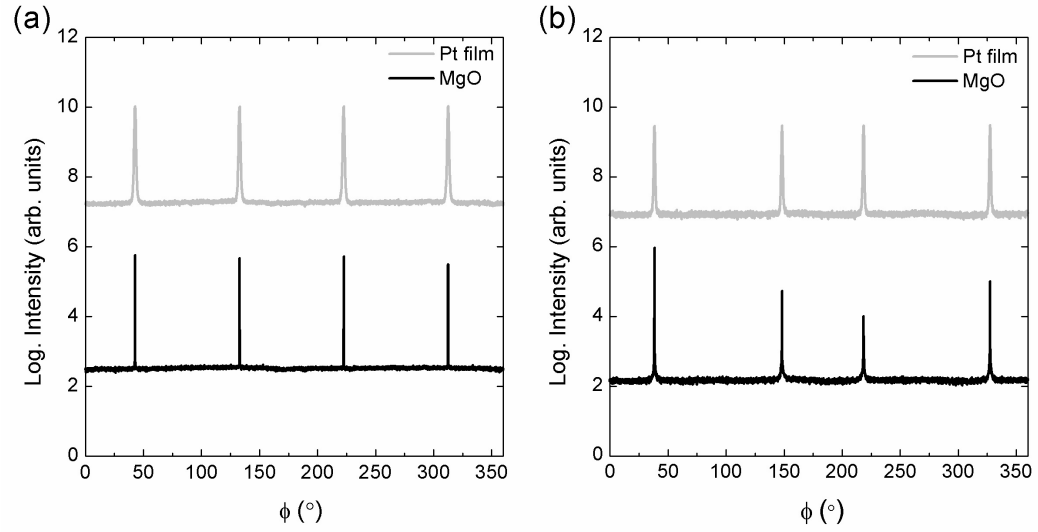

Figure 3.4: (a) ϕ scans of Pt (1 0 0) films showing Pt and MgO {1 1 1} at ψ=54.74° showing in-plane symmetry, and (b) ϕ scans of Pt (1 1 0) films showing Pt and MgO {1 1 0} at ψ=35.26°.

press nucleation of the Pt (1 1 1) orientation [50, 51]. However, in our study the root-mean-square roughness (r_{RMS}) decreased after the substrate clean. For MgO (1 0 0), r_{RMS} decreased from 0.36 nm to 0.20 nm, and for MgO (1 1 0), r_{RMS} decreased from 0.17 nm to 0.13 nm. Thus we conclude that the main result of the substrate treatment, which includes heating to 700 °C, annealing in oxygen, and plasma etching the substrate, is the removal of adventitious surface contamination instead of increase of surface roughness. Without the plasma cleaning prior to deposition, we could not reproducibly achieve epitaxial orientation until heating to very high substrate temperatures and Pt and Au (1 1 1) orientation was frequently present even in these circumstances, indicating that the absence of surface contamination is essential in achieving an epitaxial growth relationship.

Figure 3.5 shows the morphological features of the surface, as well as the root-mean-square roughness of Pt films deposited on different orientations of MgO. Figure 3.5 (a) demonstrates the effect of raising the substrate tempera-

ture while maintaining a working pressure of 3 mTorr Ar, a substrate bias of 15 W, and a target power of 100 W. At 500 °C, when based on XRD analysis the film is composed of multiple crystallographic orientations, including (1 0 0), (1 1 0), and (1 1 1), the film morphology consists of three-dimensional islands and the roughness is on the order of a few nanometers. As the temperature is increased to 550 °C, and substrate-film interactions dominate the orientation relationship resulting in epitaxial growth, the morphology of the film changes drastically. In the case of the (1 0 0) MgO surface, rectangular grains with sides oriented along ⟨1 1 0⟩ form a crossing pattern, and the films have sub-nanometer roughness of approximately 5 Å. In the case of the (1 1 0) MgO surface, rectangular grains again grow along ⟨1 1 0⟩; however, no crossing of grains is evident and they are all oriented along the same direction. Film roughness is greater for this substrate orientation, at around 1.3 nm. As the substrate temperature increases, grain size increases as well, and therefore film roughness also increases. In order to attempt to decrease the roughness of Pt films grown on MgO (1 1 0), we adjusted working pressure and substrate bias while keeping the substrate temperature at 550 °C, which was the lowest temperature at which epitaxy occurs for the given growth rate. The results, illustrated in Figure 3.5 (b), show that increasing the substrate bias from 15 W to 30 W, or increasing the working pressure from 3 mTorr to 7 mTorr, or the combination of both, decreases surface roughness of the films into the sub-nanometer range. This can be explained by the increase in the number of heterogeneous nucleation sites due to both higher pressure, and higher energy of atom bombardment. Figure 3.5 (b) also indicates that for growth on MgO (1 0 0) surfaces, increasing substrate bias while keeping working pressure constant increases grain size. Increased substrate bias effectively raises the energy of bombarding species and aids adatom mobility, which raises the probability

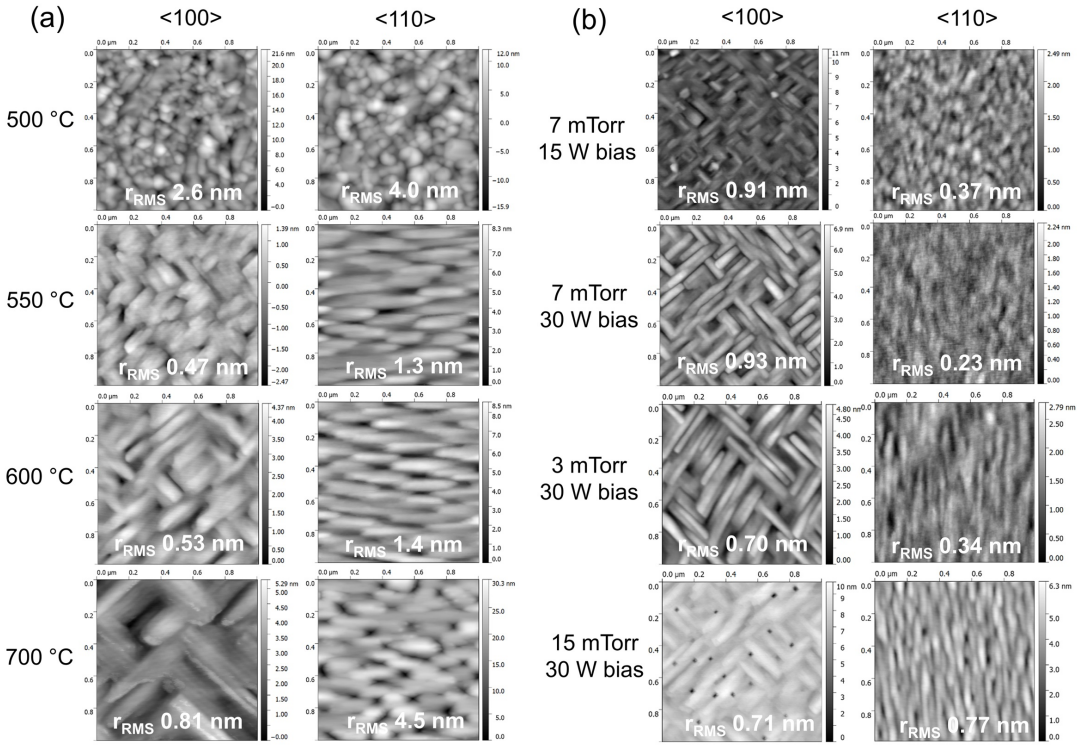

Figure 3.5: AFM topography maps of Pt films on MgO (1 0 0) and (1 1 0) deposited under different conditions. Families of directions $\langle 1\,0\,0 \rangle$ and $\langle 1\,1\,0 \rangle$ denote direction normal to the substrate surface, as well as the horizontal and vertical directions in the AFM images. (a) Effect of changing substrate temperature while maintaining a working pressure of 3 mTorr and bias of 15 W. (b) Effect of changing substrate bias and working pressure while maintaining substrate temperature at 550 °C.

of surface adatoms settling into the lowest available energy sites, thus promoting grain growth. In contrast, raising working pressure while maintaining the same substrate bias results in smaller grains due to a larger number of nucleation sites for the film and a decrease in the energy of atoms hitting the surface.

Figure 3.6 shows the morphological features of Au films grown on MgO. At 300 °C, when the film exhibits multiple orientations, the film structure is dominated by three-dimensional islands and the roughness is about 20 nm. As the temperature is increased to 350 °C, and an epitaxial relationship is established, we can achieve Au films with sub-nanometer roughness on MgO

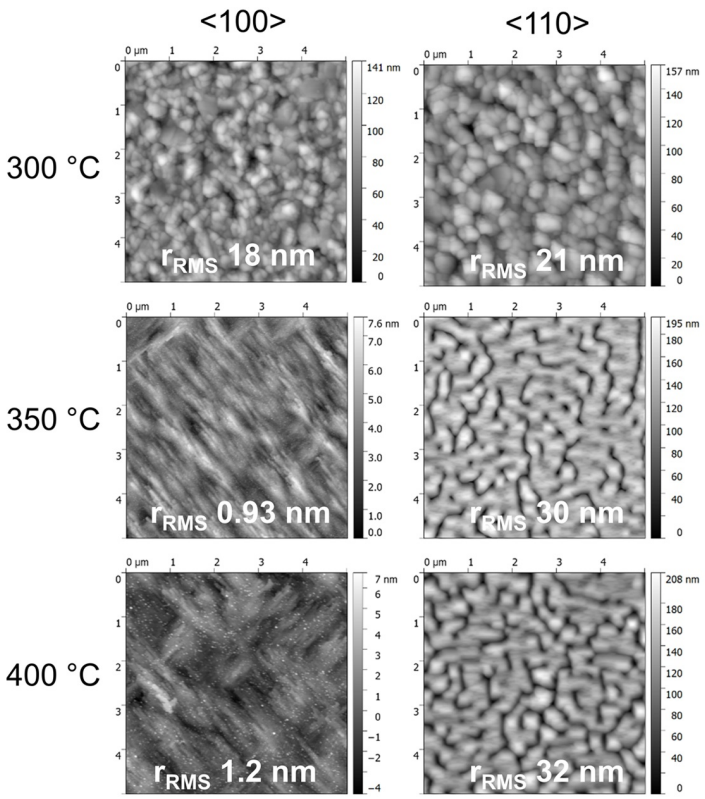

Figure 3.6: AFM topography maps of Au films on MgO (1 0 0) and (1 1 0) deposited at different substrate temperatures. All images are 5 μm by 5 μm.

(1 0 0) substrate. However, on the MgO (1 1 0) surface, Au islands do not form a continuous film, and therefore the roughness is on the order of film thickness. This is due to the high surface energy of the MgO/Au interface. Growing at higher working pressures and with larger bias did not result in smooth films appropriate for epitaxy.

Lastly, there have been literature reports showing that the substrate temperature required to achieve an epitaxial relationship decreases as the growth rate decreases [50, 51]. Therefore, we looked at the effect of deposition rate on the temperature at which the (1 1 1) orientation disappears and the cube-on-cube orientations start to dominate. Figure 3.7 demonstrates the effect of deposition rate on the orientation relationships for (a) Pt on MgO grown at 500 °C and (b) Au on MgO grown at 300 °C. The growth rate is changed

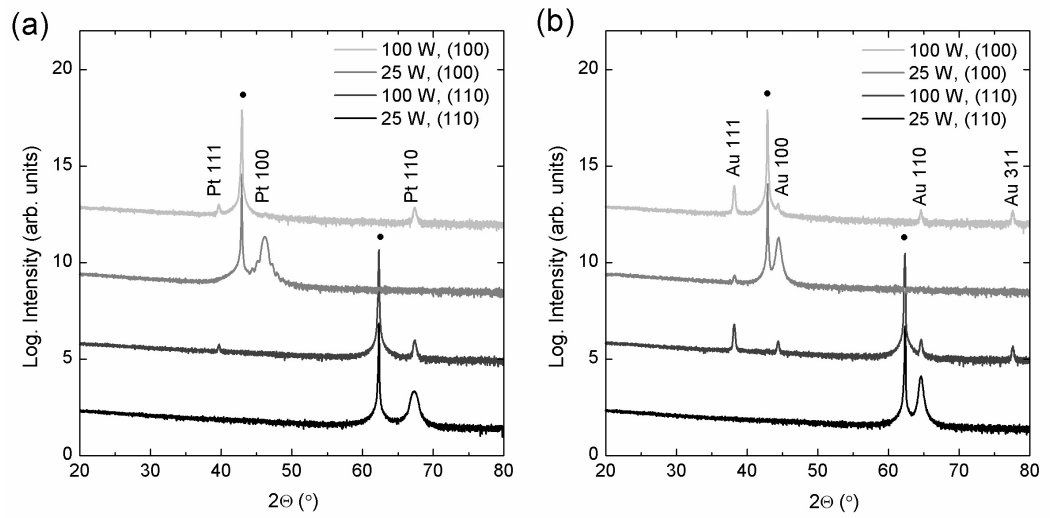

Figure 3.7: Effect of target power on the orientation relationships for (a) Pt on MgO grown at 500 °C and (b) Au on MgO grown at 300 °C. A decrease in substrate power, with a corresponding decrease in growth rate, promotes an epitaxial relationship.

by changing the target power from 100 W to 25 W, keeping other deposition parameters constant. The corresponding decrease in growth rate for Pt is from 0.8 Å/s to 0.2 Å/s, and for Au is from 1.5 Å/s to 0.4 Å/s. It is indeed the case that a lower target power, and correspondingly a lower growth rate, promotes growth of epitaxial films in both Pt and Au.

Conclusion

The main results of this work illustrate the effects of substrate preparation, temperature, and bias, on the morphology of Pt and Au thin films grown on single crystalline MgO substrates of (1 0 0) and (1 1 0) orientation. We establish an effective in situ substrate preparation and cleaning technique for MgO. Introduction of substrate bias during film growth provides a way to control film morphology and encourage an epitaxial growth relationship. Proper substrate preparation and bias during deposition allow us to decrease the temperature necessary to achieve oriented films from 600 to 350 °C for Au and from 750 to

550 °C for Pt. This temperature can be further decreased by decreasing the growth rate. We achieve sub-nanometer film roughness needed to make these films suitable as epitaxial templates for device fabrication. In addition, we illustrate the effects of changing the magnitude of substrate bias and working pressure on device morphology.

Chapter 4

Cu_2O Growth on Heteroepitaxial Ohmic Templates

4.1 MBE of Cu_xO on Pt

In this chapter, Cu_xO thin films are deposited by plasma-assisted molecular beam epitaxy (MBE) on noble metal heteroepitaxial templates, which were developed in Chapter 3. We focus this study on Pt because it produces continuous, oriented thin films with sub-nm roughness for both MgO (1 0 0) and (1 1 0) orientations. Some results on Au thin films are also included, although only the Au (1 0 0) orientation successfully produced a sub-nm continuous film. MgO is used as a heteroepitaxial template for the growth of Cu_xO heterostructures because it is a close lattice match to both FCC metals and Cu_xO and can be grown biaxially textured on an amorphous substrate [36], providing a path to dual junction cells.

Thin films of Cu_xO were deposited by plasma-assisted MBE with chamber

base pressure around 3x10^{-9} Torr, using an evaporation cell with Cu metal and a pure oxygen plasma provided by an Oxford RF Atom source. Deposition pressure during growth was kept at approximately 1.5x10^{-5} Torr oxygen, with plasma power around 150 W and plasma optical emission voltage (which correlates with the efficiency of dissociation of O_2 gas into its atomic components) kept under 1 V. These conditions were found to stabilize the Cu_xO phase. The substrates were heated to 550 °C and annealed in vacuum for 30 minutes prior to deposition of Cu_xO. Substrate temperature was kept at 550 °C during deposition. Reflection high energy electron diffraction (RHEED) with a 15 keV electron beam was used to monitor film structure in situ during growth. Films were grown for 1 hour, which resulted in a thickness of approximately 150 nm. Films were cooled in vacuum at a rate of approximately 15 °C per minute and analyzed *ex situ* using x-ray diffraction and non-contact ambient AFM. As we will show, the stability window of the Cu_2O phase needs to be re-optimized for every substrate orientation.

Figure 4.1 (a) shows the x-ray diffraction spectra of Cu_xO thin films deposited on Pt (1 0 0), which was sputtered on MgO (1 0 0). The Cu_2O film is primarily oriented in the (1 0 0) direction with some (1 1 1) orientation present. The polar (1 0 0) surface of Cu_2O is favored by the epitaxial relationship to the Pt (1 0 0) film; however, the nonpolar hkl(111) surface of Cu_2O is lower energy than the polar (1 0 0) surface [29] and is typically present as well. It may also be present due to a small amount of Pt (1 1 1) that can be seen in the x-ray diffraction data of the original Pt template. There is also a wide shoulder on the Pt (2 0 0) peak corresponding to formation of an alloy of Cu and Pt, which is expected based on the thermodynamic phase diagram in Figure 4.2. The alloy poses no issue as long as there is no shunting and the contact remains ohmic. The ohmic nature of the contact was confirmed by I-V measurement

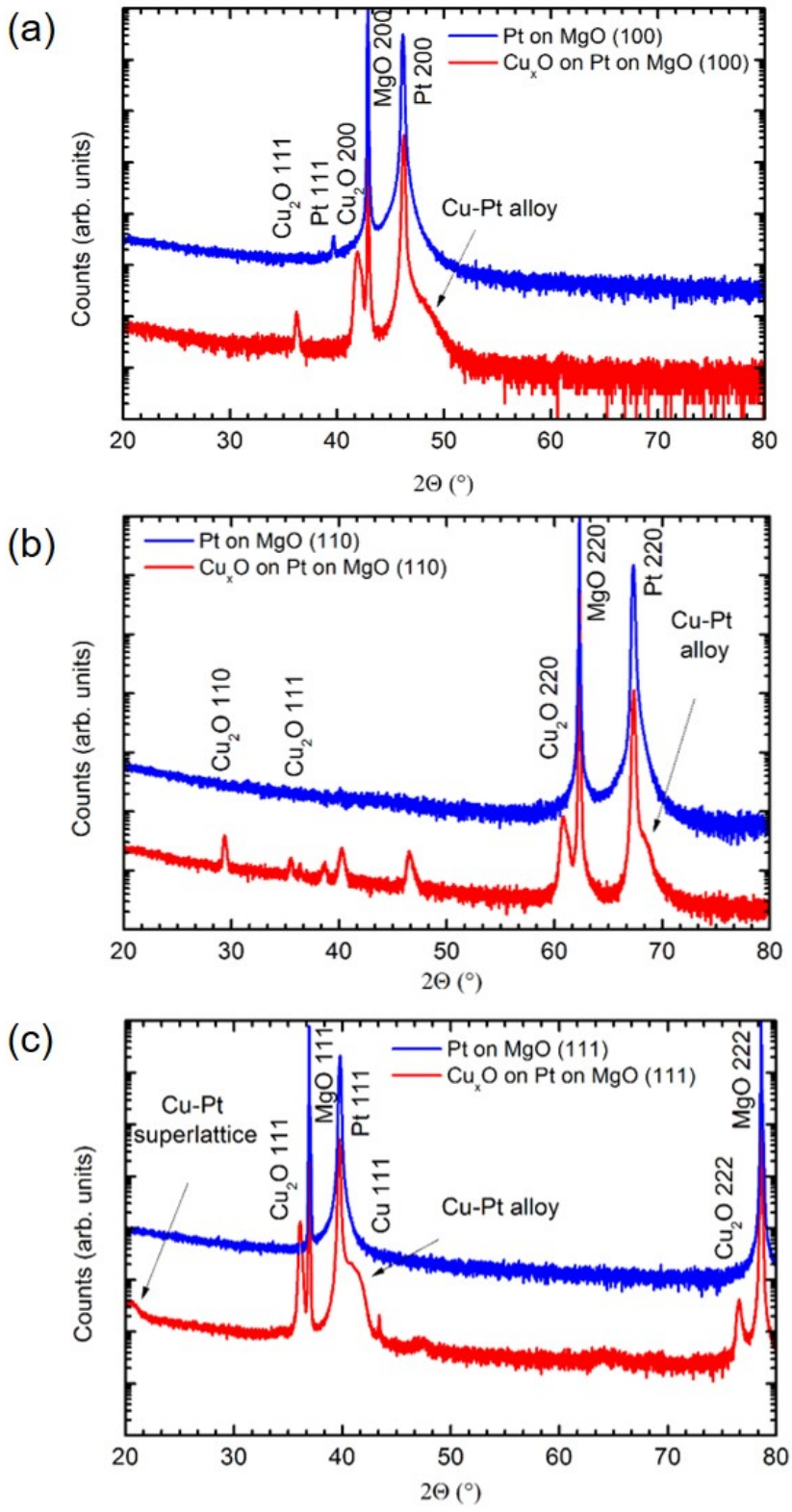

Figure 4.1: HRXRD of Cu_xO films grown on Pt heteroepitaxial templates (a) (1 0 0), (b) (1 1 0), (c) (1 1 1).

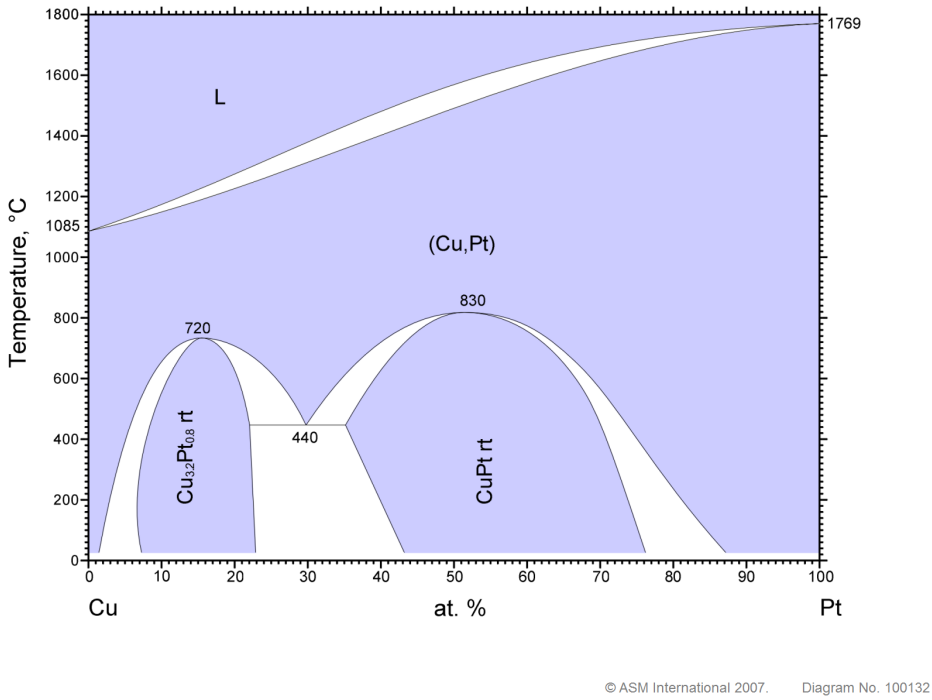

Figure 4.2: Phase diagram of Cu-Pt system. [52]

with the Cu_2O film resistance on the order of 200 Ω.

Figure 4.1 (b) shows the x-ray diffraction spectra of Cu_xO thin films deposited on Pt (1 1 0), which was sputtered on MgO (1 1 0). Unlike the (1 0 0) case, this orientation promotes formation of the monoclinic CuO phase, which can be assigned to the unlabeled peaks. Growth on Pt (1 1 1), based on MgO (1 1 1), is shown in Figure 4.1 (c). While the Cu_2O phase has a single orientation (1 1 1) and the peak is relatively sharp with a small FWHM, there are several undesirable features. Atom mobility along close-packed planes in cubic materials is higher, which may lead to increased alloy formation, as shown by the larger magnitude of the Pt-Cu alloy peak. In addition, there is now evidence of Cu formation, which is problematic for device performance.

Figure 4.3 shows the nucleation morphology and RHEED patterns of a Cu_2O film grown on Pt (1 0 0). The RHEED images indicate that the sputtered Pt film is smooth within the RHEED coherence length, which means that grain

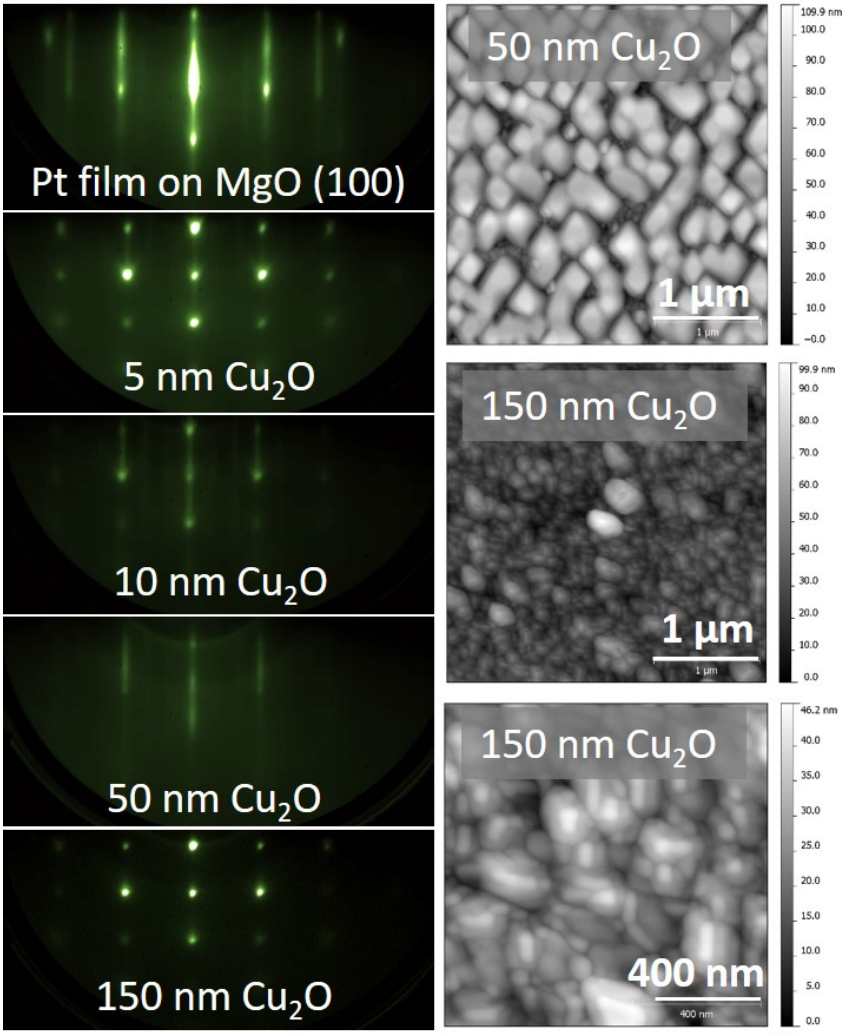

Figure 4.3: RHEED and AFM images of Cu_2O on Pt (1 0 0).

size is on the order of about 100 nm or larger on average. This is confirmed by AFM topography scans of Chapter 3. Cu_2O growth initiates in island growth mode as evidenced by the spotty nature of the RHEED pattern at a thickness of about 5 nm. At around 10 nm, the RHEED pattern starts to exhibit streaks, which indicates a two-dimensional growth mode. This growth mode dominates until the individual islands merge; however, at 150 nm the RHEED pattern once again shows spots, which means there is a small growth window for the two-dimensional mode, but that easily breaks down into island growth. Cu_2O islands nucleate predominantly along the (1 1 0) direction and

grain size exceeds that of the underlying Pt film.

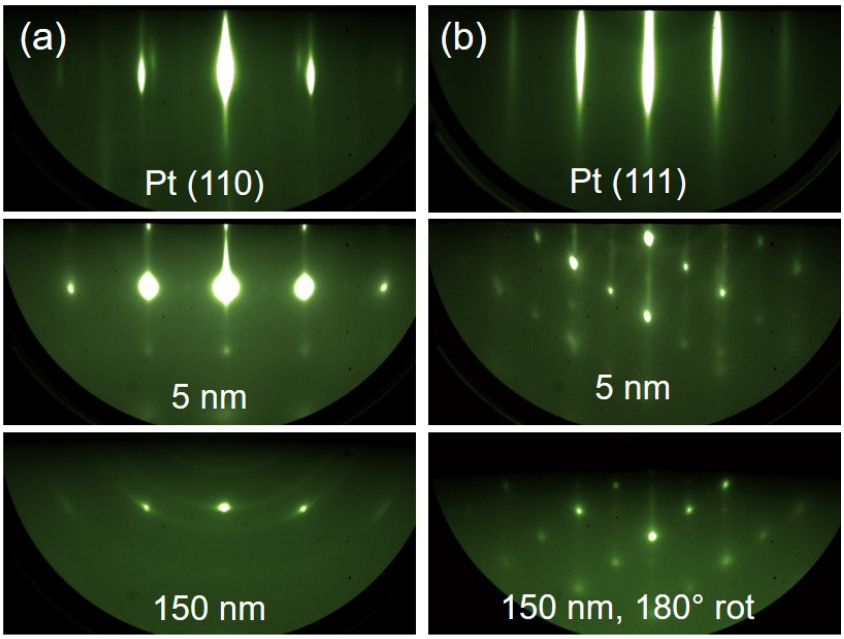

Figure 4.4: RHEED images of Cu_2O on (a) Pt (1 1 0) and (b) Pt (1 1 1).

Figure 4.4 (a) shows surface structural properties of Cu_2O deposited on Pt (1 1 0). As can be seen from the RHEED images, the Pt film grown on MgO (1 1 0) is rougher than that grown on MgO (1 0 0), and the resulting Cu_2O film is also rough as shown by the wide RHEED spots after 5 nm of deposition. After 150 nm, growth is predominantly in the (1 1 0) direction; however, multiple orientations as well as the presence of the CuO phase cause the film to be highly polycrystalline, as evidenced by the appearance of rings in the RHEED pattern. Under these conditions, the Pt/MgO (1 1 0) orientation is less favorable for growth of phase pure Cu_2O, however further optimization of growth parameters may yield more favorable results. Figure 4.4 (b) shows RHEED images of the Pt (1 1 1) template and subsequent growth of Cu_2O. The Pt (1 1 1) surface is very smooth, and has a roughness lower than both the Pt (1 0 0) and (1 1 0) surfaces, as indicated by long and narrow streaks in the surface diffraction pattern. The resulting Cu_2O film is three-dimensional

but has a single orientation, with the zone axis corresponding closely to [1 1 2].

Figure 4.5 shows two cross-sectional bright field TEM micrographs of a Cu_2O film grown on Pt (1 0 0) on MgO, corresponding to different sections of the same film. The MgO/Pt and Pt/Cu_2O interfaces appear to be very smooth and flat, and the Pt film thickness is highly uniform. The Cu_2O film has a three-dimensional structure, with facets clearly shown in (a). There is a defective layer at the interface between Cu_2O and Pt that may be due to epitaxial strain relaxation; this layer is on the order of 50 nm. In part (b) the Cu_2O layer appears to have some beam-induced recrystallization, which is likely due to damage cause by the focused ion beam during sample preparation.

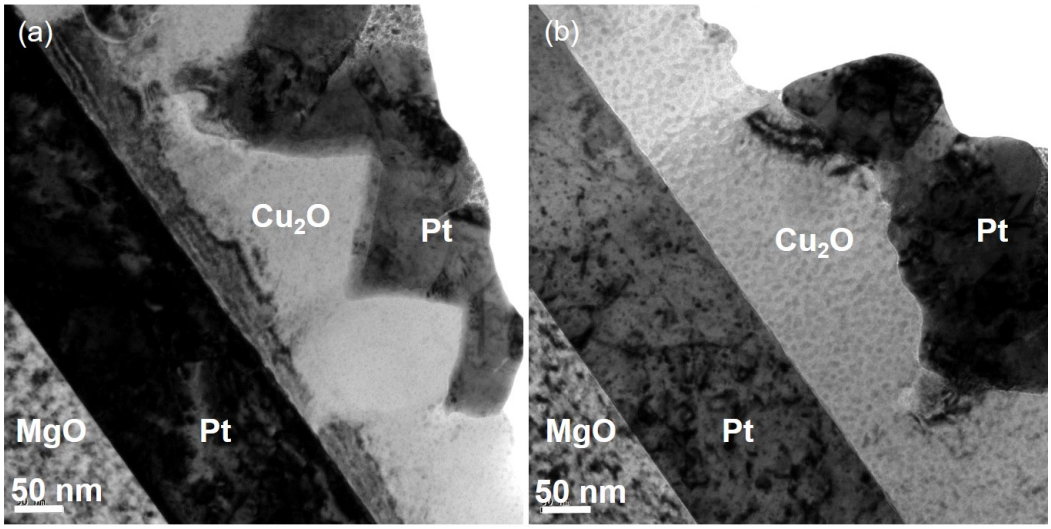

Figure 4.5: (a) Cross sectional TEM of Cu_xO grown by MBE on a sputtered heteroepitaxial template of Pt on MgO, (b) different area of the same sample.

High resolution TEM micrographs of the (a) Pt/MgO interface and (b) the Pt/Cu_2O interface are shown in Figure 4.6. The Pt/MgO interface has a strained layer that's less than 5 nm thick and the two lattices seem to be in registry, confirming epitaxial growth. The Pt/Cu_2O interface exhibits a higher degree of roughness, but the interface is still relatively sharp and although some chemical mixing is present, as shown by x-ray diffraction studies, there is still a clear boundary between the Cu_2O and Pt regions.

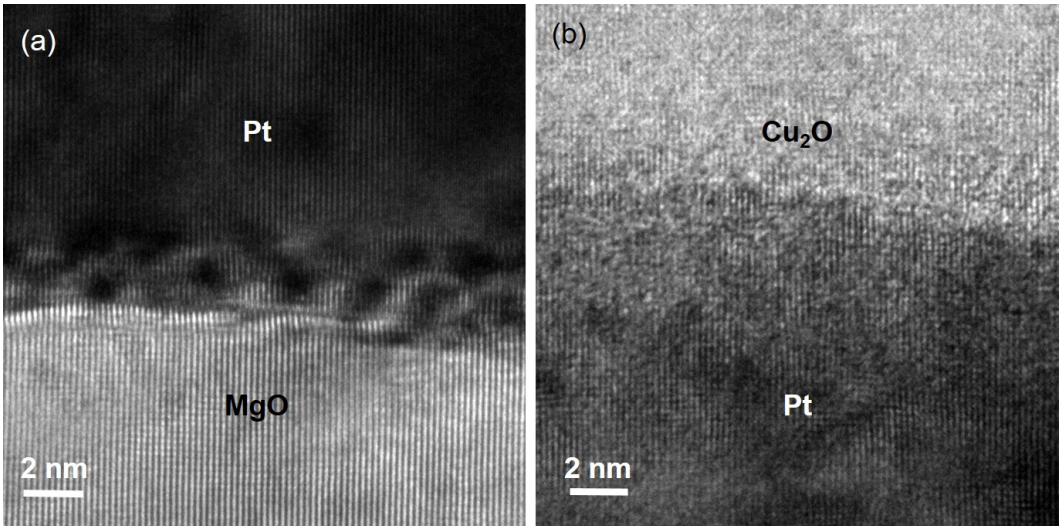

Figure 4.6: (a) Interface between Pt and MgO, (b) interface between Pt and Cu_2O. Zone axis is $\langle 1\,0\,0 \rangle$.

Selected area diffraction patterns are shown in Figure 4.7. These patterns were acquired using a 10 μm selected area aperture, beam spot size 8, and 4 second exposure time. Selecting only the Pt film and MgO substrate yields the pattern in (a). The zone axis is $\langle 1\,0\,0 \rangle$ and growth of Pt appears to be "cube-on-cube." Figure 4.7 (b) includes contributions from the Cu_2O, Pt, and MgO. Since Cu_2O is simple cubic, there are no reflections absent due to structure factor rules, which limit the mixed odd and even (h, k, l) from appearing in FCC structures of Pt and MgO. Thus we see reflections of the $\{1\,1\,0\}$ for Cu_2O.

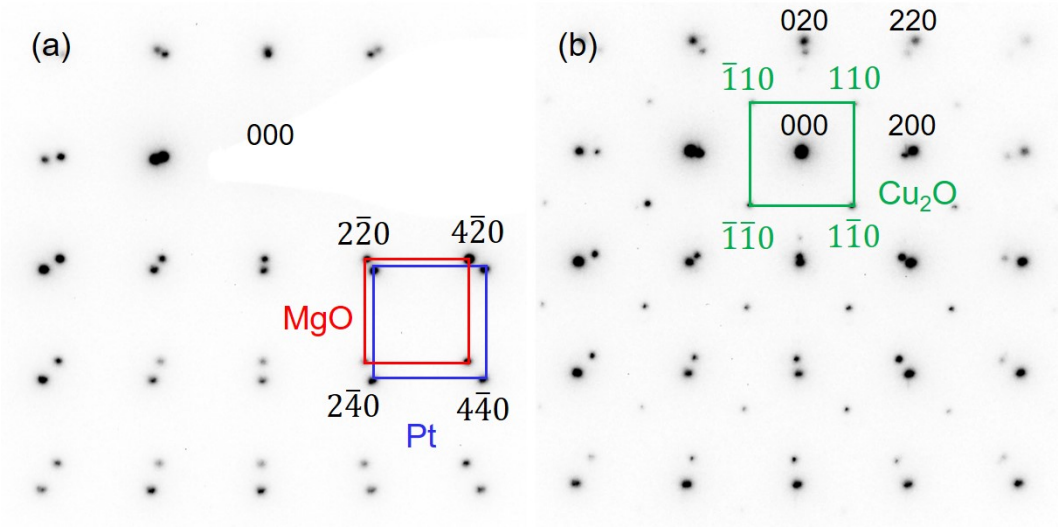

Figure 4.7: (a) Selected area diffraction pattern of Pt film on MgO, (b) selected area diffraction of a Cu_2O film deposited on Pt on MgO.

4.2 MBE of Cu_2O on Au

Growth of Cu_2O on Au sputtered films was also investigated. XRD spectra in Figure 4.8 show that the Cu_2O films on Au are highly oriented, just like on Pt. In chapter 3 we found that the Au (1 1 1) orientation persists even at high temperature, and the x-ray spectra of Figure 4.8 show a large Au (1 1 1) peak on MgO (1 0 0). This results in growth of predominantly Cu_2O (1 1 1), with some (1 0 0) and (1 1 0). Interestingly, there is no alloy peak for Cu-Au, although it is expected based on the phase diagram for these elements [53].

As shown in Figure 4.8 (b), the (1 1 0) substrate orientation leads to a single phase, single orientation Cu_2O (1 1 0) film, again with no peak for Cu-Au alloy. While this indicates that growth of phase pure Cu_2O films may be easier to achieve on Au than on Pt in a wider growth parameter window, we found in chapter 3 that the Au (1 1 0) film is not continuous on MgO under the growth parameters that were attempted.

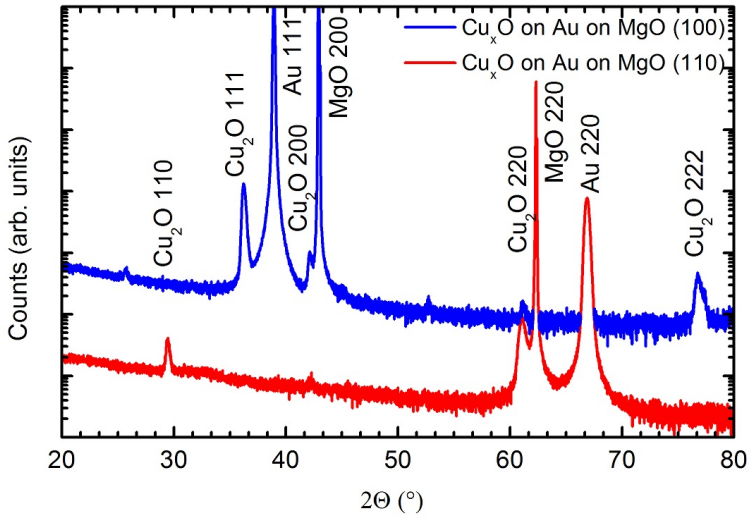

Figure 4.8: HRXRD of Cu_xO films grown on Au heteroepitaxial templates of (1 0 0) and (1 1 0) orientation.

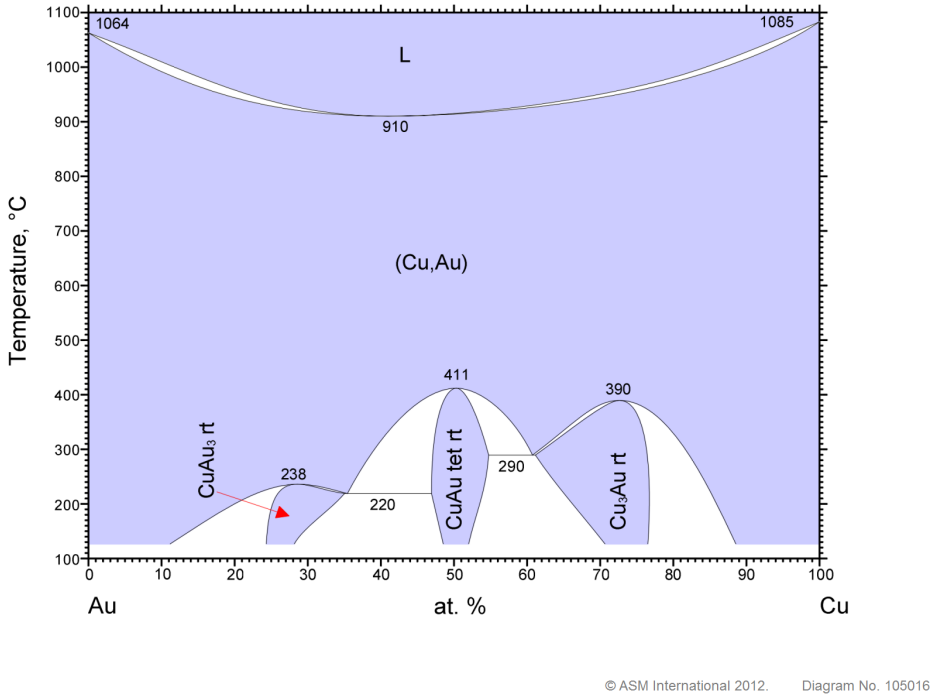

Figure 4.9: Phase diagram of Cu-Au system. [53]

Chapter 5

Cu_2O Device Synthesis and Characterization

5.1 Device Preparation Scheme

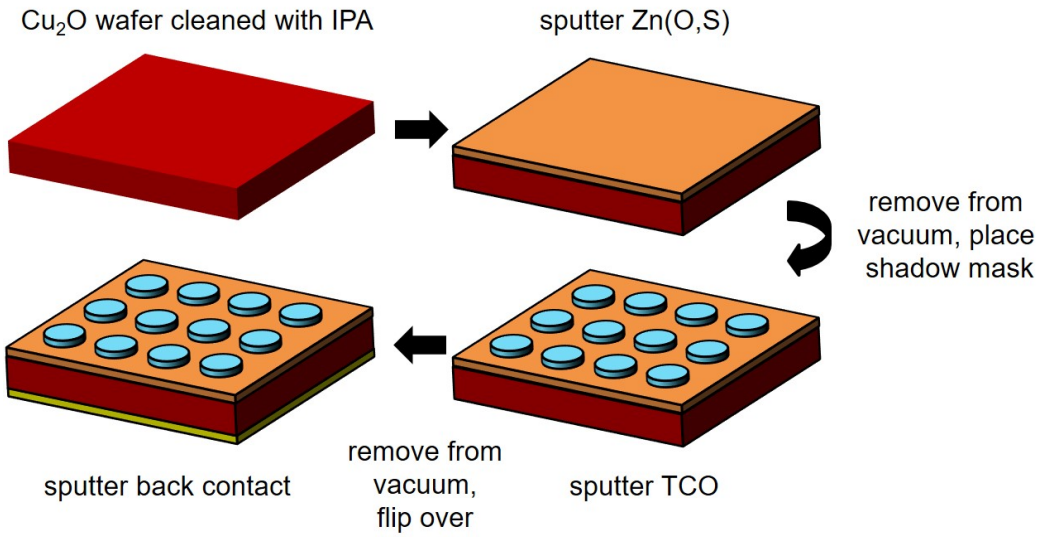

Figure 5.1: Solar cell fabrication scheme.

Figure 5.1 illustrates the basic device fabrication procedure. Polycrystalline Cu_2O wafers were produced from 6N purity Cu foils, which were heated in a quartz tube furnace to 1025 °C under N_2 flow for 4 hours. The foils were

then oxidized in air for 24 hours and cooled under N_2 flow to room temperature. Cu foil thickness was 0.5 mm and the final Cu_2O wafer thickness was approximately 0.8 mm, with typical carrier concentration of 10^{13}-10^{14} cm^{-3} and hole mobilities around 65 $cm^2V^{-1}s^{-1}$. Cu_2O wafers were cleaned with IPA and loaded into the magnetron sputtering system discussed in Chapter 3. It was found that the lowest possible base pressure corresponded to best device results and therefore the system was baked out overnight before to achieve pressures as low as 1.3x10^{-7} Torr. The Cu_2O wafer was heated in vacuum to the deposition temperature and annealed for 90 minutes, or kept under vacuum in the case of the room temperature samples. A Zn(O,S) layer of approximately 40 nm thickness was co-sputtered from ZnO and ZnS targets of 4N purity at a working pressure of 5 mTorr Ar. Power on the ZnO target was kept at 100 W, and the power on the ZnS target was 85 W. These values were previously determined to yield the highest V_{oc} devices and correspond to a composition of approximately $ZnO_{0.7}S_{0.3}$. After Zn(O,S) deposition, the samples were cooled in vacuum and removed from the chamber. A shadow mask was placed over the samples and a 60 nm ITO layer was then sputtered at 50 W in an Ar atmosphere at a working pressure of 3 mTorr, with no intentional heating. Lastly, an 80 nm Au contact was deposited on the back. Each wafer resulted in 12-16 solar cells with individual cell area of 0.02 cm^2.

5.2 Bulk Cu_2O-Zn(O,S) devices

The aim of this work is to evaluate the viability of Zn(O,S) as an earth-abundant heterojunction partner to Cu_2O. In particular, we examine the sources of photocurrent loss in polycrystalline Cu_2O/Zn(O,S) solar cells. Our results show that Zn(O,S) sputtered on Cu_2O forms a thin layer of $ZnSO_4$ at

the interface, and that this layer is detrimental to photocurrent collection in the solar cell. Deposition of Zn(O,S) at elevated temperatures decreases the presence of $ZnSO_4$, which decreases the barrier to photocurrent and thereby increases the average short circuit current density from 2 to 5 mA/cm^2 for cells deposited at 100 °C. The presence of a barrier at the Zn(O,S)/Cu_2O interface is further corroborated by spectral response measurements which indicate the presence of a current blocking layer.

5.2.1 Zn(O,S) as a Heterojunction Partner to Cu_2O

Zn(O,S), which is the focus of this study, is a particularly enticing candidate due to its earth abundance. The Zn(O,S)/Cu_2O electronic band alignment can be controlled by tuning the sulfur content of the Zn(O,S), which determines the position of the Zn(O,S) valence and conductions bands, and therefore allows for the fabrication of a high efficiency Cu_2O/Zn(O,S) device. While Zn(O,S) solar cells have demonstrated open circuit voltages above 1 V, the efficiencies of these devices have been limited by low short circuit currents and fill factors. In this paper we explore the sources of low current in these devices, and correlate the decrease in series resistance to a reduction in $ZnSO_4$, the most thermodynamically likely [2] compound to form in the presence of these elements. $ZnSO_4$ is a high band gap insulator that forms a conduction band spike with Cu_2O and therefore can act as a current blocking layer. Research on CIGS solar cells has shown that the presence of $ZnSO_4$ can be minimized by sputtering at elevated substrate temperatures on CIGS. [54]

In this work we demonstrate that similar to CIGS/Zn(O,S), the Cu_2O/Zn(O,S) interface is prone to $ZnSO_4$ formation, which contributes to an increase in series resistance of the junction, and subsequently significantly decreases the short circuit current (J_{sc}) that can be extracted. We show that deposition

of Zn(O,S) at elevated substrate temperature results in a significant improvement in the current collected, and thus the device efficiency. The best results are achieved with a substrate temperature of 100 °C, although even at this temperature some $ZnSO_4$ is still present. We further analyze possible reasons for reduced photovoltaic performance using light and voltage biased external quantum efficiency.

5.2.2 Current-voltage analysis

The solar cell performance was characterized as a function of Zn(O,S) deposition temperature. The current-voltage characteristics of the most-efficient cells at each temperature are shown in Figure 5.2 and the overall results are summarized in Table 5.1.

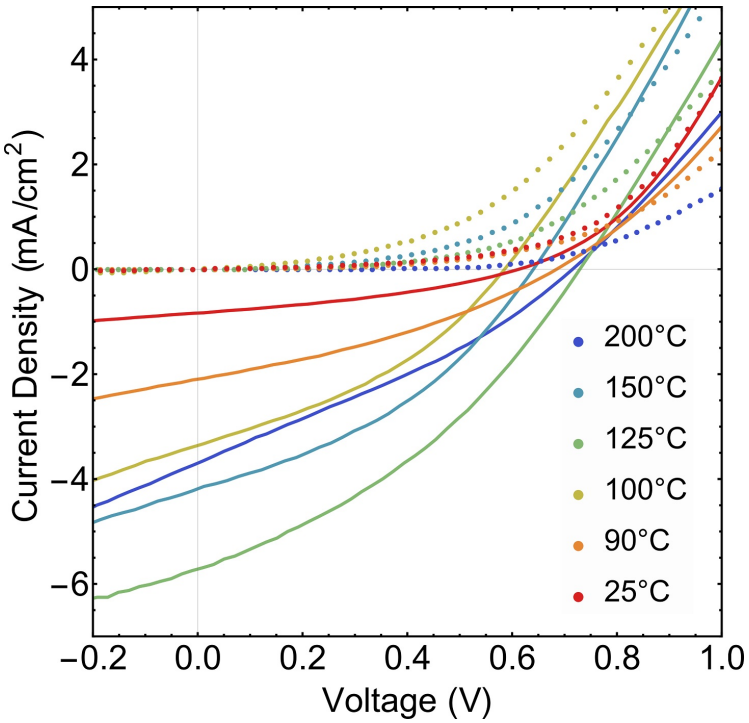

Figure 5.2: Current density as a function of voltage in the dark (dashed) and light (solid) for Cu_2O/Zn(O,S) solar cells deposited at different temperatures. All devices were tested under standard AM 1.5 illumination.

The device deposited at 100 °C has both the highest V_{oc} and J_{sc}. Notably,

there is crossover between the dark and light curves for every temperature, which indicates an electron barrier in the conduction band that is reduced under illumination. This reduction in the barrier can be due to photodoping of the Zn(O,S) buffer layer, which is confirmed by the spectral response in Figure 5.3. In addition, an electron barrier in the dark can also correspond to a high density of electronic defects at the interface that are filled with photogenerated carriers under illumination, reducing the barrier. [14]

The average open circuit voltage, which is correlated to the interface quality, varies from 419 mV at a deposition temperature of 200 °C to a maximum of 724 mV at 100 °C. This suggests that the highest quality Cu_2O/Zn(O,S) interface occurs for a Zn(O,S) deposition temperature of 100 °C. The effect of substrate temperature variation on the short circuit current (J_{sc}) is more significant. The J_{sc} increases from an average of 2.0 mA/cm^2 for devices deposited without intentional substrate heating to a maximum of 5.0 mA/cm^2 for devices deposited at 100 °C, and drops off significantly as the temperature is raised further. In order to understand the apparent barrier to current collection, the dark J-V curve was modeled using the non-ideal diode equation including the impact of series and shunt resistance:

$$I = I_0(exp(\frac{q(V - IR_s)}{nkT}) - 1) + \frac{V - IR_s}{R_{sh}}$$

where I_0 is the dark saturation current, q is the fundamental electron charge, n is the diode ideality factor, k is the Boltzmann constant, T is the temperature, R_s is the series resistance, and R_{sh} is the shunt resistance of the cell. The fit was obtained using a nonlinear least squares fitting method. As the deposition temperature of Zn(O,S) increases, the series resistance of the device decreases. For reference, through-thickness resistance of the Cu_2O wafer, which was expected to be the largest contribution to series resistance, was measured to be

on the order of 800 Ω. For a heterojunction deposited at room temperature, the series resistance is almost a magnitude higher, which indicates presence of a current blocking layer at the junction. At 200 °C, the series resistance of the cell is on the order of the Cu_2O wafer contribution, which suggests the junction resistance has been eliminated. We will analyze this further in Section 5.2.4.

Table 5.1: Solar cell results

T dep (°C)	V_{oc} max (mV)	V_{oc} avg (mV)	J_{sc} max (mA/ cm^2)	J_{sc} avg (mA/ cm^2)	R_s best (Ω)	R_s avg (Ω)	FF max	FF avg	η max (%)	η avg (%)
25	800	704	3.7	2.0	5889	4906	30.3	26.5	0.8	0.4
90	641	615	4.3	4.1	2389	2079	37.4	35.8	1.0	0.9
100	733	724	5.7	5.0	2446	2512	35.8	34.7	1.5	1.3
125	586	510	3.4	2.9	2146	2118	37.0	33.4	0.7	0.5
150	685	628	2.1	1.9	1329	1324	36.0	34.6	0.5	0.4
200	613	419	0.9	0.8	560	766	37.2	30.9	0.2	0.1

The large series resistance is evident in the low fill factor (FF) observed across all temperatures. The smallest FF is an average of 26.5% for devices deposited at room temperature and increases to about 35% for devices deposited at elevated temperature. The fill factor is further limited in the low-current regime by photoshunting, which is apparent from Figure 5.2. Ultimately, the efficiency is limited by the low FF. However, the efficiency increases from 0.8 % for room temperature devices to a maximum of 1.5 % for devices deposited at 100 °C, in large part due to the increase in short-circuit current.

5.2.3 External quantum efficiency characterization of solar cell deposited at 100 °C

Bias dependent external quantum efficiency (EQE) measurements were performed in order to further understand the photogenerated collection efficiency and photoshunting observed in the J-V curves. External quantum efficiency measurements were performed using a Xe arc lamp and slit monochromator, and calibrated to a reference Si photodiode with known spectral responsivity. White light bias was provided with a broadband LED. Voltage bias was controlled by a potentiostat.

Figure 5.3 (a) shows the EQE obtained at different voltage biases without any white light bias. At zero voltage bias, the EQE is close to 60% in the wavelength region from 500 to 570 nm before dropping off at the Cu_2O optical band edge. This indicates that the minority carrier diffusion length in our thermally oxidized Cu_2O is long and does not limit carrier collection far from the depletion region. On the other hand, the EQE in the short wavelength regime (below 500 nm), where carriers are generated close to the Cu_2O/Zn(O,S) junction, is significantly diminished due to high recombination at the heterojunction interface.

Figure 5.3 (b) shows the relative change in EQE with respect to the zero voltage bias. Reverse bias acts to increase the electric field in the depletion region, thereby increasing the band bending and boosting carrier drift. This results in a broadband increase in the EQE for all bias levels. The EQE does not saturate even at large reverse biases indicating the presence of large electronic losses. Similarly, forward bias leads to a reduction in the EQE at all bias voltages. Figure 5.3 (c) shows the same experiment performed with white light bias, sourced from a broadband LED, in order to more closely simulate operating conditions. The overall EQE is reduced for wavelengths beyond

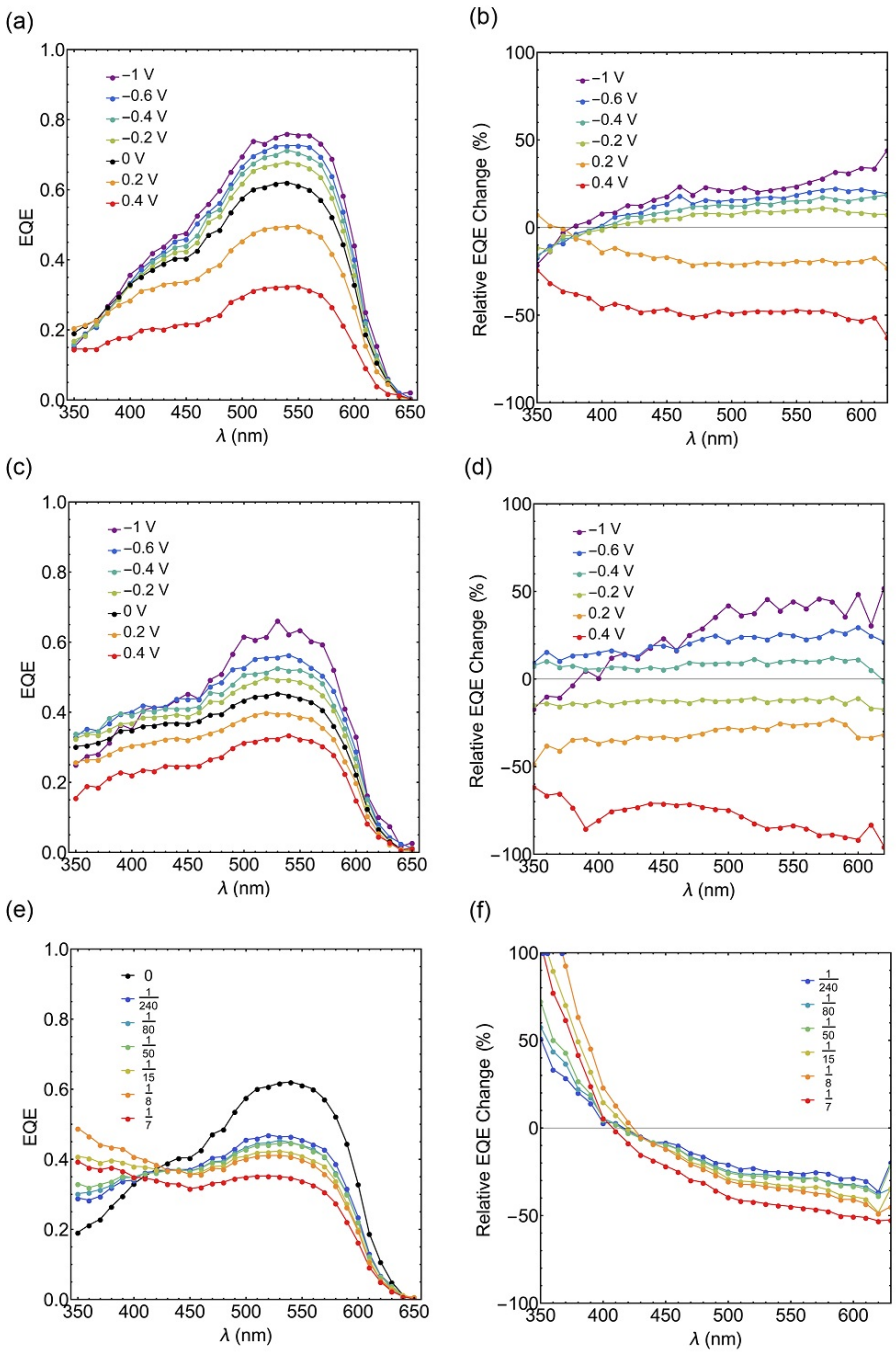

Figure 5.3: External quantum efficiency of solar cell deposited at 100 °C (a) with no light bias as a function of applied voltage bias; (b) relative change in EQE compared to zero voltage bias. (c) EQE of same cell with white light illumination of 0.013 suns as a function of applied voltage bias and (d) relative change in EQE compared to short circuit operation under 0.013 sun illumination. (e) Effect of light bias on EQE at short circuit; (f) relative change in EQE as a function of light bias intensity.

about 415 nm, which corresponds to the Zn(O,S) band edge, and augmented for shorter wavelengths suggesting strong photodoping of the buffer layer under light bias. The relative change in light-biased EQE with respect to voltage bias is similarly broadband, as shown in Figure 5.3 (d). Figure 5.3 (e-f) illustrates the effect of light bias intensity on EQE at short circuit conditions, and the strong dependence of EQE response on light illumination intensity suggests that photodoping of the emitter decreases the photocurrent barrier at the heterojunction interface. [14, 55]

The integrated EQE without white light bias gives an expected short circuit current of 6.7 mA/cm^2, which is slightly higher than the short circuit current of 5.7 mA/cm^2 measured under standard AM1.5 illumination. However, integrating the EQE corresponding to the largest available illumination level of approximately 0.14 suns gives an expected short circuit current density of 4.3 mA/cm^2, which is significantly lower than the J_{sc} measured using the solar simulator. Extrapolating this trend to an EQE measured at 1 sun illumination would give an even lower expected value of J_{sc}. This confirms the presence of a large barrier to photocurrent in the dark, which is reduced under light illumination by doping the buffer layer. One possible reason for a large photocurrent barrier is the presence of $ZnSO_4$ at the interface between Zn(O,S) and Cu_2O, and we explore this idea in the next section. Another reason for low EQE response compared to the measured J_{sc} is a large density of shunts, which we analyze using light beam induced current measurements.

5.2.4 XPS characterization of Zn(O,S)/Cu_2O interfaces

X-ray photoelectron spectroscopy (XPS) was used to investigate the chemical composition of the Cu_2O/Zn(O,S) interface and to identify the origin of the current blocking layer. To confirm the composition of the interface, a very thin

layer of approximately 1-2 nm of Zn(O,S) was deposited on polycrystalline Cu_2O wafers. The samples were removed from vacuum and transferred to a Kratos Axis Ultra photoelectron spectrometer with base pressure below $5x10^{-9}$ Torr. X-ray photoelectron spectroscopy was performed with Al K-alpha x-rays ($h\nu = 1486.7$ eV). High resolution scans of the Cu 2p, O 1s, S 2p peaks were acquired at 25 meV step size, 10 eV pass energy, and slot aperture.

Figure 5.4 (a) investigates the effect of annealing the Cu_2O substrate in vacuum. The as-grown surface contains a considerable amount of CuO as evidenced by the satellite peaks between 940 and 945 eV and the shoulder at 935 eV. This CuO layer results from air exposure after the thermal oxidation procedure and is present on all samples. Annealing at 100 °C reduces the amount of CuO present at the substrate surface and is effectively eliminated by annealing at 200 °C.

XPS spectra were also collected from polycrystalline Cu_2O substrates with approximately 1-2 nm thick films of Zn(O,S) deposited at different temperatures in order to examine the stoichiometry of the Cu_2O/Zn(O,S) interface (Figure 5.4 (b-d)). The absence of the shoulder and satellite peaks in Figure 5.4 (b) confirms the reactive removal of the CuO layer present on the as-grown substrates by deposition of Zn(O,S). In addition, the Cu Auger spectra did not show any evidence of elemental Cu formation and therefore we conclude that the Cu_2O surface is stoichiometric which is necessary for the best solar cell performance [7]. Figure 5.4 (c) shows the S 2p doublet of the Zn(O,S) film and contains composition information about the sulfur phases that are present at the interface. It was found previously that $ZnSO_4$ forms primarily at the heterojunction interface [2], with the bulk of the film being the desired zinc oxysulfide phase. The main peak position of the $2p_{3/2}$ at 161.8 eV and the $2p_{1/2}$ position at 162.8 eV correspond to ZnS, confirming that the film is

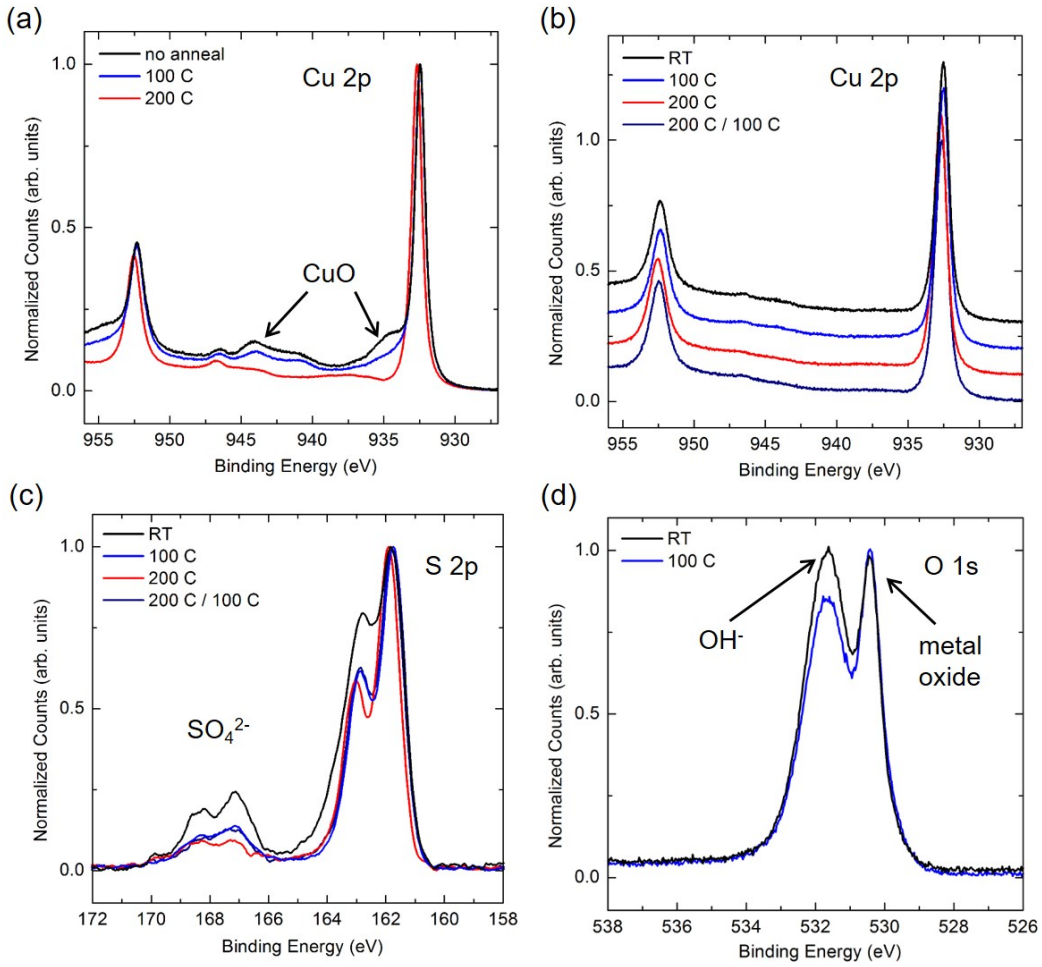

Figure 5.4: (a) Cu 2p peaks for a bare Cu_2O wafer annealed in vacuum inside the XPS chamber; (b) Cu 2p peaks, (c) S 2p peaks, and (d) O 1s peaks corresponding to XPS characterization of 1-2 nm Zn(O,S) layers deposited at different temperatures on Cu_2O.

primarily zinc oxysulfide. The smaller doublet around 168 eV confirms the presence of $ZnSO_4$. [56] The Zn(O,S) film deposited at room temperature has the largest amount of sulfate present. The relative sulfate content decreases as the deposition temperature rises.

In order to check whether the presence of CuO on the surface affected the chemistry of the growing Zn(O,S) film and promoted sulfate formation, a Cu_2O wafer was annealed at 200 °C to remove the CuO layer and then cooled down to 100 °C before depositing Zn(O,S). As shown in Figure 5.4

(c), the concentration of sulfate in this sample is negligibly different from the sample grown at 100 °C, suggesting that the presence of CuO on the surface does not significantly promote $ZnSO_4$ formation, and that deposition temperature is the dominant factor in limiting $ZnSO_4$ at the interface. The oxygen 1s peak in Figure 5.4 (d) showed presence of the Zn-O bond at 530.4 eV and metal hydroxide at 531.6 eV. [57] The magnitude of the hydroxide peak decreased as the temperature was increased to 100 °C, but was still present. This indicates that the decrease in $ZnSO_4$ concentration at the interface is of greater significance to maximizing the short circuit current, but that the remaining hydroxide could still be limiting device performance.

5.2.5 Structural Characterization of Zn(O,S)/Cu_2O interface

Figure 5.5 (a) shows a bright field cross sectional transmission electron micrograph of the solar cell deposited at 100 °C. The Cu_2O layer root-mean-square surface roughness is approximately 2 nm as measured by AFM and the Zn(O,S) and ITO layers grow conformally. The thickness of the Zn(O,S) layer is confirmed to be approximately 45 nm and ITO is approximately 55 nm.

Figure 5.5 (b) shows high resolution transmission electron micrographs of the Zn(O,S)/Cu_2O interface, with the inset showing the highest achievable magnification. The Zn(O,S) layer is amorphous with a small amount of nanocrystals, some of which may be due to beam-induced crystallization. The Cu_2O surface appears to have very little disorder, and no other phases seem to be present at the interface.

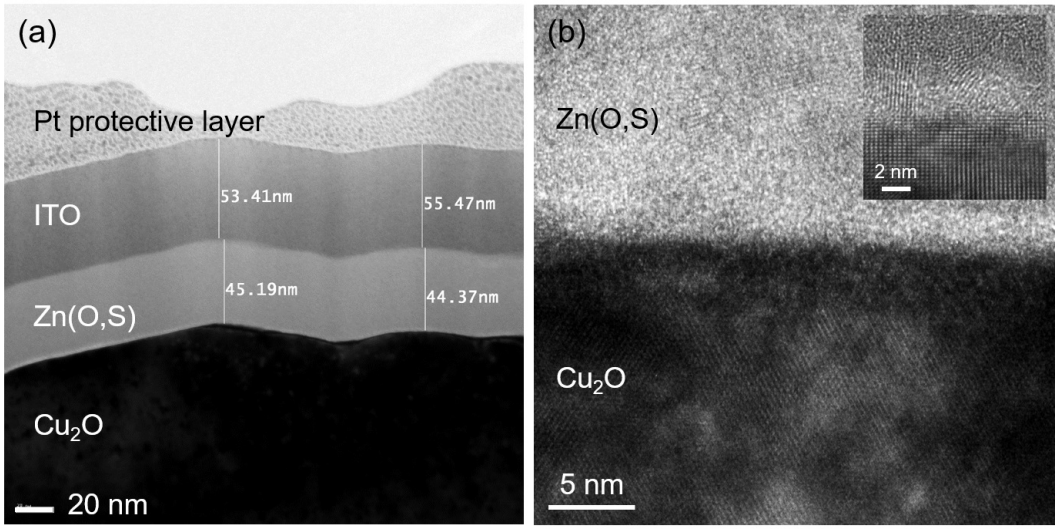

Figure 5.5: Transmission electron micrographs of Zn(O,S)/Cu_2O solar cell deposited at 100 °C. (a) Low resolution bright field image showing film thickness; (b) high resolution image of the Zn(O,S)/Cu_2O interface; (inset) highest magnification.

Conclusions

In this work, Zn(O,S) was analyzed as an earth-abundant heterojunction partner to Cu_2O. We report on the effect of deposition temperature on the composition of the Zn(O,S)/Cu_2O interface and the resulting changes in solar cell performance. We find that deposition of Zn(O,S) without intentional substrate heating yields an average short circuit current of 2 mA/cm^2 and increasing the substrate temperature results in a substantial short circuit current increase to an average of 5 mA/cm^2 at 100 °C. We correlate this improvement in current collection to a suppression of $ZnSO_4$ formation at the Zn(O,S)/Cu_2O interface, which acts as a barrier to photocurrent, using x-ray photoelectron spectroscopy. However, the photocurrent barrier still exists even for the highest efficiency cells, and further work is needed to address this issue in order to make Zn(O,S) a viable heterojunction partner for Cu_2O. EQE measurements confirm the presence of a photocurrent barrier and show strong light and voltage bias dependent collection.

5.3 LBIC characterization of polycrystalline Cu_2O solar cells

To further investigate the mechanisms of current collection loss in our devices, light beam induced current measurements were conducted on a large area solar cell deposited at 100 °C. Light (or Laser) Beam Induced Current (LBIC) measurement is a technique that can show and help determine the causes of spatial non-uniformity of photovoltaic devices. In this technique a laser beam is scanned across the solar cell's region of interest and the measured photocurrent is collected into a high-resolution map. This map can be used to identify regions of reduced current collection. While LBIC analysis has been instrumental in helping understand problems that face the more established photovoltaic technologies, such as Si and CdTe, there is no such prior work in Cu_2O photovoltaics as of the writing of this thesis. LBIC analysis was performed on solar cells described in the previous section, and several important conclusions emerge from this work. First, grain boundaries are electronically "dead," and are to be avoided or passivated, although passivation remains an area yet to be explored by the Cu_2O community. Second, photocurrent collection seems to depend on the grain orientation relationship, and further work is needed in this area.

5.3.1 LBIC setup

LBIC measurements were conducted on a Zeiss confocal laser scanning microscope (LSM 710) modified in-house such that instead of detecting the transmitted light using a photomultiplier, the current photogenerated in the device is sensed using a transimpedance amplifier (TIA). Figure 5.6 shows the schematic layout of the system.

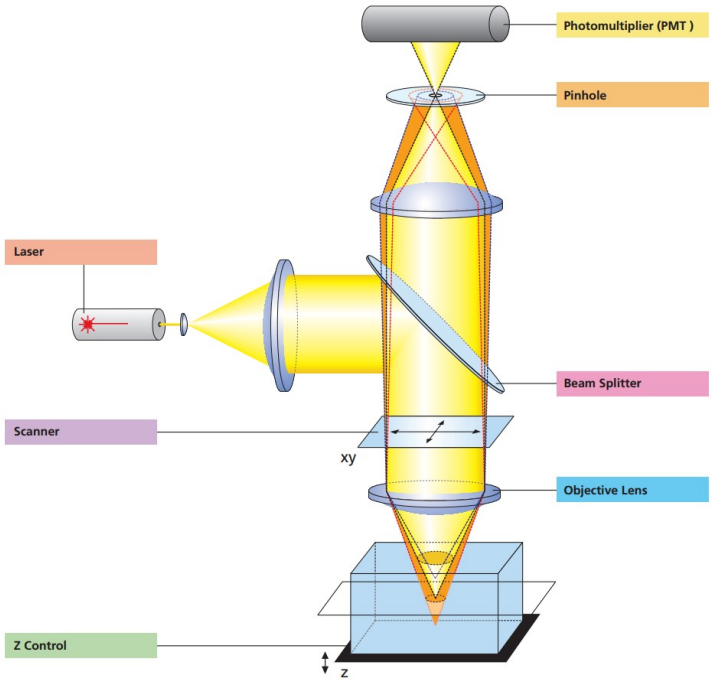

Figure 5.6: Schematic beam path of LBIC setup [image credit: Zeiss]

The main beam splitter is a dichroic mirror that reflects the laser light down to the sample and transmits all other wavelengths towards the detector such that the reflected light can also be measured. Light sources include 543 nm and 633 nm HeNe diode lasers as well as an Ar laser providing 458 nm, 488 nm, and 514 nm. For the purpose of this work, laser power was kept constant for all wavelengths at 750 nW. Although the laser spot size could not be easily measured, we can calculate the minimum value for the diffraction limited spot size by calculating the Airy disk diameter:

$$d_{Airy} = 1.22\frac{\lambda_{ex}}{NA_{obj}}$$

where λ_{ex} is the excitation wavelength and NA_{obj} is the numerical aperture of the objective lens. Using this approximation for the minimum spot size, the maximum power density incident on the solar cell can be calculated. This information is tabulated in Table 5.2. Two objective lenses were used, corre-

sponding to 2.5x magnification and 10x magnification. Larger magnification could not be achieved because as the magnification increases, the working distance decreases and the solar cell and probe contacts could not physically fit under the objective.

Table 5.2: Laser spot size and power density as a function of wavelength

wavelength (nm)	spot diameter (μm)		power density (W/m^2)	
	2.5x (NA=0.06)	10x (NA=0.25)	2.5x	10x
458	7.6	1.8	4133	73680
488	8.1	2.0	3639	59680
514	8.6	2.1	3228	54130
543	9.1	2.2	2883	49320
633	10.6	2.5	2125	38200

Since the actual spot size is much larger than the diffraction limited spot size, the actual power density is less than the values calculated in Table 5.2. The effects of laser power on the features in the image were investigated at each wavelength and no effect on the relative intensity of photocurrent was found, meaning that a higher incident laser power did not change the feature landscape of the image, only increased the relative signal. It should be noted that the current collected is not quantified, and therefore only spatial variations within the same image can be compared. For every laser wavelength, the digital gain and digital offset must be changed in order to maximize the signal. Nevertheless, we can learn a lot of useful information from these qualitative comparisons.

Figure 5.7 (a-c) shows spatially resolved photocurrent collected at different laser excitation wavelengths using a 2.5x objective. Figure 5.7 (d) shows the

reflected laser signal intensity so that the reflected signal can be compared to the collected photocurrent to ensure that changes in photocurrent are not caused by changes in reflectivity of the cell. Figure 5.8 (a-h) shows higher resolution scans of the same cell acquired using a 10x objective.

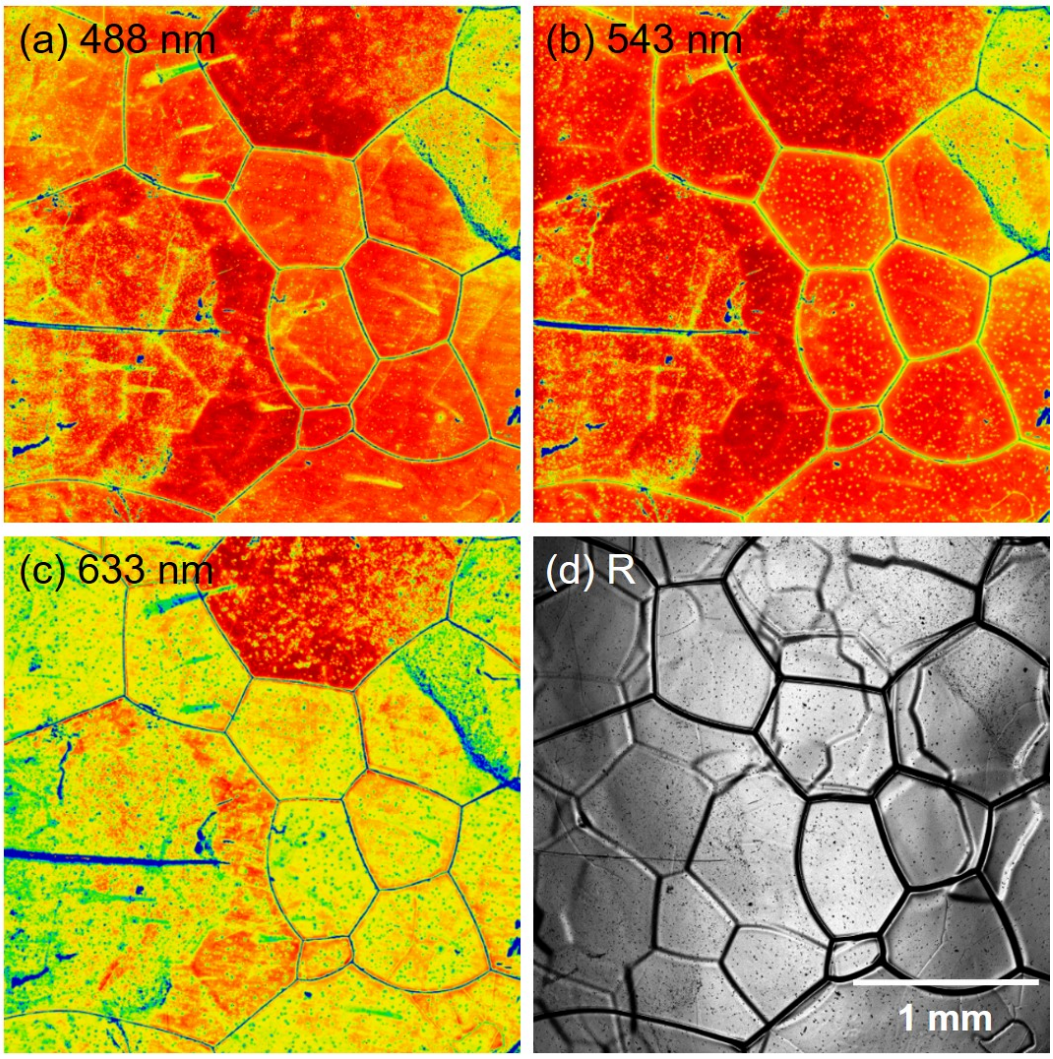

Figure 5.7: Light beam induced current characterization of large area solar cell using different laser excitation wavelengths and a 2.5x objective. Reflected signal is also shown to illustrate reflectivity dependence of photocurrent collection. Photocurrent maps acquired at (a) 488 nm, (b) 543 nm, (c) 633 nm; (d) image of reflected laser light.

First, the amount of photocurrent collected decreases substantially closer to the grain boundaries. This is not surprising for a semiconductor with no

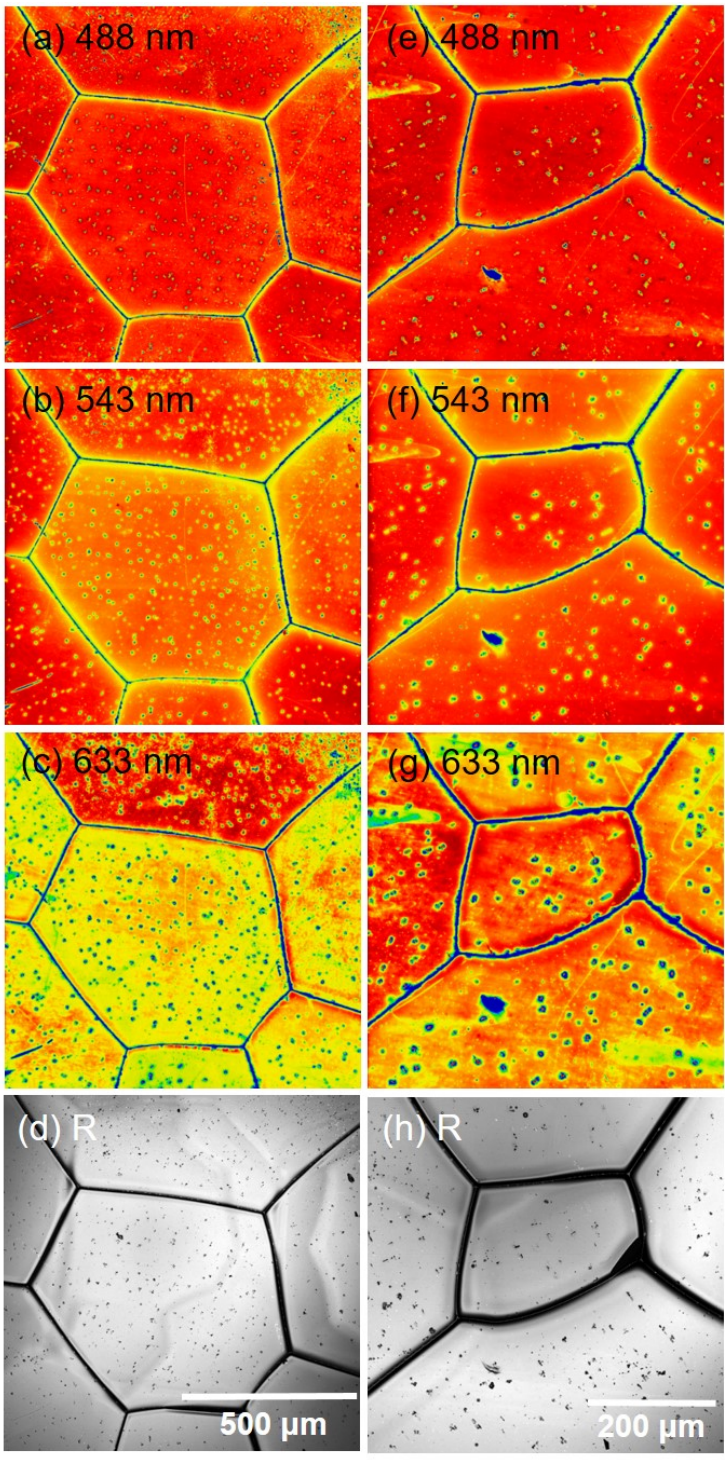

Figure 5.8: Light beam induced current characterization of large area solar cell using different laser excitation wavelengths and a 10x objective. Reflected signal is also shown to illustrate reflectivity dependence of photocurrent collection. Higher magnification could not be achieved due to working distance limitations of the objectives.

grain boundary passivation such as Cu_2O, and it underlines the importance of minimizing the amount of grain boundaries in a polycrystalline Cu_2O solar cell. In addition, the higher resolution scans in Figure 5.8 (a-h) show the presence of dimples on the surface that act as current sinks. There is a significant decrease in current collection at these dimples for longer wavelength excitation, where photons are absorbed far from the surface, which indicates that these defects likely arise from surface termination of threading dislocations. From these images we calculate, in ImageJ software, a dislocation density of about $5x10^4$ cm^{-2} from the LBIC images. Due to the limited resolution of these images the actual dislocation density could be much higher, so we take our calculated value to be the minimum dislocation density in thermally oxidized Cu_2O wafers prepared by the method used in this study. Dislocations, as well as grain boundaries, are known to reduce short circuit current and act as carrier recombination centers in solar cells, resulting in an increased dark leakage current. In GaAs solar cells, dislocation densities start to affect efficiency at concentrations around 10^4-10^5 cm^{-2}. [58]

Importantly, the LBIC images demonstrate a difference between the magnitude of current collection between different grains in the solar cell. This difference in photocurrent collection becomes more apparent as the excitation wavelength approaches the band gap. Cu_2O has an electronic bandgap of 2.09 eV at room temperature, and an optical bandgap of 1.9 eV at room temperature due to its large exciton binding energy. Excitation at 633 nm (1.96 eV) therefore produces excitons which are subsequently dissociated and collected as current.

5.3.2 Electron backscatter diffraction

Electron Backscatter Diffraction (EBSD) is a scanning electron microscope technique for measuring crystallographic structure and orientation of a polycrystalline sample. An electron beam of 20 keV energy strikes a sample which is tilted to 70 degrees towards a phosphor screen and CCD camera, which records the backscatter Kikuchi diffraction pattern at each point that is scanned by the electron beam.

To investigate possible reasons for the grain dependence of photocurrent collection, the out of plane crystallographic orientation of the polycrystalline wafers of Cu_2O was mapped using EBSD, as shown in Figure 5.9. The grain contributing the most photocurrent in Figure 5.9 is measured by EBSD to have a (1 0 1) surface orientation. Other grains, including {1 1 0}-type, have a significant effective offcut. DFT calculations have shown that the {1 1 0}-type orientations of Cu_2O have the lowest surface energy, which affects surface stability and reactivity. [29]

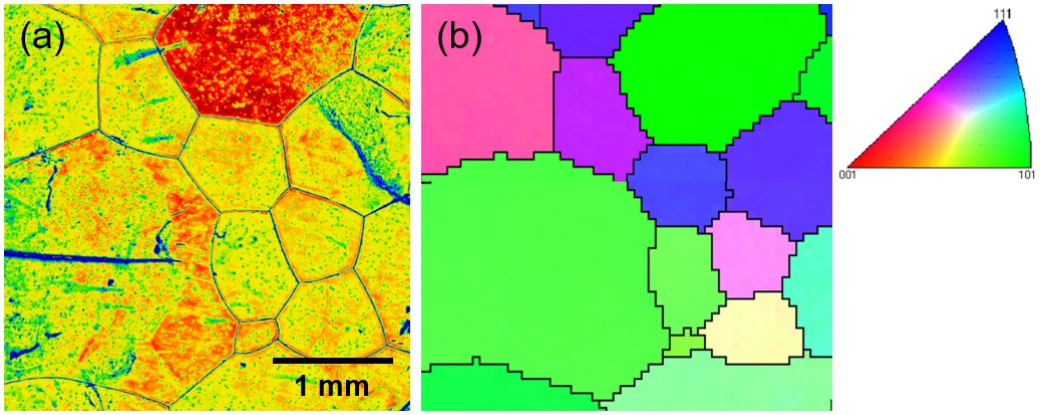

Figure 5.9: Comparison of (a) LBIC map with (b) EBSD orientation map with legend corresponding to the direction normal to the wafer surface.

Variations in surface energy should therefore lead to a surface chemistry that varies with orientation. Differing CuO layer coverages of the Cu_2O substrates may affect the properties and conductivity of the deposited Zn(O,S)

layer, thereby influencing the band offsets at the heterojunction interface as well as the depletion width. Orientation-dependent carrier transport for could also explain the variation in photocurrent collection with grain orientation, although Cu_2O has a cubic crystal structure and these effects have not been measured for single crystals. Our results suggest that an ideal surface chemistry is difficult to achieve for all grain orientations in a polycrystalline wafer, and this may be limiting polycrystalline Cu_2O photovoltaic efficiencies. We are currently exploring the crystallographic orientation dependence of Cu_2O solar cells using single crystals.

Conclusions

Light beam induced current measurements reveal a crystallographic orientation dependence of photocurrent collection, as well as a strong reduction in photocurrent around grain boundaries and threading dislocations. The difference in performance between different grains of the polycrystalline Cu_2O wafer suggests that (a) optimization of the entire polycrystalline surface may be impossible, limiting the potential viability of polycrystalline Cu_2O and (b) an optimal orientation of Cu_2O exists that would optimize the surface stoichiometry and maximize efficiency. Our findings suggest the (1 1 0) surface maximizes photocurrent collection, and agree with theoretical calculations that have shown that the (1 1 0) orientation has the lowest surface energy.

5.4 Thin Film Cu_2O Devices

Having developed growth of Cu_2O on heteroepitaxial ohmic templates in chapter 4, the next step was to see how these thin films compare with polycrystalline wafers when it comes to solar cell performance. Figure 5.10 shows the basic structure of these devices. The Cu_2O films grown on Pt and Au templates were transferred into the sputtering chamber and Zn(O,S) heterojunctions were deposited, followed by ITO top contacts, following the same procedure that was developed for polycrystalline wafers.

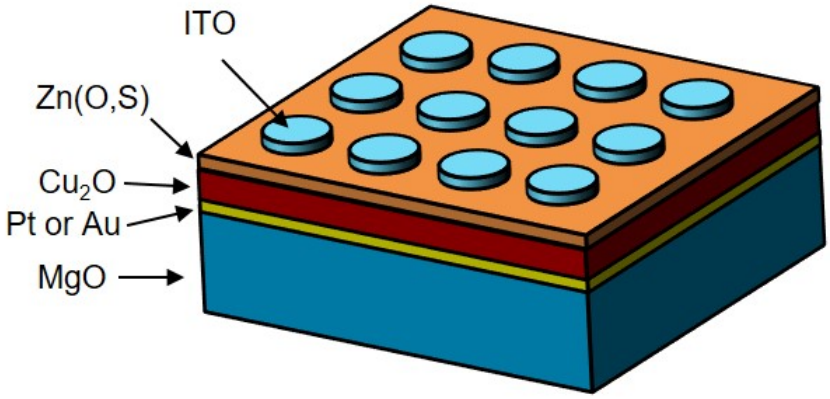

Figure 5.10: Structure of thin film solar cells.

The first devices that were made had Zn(O,S) layers deposited at room temperature. Figure 5.11 shows the photographs of these devices and J-V curves are presented in Figure 5.12.

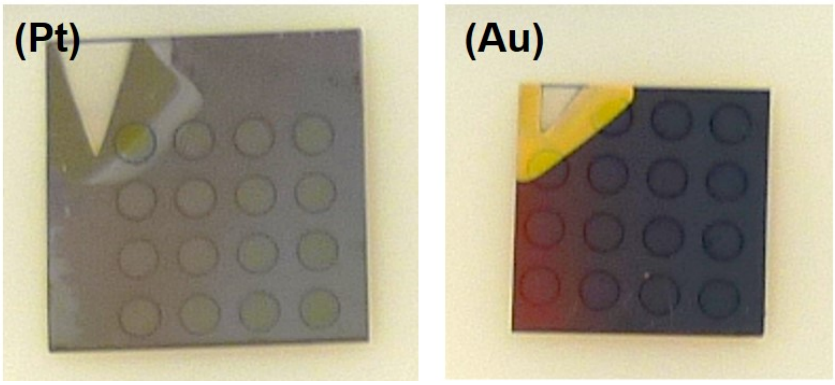

Figure 5.11: Photographs of thin film solar cells.

The Cu_2O layer thickness of both of these solar cells was approximately 420 nm, measured by profilometry and also expected from the previously measured growth rate of approximately 140 nm/hr. This thickness of Cu_2O is not enough to absorb all the incident light, so we expect a decrease in performance compared to the bulk polycrystalline wafers. Both cells are based on MgO (1 0 0) single crystals, which were shown in chapter 3 to produce epitaxial metal films with sub-nm roughness for both Au and Pt.

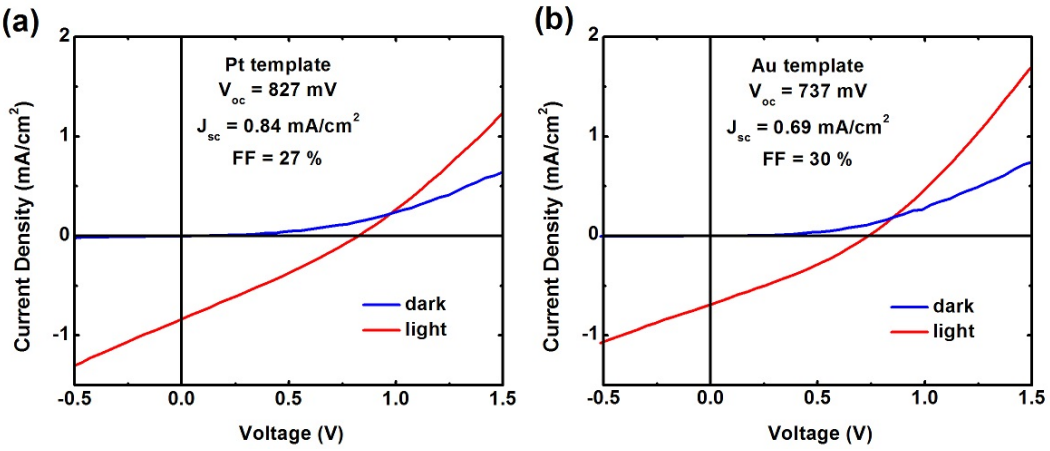

Figure 5.12: J-V curves of thin film solar cells deposited at room temperature on MgO (100).

From Figure 5.12, the device based on Pt exhibits a higher open circuit voltage of 827 mV as well as a higher short circuit current of 0.84 mA/cm^2 compared to the device based on Au, which had a V_{oc} of 737 mV and J_{sc} of 0.69 mA/cm^2. However, the Au-based device has a higher fill factor of 0.30, compared with 0.27 for Pt. This may be due to a lower degree of shunting, indicated by the smaller slope of the light curve around J_{sc}. While both samples had several individual solar cells, the results presented here are of the highest efficiency cells from each set. The generally low fill factor as well as short circuit current may be attributed to the current blocking layer in room-temperature deposited Zn(O,S) that was explored earlier in this chapter. Figure 5.13 shows the current-voltage characteristics of a thin film Cu_2O

solar cell based on Pt (1 0 0) where the Zn(O,S) layer was deposited at 100°C. These results are analogous to the polycrystalline Cu_2O case, and the open circuit voltage has dropped slightly to 667 mV, however the short circuit current has increased to 3.75 mA/cm^2. The fill factor has also increased to 0.35, which is close to the best result for polycrystalline Cu_2O cells.

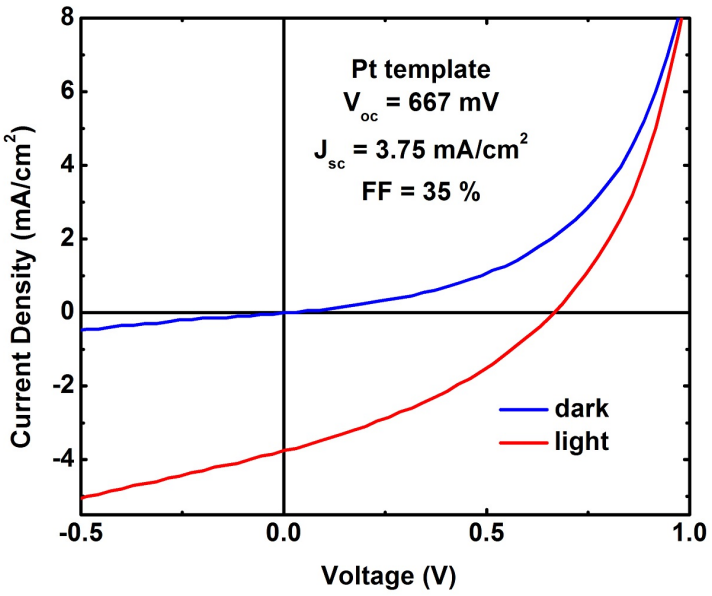

Figure 5.13: J-V curves of thin film solar cells deposited at 100°C.

Further work is being carried out to grow thicker Cu_2O films by molecular beam epitaxy in order to absorb all the incident light.

Chapter 6

Conclusions and Outlook

This thesis focused on understanding and improving photovoltaic performance of Cu_2O devices. To mitigate issues present in bulk thermally oxidized wafers and to provide a viable path for high quality thin film growth, we developed heteroepitaxial growth techniques to deposit Cu_2O. First, we successfully demonstrated epitaxy of Cu_2O on MgO single crystalline substrates of different crystallographic orientations. Next, we developed heteroepitaxial ohmic contact templates of Pt and Au using biased sputtering. We then used these templates to grow Cu_2O thin films and made the first Cu_2O/Zn(O,S) thin film solar cells where the active layer was deposited by molecular beam epitaxy.

In parallel, we explored the Cu_2O/Zn(O,S) heterojunction using bulk thermally oxidized wafers in order to understand sources of current loss in these devices. We found that a current blocking layer consisting mostly of zinc sulfate was present at the interface and that this layer could be minimized by raising the deposition temperature of Zn(O,S). We also performed the first light beam induced current measurements on polycrystalline Cu_2O solar cells, which revealed the detrimental effects of unpassivated grain boundaries in polycrystalline Cu_2O as well as presence of grain-dependent photocurrent col-

lection, which points to differences in surface reactivity of the different grain orientations. The difference in performance between different grains of the polycrystalline Cu_2O wafer suggests two important conclusions. First, optimization of the entire polycrystalline surface may be impossible, limiting the potential of polycrystalline Cu_2O from achieving high open circuit voltages throughout the device. Second, an optimal orientation of Cu_2O exists that would optimize the surface stoichiometry and solar cell efficiency.

From the results on thermally oxidized wafers, it is apparent that in order to maximize device efficiency, wafers that have very large grains, preferably single crystalline wafers oriented in a particular orientation need to be fabricated. Our results indicate that the (1 1 0) orientation is likely to produce the best interface due to stability of that surface orientation, and this needs to be investigated further. One approach that is being explored in our group is to use the float zone method to grow boules of Cu_2O and then orient and cut them exposing the desired surface orientation. Another, arguably simpler approach, is to further develop molecular beam epitaxial techniques for higher quality thin films. So far we've only had the chance to explore growth on MgO, Pt, and Au, and even those films are not as high quality as they can be with further optimization.

Ultimately, in order to produce a solar cell suitable as a top cell in a tandem structure with a c-Si bottom cell, it is imperative that the back contact absorbs as little light as possible. Therefore Pt and Au films will most likely not be transparent enough, unless made ultra thin. One approach is to use graphene as a back contact. We have shown that a monolayer of graphene placed on top of a Cu_2O wafer will allow many materials that would otherwise form rectifying contacts to Cu_2O to make an ohmic contact. This is important because it potentially allows the use of any transparent conducting material

to make ohmic contact to Cu_2O.

We've also briefly explored epitaxial lift-off of Cu_2O films grown on alkali halides such as NaCl, which simply dissolve in water, leaving the ultra thin Cu_2O layer floating on the surface. This idea is demonstrated in Figure 6.1. Epitaxial lift-off can enable synthesis of a thin film cell that can be lifted-off its substrate and placed on top of a c-Si cell to form a tandem. In this scheme, graphene can be used as a transparent ohmic back contact.

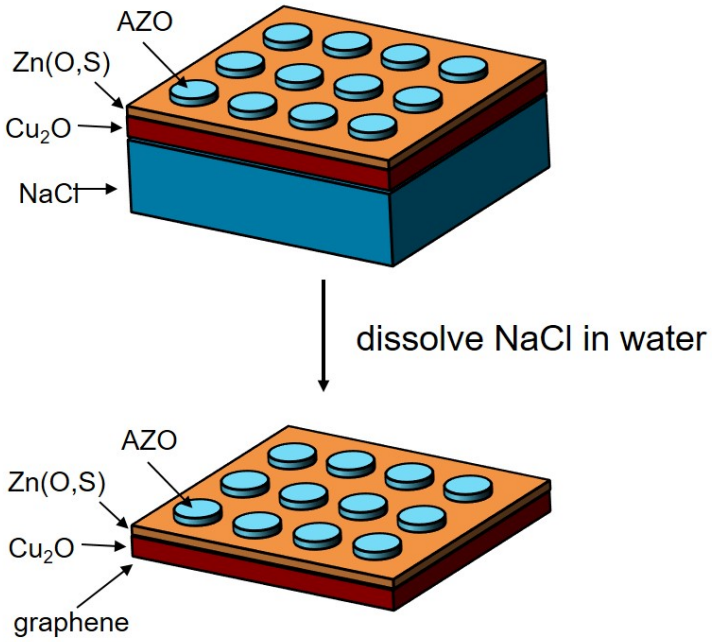

Figure 6.1: Schematic of epitaxial lift-off of solar cell

In addition, there is a lot of room to explore heteroepitaxy of Cu_2O in the superstrate configuration, where instead of being grown from the bottom contact up, the first layer to be deposited is the top transparent conducting contact, followed by the buffer layer/heterojunction partner, and then the Cu_2O absorber layer can be grown on top of that, followed by the back contact. This can be a particularly fruitful avenue for achieving crystalline heterojunction partners such as Ga_2O_3, which can be deposited at high temperature without adversely affecting the Cu_2O film.

Lastly, understanding the self-compensation and doping mechanisms in Cu_2O is paramount to achieving a high efficiency solar cell.

Appendix A

Oxide MBE User Guide

A.1 Sample loading

1. Clean chuck with IPA, attach sample using Mo clips.

   Ag paste has been used in the past, but while it does help provide good thermal contact, there is a risk of sample and chuck contamination. If using Ag paste, either use a clean Si wafer as a sacrificial layer, or have a dedicated chuck for Ag paste use. Note this will also have an adverse effect on the base pressure.

2. Load chuck into load lock, sample facing down, such that the loading arm fork grips the bottom groove of the chuck (the groove that's now closest to the top surface of the chuck since the chuck is upside-down). Ensure that the chuck sits securely in the grooves of the fork.

3. Close lid, turn on nitrogen flow (green valve), if not already flowing. Purging the load lock with nitrogen helps dilute some of the water and oxygen that are present in air.

4. Turn off nitrogen after purging. Turn on mechanical pump, wait for pressure to get below 20 mTorr. To prevent the pump from overheating, turn on the cooling fan.

5. Turn on turbo, wait for it to spin up and give it 20 min to pump down. The load lock is equipped with a quartz heating lamp for internal baking. This helps achieve a lower base pressure in the load lock and eliminate water contamination. Turn on the lamp by slowly turning on the variac located below the load lock. Let it bake for as long as needed (a few hours to overnight). Note that this will also heat up the substrate and chuck, so before loading into the main chamber, make sure to slowly

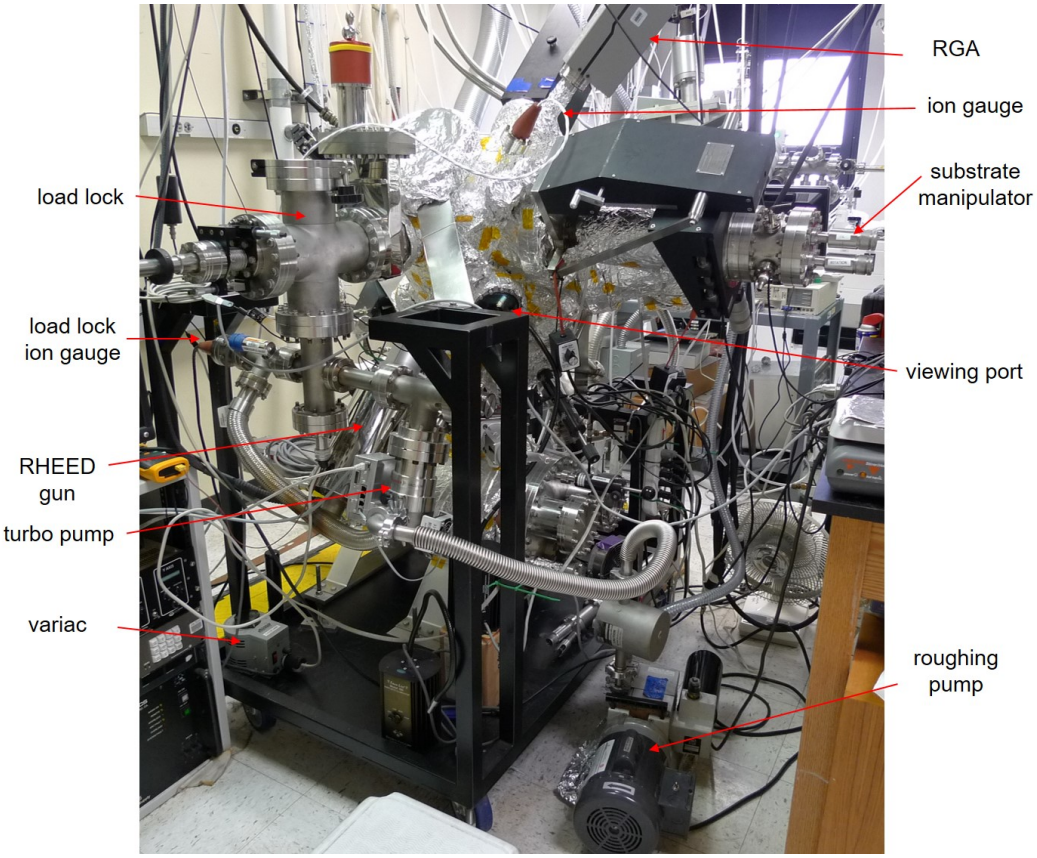

Figure A.1: Oxide MBE system

turn off the variac and let the chuck cool. Use the ion gauge on the load lock (IG2) to measure pressure before opening the gate valve. Also, it's a good idea to check the turbo pump motor current to get a sense of the gas load.

6. Once pressure in load lock is stabilized, open the gate valve and slide sample into the main chamber. Use the webcam and gooseneck lamp to observe. First, move the loading arm magnet such that the chuck slides onto the main chamber fork assembly. Use the tilt and rotation knobs to ensure correct placement. Once the chuck is loaded all the way, use the rotation knob to rotate the main chamber fork clockwise. The tilt knob may need to be adjusted. Once rotation is no longer possible, tilt the assembly to unlatch the chuck and carefully start to pull out the arm. Make sure to watch the webcam; this might be tricky. If the chuck slides off, make sure to re-adjust tilt and rotation. Once the main chamber fork is facing towards the evaporation sources, pull out the arm all the way and close the gate valve. Tilt the substrate chuck to its final position and lower the sample shutter.

A.2 General growth procedure

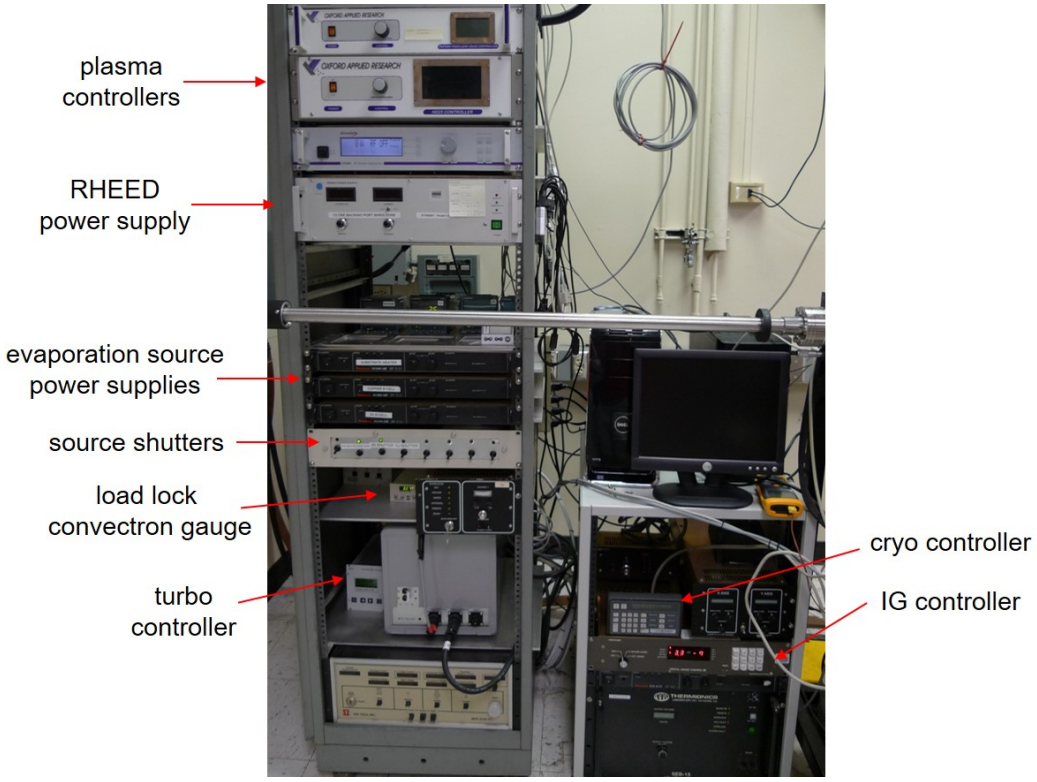

Figure A.2: Oxide MBE controls

A.2.1 Heating Cu source

Before heating any source, make sure that its shutter is closed (and also preferably the substrate shutter).

The Cu evaporation cell takes a long time to heat up (around 3 hours), so usually start this first. Use the eurotherm to create a heating and cooling program. Currently for Cu, the following program is set:

1. Heat to 1000°C at 10°C/min
2. Dwell for 5 min
3. Heat from 1000°C to 1325°C at 5°C/min (It's important to go slowly through the solid to liquid transition (around 1080°C for Cu) and back since this places a lot of stress on the crucible. I keep heating slowly slowly to the deposition T because the Sorensen power source is close to the current limit of 18 A at this point, and I found that it gets unstable if heating faster. Alternatively, can find another power supply with a higher maximum current.)

4. Dwell at 1325°C for 5 min. This is the deposition temperature so we can press "hold" on the eurotherm to pause the program at this T. (The rest of the program is the reverse of previously mentioned steps. Note that it's again very important to cool slowly around the phase transition).

It's useful to know what the resistance of the evaporation source filaments is at different temperatures. This way you can anticipate a failure or know if something is wrong.

The same procedure would apply to other evaporation sources, just make sure to check acceptable heating rates for each material.

A.2.2 Heating substrate

Substrate heating is a little different since there is no thermocouple measuring temperature and feeding this back to the controller. Therefore we just slowly increase the power output to achieve a certain temperature. This is done in "manual" mode on the eurotherm. Make sure to increase the power slowly. Figure A.3 shows the approximate relationship between the power output and substrate temperature. The actual temperature is higher since this calibration was done at 10^4 Torr, and typical growth pressures are at least an order of magnitude lower.

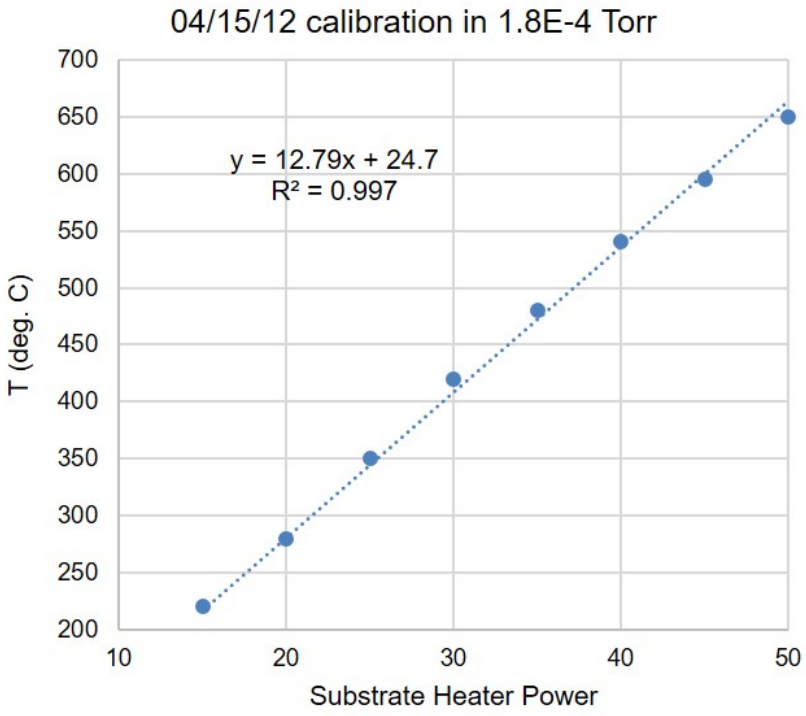

Figure A.3: Substrate heater calibration using thermocouple wafer

A.2.3 Plasma

Figure A.4: Process gas control. Top: piezo leak valve controller used to set gas flow rate; middle: plasma matching unit; bottom: RF power generator.

1. Start recording chamber partial pressures with the RGA.
2. Ensure that the process gas tank is open, as are all the valves leading up to the piezo leak valve. Also make sure the cooling water is flowing.
3. Turn on PLV1000 leak valve controller, RF power generator, and HD25 controller.
4. Set the "load" and "tune" to Auto (they reset to manual whenever you turn off the controller).
5. Set ion deflection plate voltage to desired value (this will deflect ions away from the film, leaving only neutral atoms in the beam).
6. Start flowing process gas by slowly opening the leak valve. Once the chamber pressure reaches mid-10^{-6} Torr, set RF power to 125 W and turn on. The reflected power should spike and then decrease to zero. If it's not decreasing to zero, the tune and load are either not set to auto (or the values are not appropriate).
7. Once the reflected power has gone to zero, this is the low brightness mode of the plasma (the plasma is not "lit"). Now we need to increase the process gas pressure (but not above 10^{-4} Torr) and plasma power (but not above 200W) until the high brightness mode is reached. It

sometimes helps to spike the pressure (for example by closing the green shut-off valve behind the piezo leak valve while keeping the leak valve open and then opening the green valve again). The high brightness mode has a region of stability, and will extinguish if the pressure it too high or too low. Once the high brightness mode is reached, reflected power will once again spike and then decrease to zero.

8. Once the plasma is bright, decrease the chamber pressure to the desired deposition pressure and slowly set the power. Let the plasma stabilize for a few minutes.

9. Using the PCR mode is recommended. This mode, which can be accessed by pressing the main knob, will automatically adjust the plasma power to achieve a constant optical emission voltage. The optical emission voltage is the integrated optical emission of the plasma and contains information about the plasma efficiency. Keeping a constant emission voltage usually produces the most reproducible results. One reason that the emission voltage would change is a change in flow rate, which usually happens during the first few hours of plasma operation as the pressure in teh chamber reaches steady state.

The plasma should be checked at least once every hour during the first 4-5 hours of growth, and the leak valve pressure can be adjusted (usually an increase is necessary) slightly in order to keep the power from increasing too much. After that the system becomes very stable and can run for many hours without any adjustments. (But don't take my word for it!)

To switch process gas between O_2 and Ar/O_2 mix, close the tanks, use an oil free scroll pump to evacuate the gas lines. Purge with the gas you are switching to and evacuate a couple times.

A.2.4 RHEED

1. Open KSA400 software, hit Live Video button.

2. (When using process gas) Ensure that the load lock is pumped down fully and open the backing port. This allows for differential pumping of the RHEED gun, which is important when the chamber pressure is above 10^{-6} Torr, and especially important for operation with oxygen.

3. Ramp up voltage and current slowly, according to the manual (or slower). For voltage, ramp to 10 kV over 10 s, then to 20 kV over 10 s. For current, 0 - 1 A in 5 sec, then steps of 0.1 every 5 s up to 1.5 A (if new filament, or after venting, for current use 0 - 1 A in 15 s, 1 - 1.2 A in 30 s, wait 30 s, then 0.1 A every 20 s).

4. Use beam deflectors and sample tilt (top knob)/sample rotation (bottom knob) to position the substrate to get a signal. Note: if sample is not

conductive (like MgO), can cause significant charging; flowing process gas and turning on the RF source may help.

There are 2 levels of standby for the RHEED gun. If not using the RHEED for a period of time less than 1 hour, the current and voltage can be kept at 1.2 A/20 kV. For standby times between 1 and 2 hours, use 1 A/10 kV. If not using it for longer than 2 hours, decrease both to 0.

Placing the substrate in the same position on the chuck is important for finding it in RHEED as well as getting reproducible depositions.

Note that electron beam exposure does locally affect the growth of the film, so make sure to keep the beam shuttered when not recording images.

A.3 Shutdown

1. To complete film deposition, first shutter the substrate.
2. Shutter the evaporation cell and run the cooling program.
3. To turn off the plasma, first set PCR back to manual mode. The slowly decrease the power to less than 100 W. Turn off the power and slowly decrease the piezo leak valve voltage to zero.
4. Decrease the substrate heater power slowly at the desired rate and wait for all components to cool before unloading sample.

A.4 Notes and Troubleshooting

- Power outages happen, and let's hope they don't happen when you're growing. The main issue with a power outage on this system is that the cryo shuts down and doesn't start back up again, even if the power is out for a fraction of a second, and unfortunately our system doesn't have the option to start it back up again, although some others do. So the best thing to do is to restart the cryo as soon as possible, unless it's heated up to above 20 K.
- The sample chuck is made from Haynes alloy 230, which is a Ni alloy with good oxidation resistance at high temperature and high machinability.
- The sample heater is made from a solid piece of SiC. The wires leading to the SiC are Ag-coated Cu, which is somewhat resistant to oxidation, but high current does decrease their lifetime. For reference, the wires have broken twice in the past 6 years.

A.5 Bakeout

The system is fitted with several heating tapes for bake out. Ramp the power slowly in increments of 5 every 15 min or so to let the system slowly heat up. Use a thermocouple to measure the chamber temperature and make sure there are no hot spots. Bake for as long as necessary (you can bake between runs also for the lowest base pressure), and remember to cool slowly.

Appendix B

PLD User Guide

Notes on system usage, cleaning, and maintenance
Written by WooChul Jung and Yulia Tolstova.

Figure B.1: Main control panel

B.1 Cleaning and loading

1. Clean the interior of the vacuum chamber with isopropyl alcohol, gently wiping down surfaces to remove residue from previous depositions. Clean and polish the window which faces the laser optics with diamond paste. Be careful that your skin does not touch the inside surfaces of the chamber. Always wear gloves while touching the inside of the chamber and a lab coat so that you do not contaminate your clothing with deposited material. **Wear a respirator.**

2. (Optional) Clean and polish the sample stage, shutter, and shields surrounding the target to prevent contamination and ensure even distribution when sputtering. Note that the shutter is difficult to remove, and

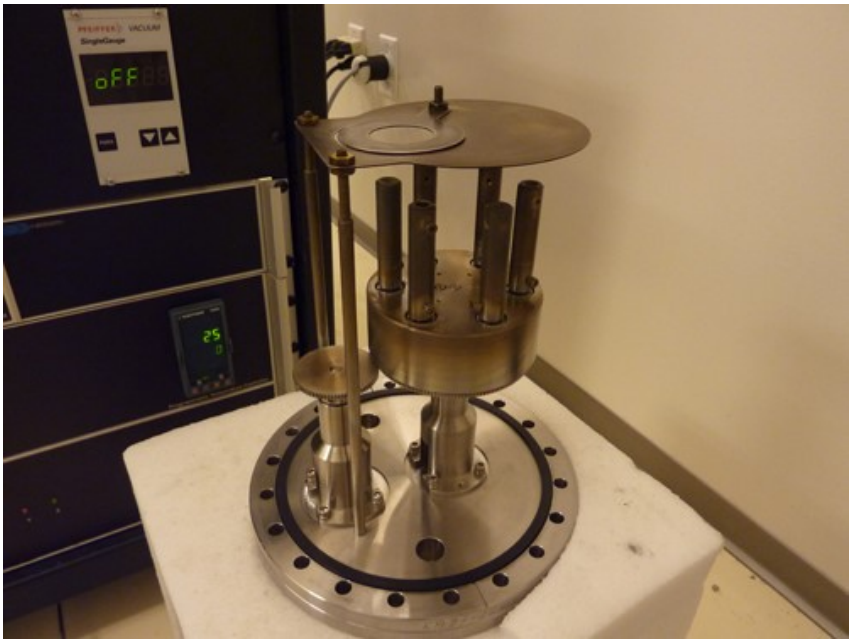

Figure B.2: Target flange

that replacing it should be done with care to ensure that it is secure and parallel to the heater coil. This is not mandatory for most samples.

3. Attach your samples to the substrate holder using clips. DO NOT OVERTIGHTEN THE SCREWS! Since you will be heating this assembly up to very high T, thermal expansion will degrade the screw threading and may make it impossible for you to remove the screws later.

4. Install the substrate holder by aligning the holes with the screws surrounding the substrate heater coil, and turning the substrate holder clockwise. Tighten the 4 screws gently and ensure the substrate holder is secure.

5. Install new target at a consistent height to ensure similar deposition each time. (The target needs to have a flat surface, so polishing the target is recommended.) Place the base of the ruler against the hole on the bottom of the flange, and align the top of the target to a certain height (e.g. the 20.35 mm mark). Changing the height of the target can greatly alter laser focus and deposition rate/time. Note that this height changes after each laser alignment.

6. After cleaning, polishing, and installing your new target, replace the flange and tighten the 4 screws with the wrench. Make sure that the rubber O-ring is placed properly. The screws should be spaced out evenly (with 4 screw-holes in between each screw). Reconnect X and Y cables

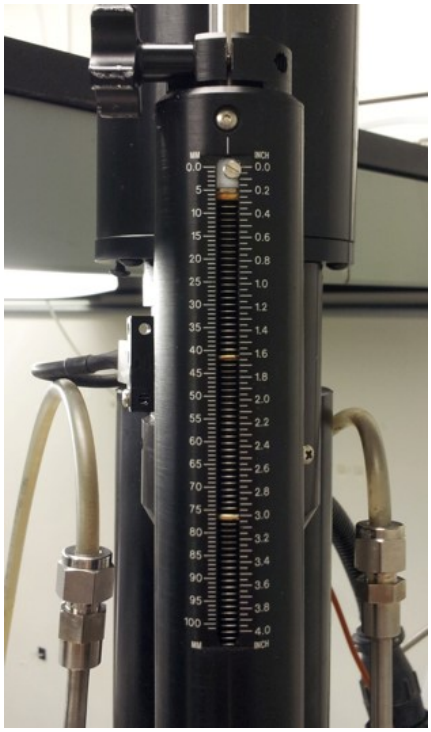

Figure B.3: Sample shutter

to the motors by aligning the grooves in the cable to the matching mark on the motor.

7. Lower the shutter to the 85 mark, making sure that it does not contact your sample holder clips.

8. On the panel, "Control Substrate Motor," press "Home/Enable," and then "Rotate at Constant Velocity," (e.g. 10 deg./s). Sometimes the sample holder will contact the shutter and knock down your samples. Stop the motor until you are ready for deposition.

9. Set motor controls (X for target carousel and Y for target) to rotate sample gently and ensure even deposition (see Figure 4). On the "Control Target Motors" panel on the left side, press "Home" to home the target carousel. Set the Desired Angle, Start Angle, Home Angle, and Velocity (e.g. 200 deg.; 195 deg.; 205 deg., 10 deg./s) and press "Raster." On the top right of the panel, press "Enable" and "Rotate," (e.g. 17 deg./s). Check that the motors work properly and stop them until you are ready for pre-ablation of the target. [Note: if the X motor decides to travel in the negative direction indefinitely during the homing sequence, try to gently adjust the electrical contact on the outside of the flange.]

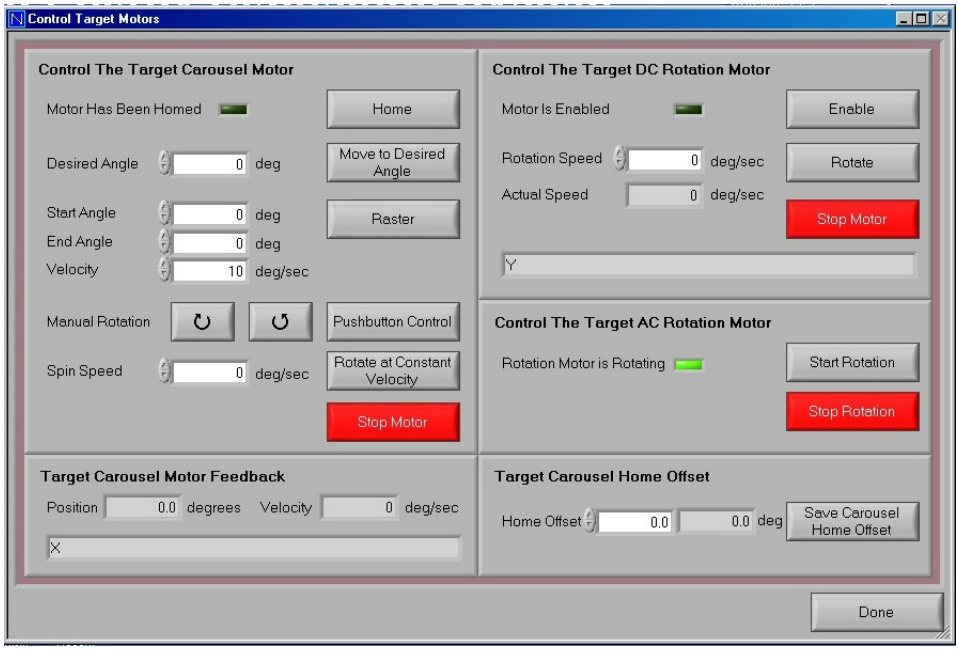

Figure B.4: Target motor control

B.2 Pumpdown

10. After the flange is closed and you are reasonably confident that the rubber O-ring is in place, pump down the chamber:

    (a) Open the gate valve fully (may hear a soft hiss as pressure equilibrates between turbo pump and chamber).

    (b) Turn on the mechanical pump and wait for the pressure to reach less than 1 Torr. (This is necessary only when using external backing pump; if using the diaphragm pump, proceed to next step).

    (c) Press the "Turbo-on" button on the Vacuum Control panel on the computer (Fig B.5).

11. The software automatically sets the target turbo Rotation Speed to the maximum 1000Hz. While this is meant to optimize pumpdown time, it puts a lot of stress on the turbo, since it has to operate at maximum power in order to deal with the large gas load at the beginning of pumpdown. It is best to **immediately lower the Rotation Speed to 300Hz** and wait for the pressure to stabilize before slowly increasing the Rotation Speed (such as in increments of 100Hz), up to about 600-700 Hz, if you need a lower base pressure. However, most users will not need to increase the speed above 600Hz, especially if you plan to flow gas during growth.

    It is very important to monitor the turbo Motor Current, located in the Pfeiffer Turbo Control window shown above. The maximum value is 3.8

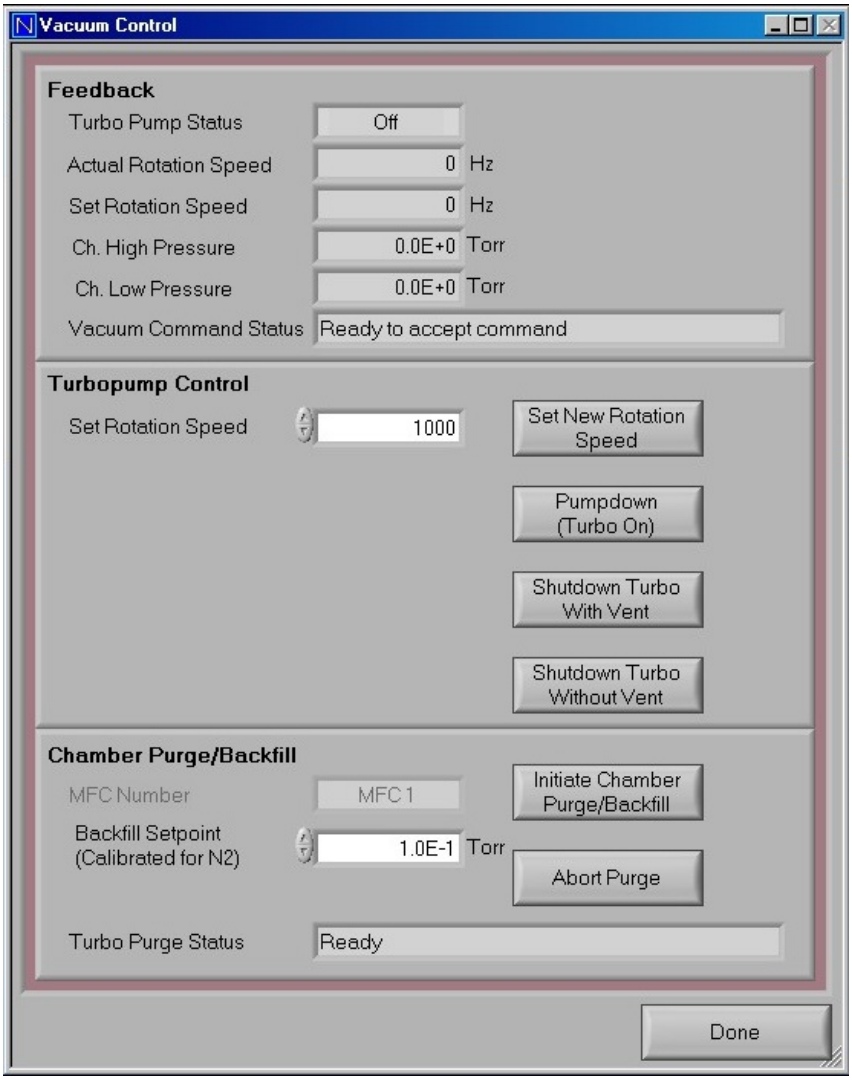

Figure B.5: Vacuum control

Amps, and the turbo should not be at the maximum value for extended periods of time. If it is, that means the gas load is too high and Rotation Speed has to be reduced. Please do not change any of the parameters in this window, it should only be used to monitor the turbo power.

12. Open the LN2 tank.

B.3 Pre-deposition

B.3.1 Temperature Control

13. Set the heating coil to your target temperature (e.g., 900 deg. C) at fixed ramp rate of 10 or 15 deg. C/min. For Control Type, make sure to

Figure B.6: Turbo control

select "Ramp Rate," and "deg/minute," not "deg/second". Press start to begin heating (see Figure B.7). Turn on the chiller.

B.3.2 Deposition pressure control

14. When heater temperature reaches your targeted value, reduce the turbo pump speed to 500Hz, if necessary, by entering "500" in "Set Rotation Speed" and pressing "Set New Rotation Speed" button in "Vacuum Control" (see Figure 2).

15. Wait until the actual turbo speed reaches 500 Hz.

16. Open the tank corresponding to your process gas and the valves associated with it.

17. Open "FINE" valve and control the deposition pressure by adjusting the manual flow meter (see Figure 1). DO NOT open "COARSE" or "VENT" valves. This will kill the turbo pump. Let the gas flow equilibrate. Remember not to put too much strain on the turbo. It is better to flow less gas and decrease the turbo rotation speed. Never flow gas if the turbo speed is above 600Hz.

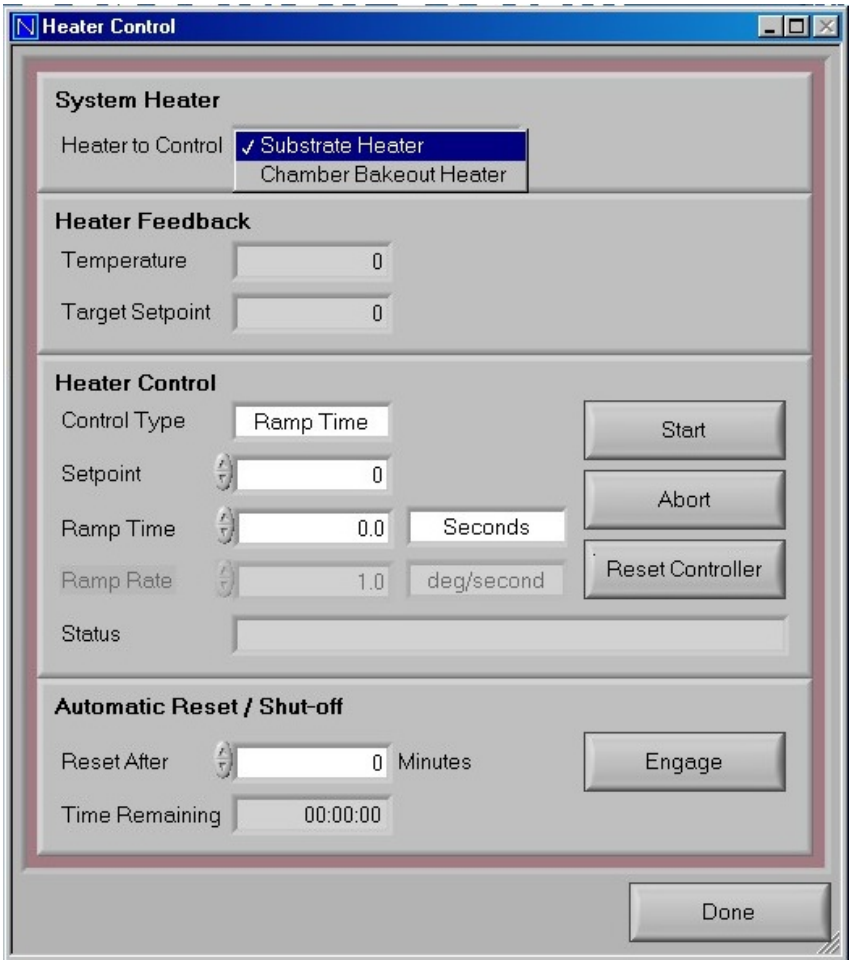

Figure B.7: Heater control

B.3.3 Laser warm-up

18. Inspect the laser and system to make sure that the plastic beam-path protection cage is closed and flush with the chamber and laser. No part of the beam path should be exposed. Make sure the laser shutter is closed and that the exhausts are connected and functioning properly.

19. Get a pair of Laser safety goggles with OD above 9 for UV wavelengths (248nm)

20. Turn on laser (switch, then key) and wait 5 min for the laser self-test to complete (make sure you are familiar with the Laser SOP before doing this).

21. There are 3 modes available for laser use: HV, EGY NGR, EGY PGR. HV mode (where the voltage is kept constant and energy may decrease as a function of time, is used only for aligning the laser and calibrating the energy meter (by users trained to do so). EGY NGR (constant

energy, gas not refilling automatically) mode should be used for depositions (up to several hours). EGY PGR mode is only used for systems under continuous operation, and here the laser will partially refill itself automatically to keep a constant energy output. DO NOT USE THIS MODE. This would require keeping the halogen mix tank open, and our lab is not safely equipped for that.

22. Check that the laser is programmed with the correct parameters for your deposition. Press "Trigger INT/EXT" and select "EXT" by arrow and hit "ENTER". (Now the computer controls the laser externally.) Press "MODE" and select "EGY NGR" by arrow and hit "ENTER". (Now it is under a constant energy mode.) Press "EGY" and enter a desired energy (e.g., 300 mJ) and hit "ENTER". (Now the output energy is set.) Press "REPRATE" and enter a desired rate (e.g., 1-20 Hz) and hit "ENTER". (Now the reprate rate is set.) Note that using a reprate above 15Hz, the laser cooling water must be on.

23. Press "RUN/STOP" and hit "EXE". (The laser will wait for a command from the computer.)

24. It is essential to first warm up the laser; this will ensure uniform pulse parameters. Make sure your laser safety goggles are on, and that the sample shutter is down and the laser shutter is closed. In the laser control window (Figure 6), run 100 pulses with a frequency of 1Hz; then run 100 pulses at 5Hz, and so on until you reach your desired pulse frequency and energy.

B.4 Pre-ablation & deposition

25. Start up the X and Y motors again. Enter a number of pulses and frequency in "Control Laser" and Press "Start Laser" button. Typical required number of pulses for laser pre-ablation to clean the target surface is 5000 to 10000.

26. When the pre-ablation is done, raise the sample shutter back to "0". Turn on the Substrate motor. Enter targeted number of pulses and frequency in "Control Laser" and press "Start Laser".

27. During the deposition, you'll need to monitor the chamber pressure and correct it by changing the flowmeter slightly, and sometimes the turbo rotation speed.

28. At the end of your deposition, close the laser shutter. Turn off laser: first press STOP on the keypad, then turn the key and then the circuit breaker switch.

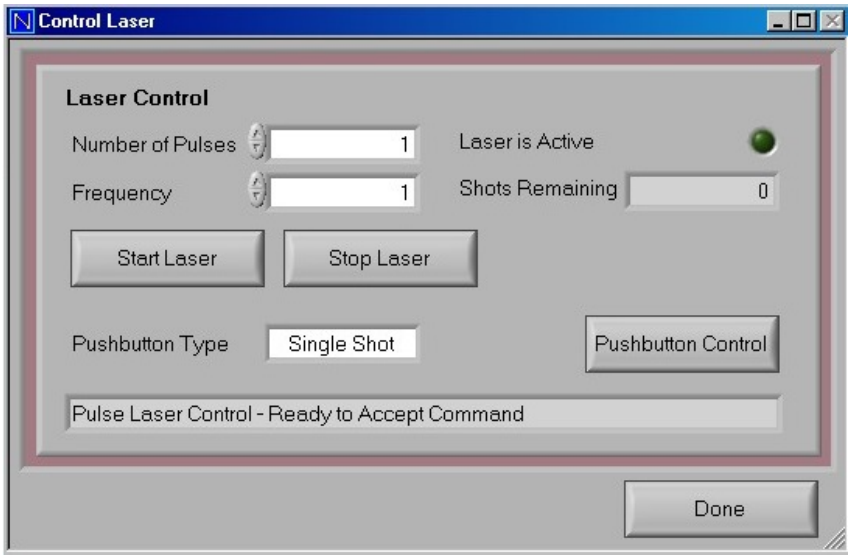

Figure B.8: Laser control

B.5 Annealing & Cooling Down

29. (If you need to anneal your film in a high partial pressure of oxygen:) Close the gate valve. Close "FINE" valve. Turn off the turbo pump by pressing "Shutdown Turbo Without Vent" from "Vacuum Control" in the computer (see Figure 2). Increase the chamber pressure to 100 Torr of oxygen by opening "COARSE" valve. Wait 20 min to oxidize your films.

30. Set heating coil temperature to zero at ramp rate of 10 deg.C/min. Press start to begin cooling (see Figure 5). (Alternatively you can use a script which will wait 20 minutes and automatically begin cooling down).

31. If you don't need to anneal your film after deposition, you can proceed to the next step once your sample has cooled down.

B.6 Venting

32. Make sure the gate valve connecting the turbo pump to the chamber is closed (clockwise to close, also check indicator pin). Press "Shutdown Turbo Without Vent" from "Vacuum Control" in the computer (see Figure 2). DO NOT use "Shutdown Turbo with Vent".

33. Once the turbo has reached a speed below 400 Hz, turn off the mechanical pump. [Note: this is applicable when not using the normal diaphragm backing pump which is part of the pumping station].

34. Unplug the cables attached to the X and Y motors on the flange which supports the target carousel. Loosen the screws on this flange to avoid overpressurization. (Make sure that the gate valve is now closed!) Open the "Vent" valve to backfill the chamber with nitrogen. When the pressure in the chamber reaches 700 Torr (see convectron gauge in Figure 1), close the vent valve so you don't pressurize the chamber.

35. Placing your arm under the motors and one hand on the bottom of the flange, gently pop off the flange to break vacuum and slowly remove the flange/carousel apparatus. Place the flange in the Styrofoam holder on the floor (see Figure 3). Make sure not to damage electrical ports and connections on the outside of the flange.

36. Close LN2 tank and turn off water chiller when you are finished.

B.7 Note

Between your depositions, you should monitor the cleanliness of the window through which the laser must pass to hit your target. If the rectangular "spot" gets too thick, you will lose intensity and focus. Clean the laser window with diamond paste roughly every 100k-200k pulses.

B.8 Laser Refill Procedure

The laser gas has a dynamic and static lifetime. The dynamic lifetime corresponds to the maximum number of pulses that can be generated by a given quantity of laser gas; this number is on the order of 25 million pulses. The static lifetime corresponds to the time the gas can stay inside the laser cavity before decomposing; this is typically between 1 and 2 weeks.

1. Check that the laser is on and ready to go. Ensure that all exhaust is connected and operating (gas roughing pump, gas cabinets).

2. Open the premix and He tanks in the gas cabinet. Ensure all the proper valves are open, and all others are closed (that the He connection to the premix tank is closed). You can check this by following the gas lines.

3. First, flush the He line (the inert gas in this case). Flushing the line evacuates gas inside the line using the roughing pump under the laser. On the laser keypad, press FLUSH LINE → INERT → ENTER → EXE (do this 3 times).

4. Next, flush the buffer gas (F premix) line. On the laser keypad, press FLUSH LINE → BUFFER → ENTER → EXE (do this 3 times). IF YOU SMELL ANY GAS (F2), IMMEDIATELY CLOSE THE TANKS

AND CONTACT THE STUDENT SAFETY OFFICERS. Do not continue. Follow emergency guidelines.

5. Start the refill process where the mechanical pump will first pump out the laser cavity and then refill it with a fresh buffer. On the laser keypad, press NEW FILL → ENTER → EXE.

6. Once the refill has finished, close the premix tank. NOTE: the process should complete within 15 minutes. If the refill doesn't stop automatically, and the pressure is not increasing anymore, press BREAK on the control pad.

7. Now it is important to purge the buffer line so that no premix remains there. "Purge" will evacuate the gas in the line using the vacuum pump and then refill the line with the inert gas (He). On the laser keypad, press PURGE LINE → BUFFER → ENTER → EXE (3 times). Close the He tank and all valves associated with the tanks inside the cabinet.

8. The laser is now ready to use. Note the date and laser tube pressure (3320mbar) in the Log book.

B.9 LN2 tank

We have a special fitting on our LN2 tank that allows us to use the boil-off as the source (this is great for low pressure requirements). When you refill the tank, make sure you for THE SAME TANK so we don't lose that fitting.

Bibliography

[1] A. E. Rakhshani. Preparation, characteristics and photovoltaic properties of cuprous oxide - a review. *Solid-State Electronics*, 29(1):7–17, 1986.

[2] S. S. Wilson. *Zn-VI/Cu_2O Heterojunctions for Earth-Abundant Photovoltaics*. PhD thesis, California Institute of Technology, 2015.

[3] J. Xue and R. Dieckmann. The High-Temperature Phase Diagram of the Cu - O System in Stability Region of Cuprous Oxide. *High Temperatures - High Pressures*, 249(3):271–284, 1992.

[4] L. C. Olsen, F. W. Addis, and W. Miller. Experimental and theoretical studies of Cu_2O solar cells. *Solar Cells*, 7(3):247–279, 1982.

[5] F. Biccari. *Defects and Doping in Cu_2O*. PhD thesis, University of Rome, 2009.

[6] Jr. M. W. Chase, C. A. Davies, Jr. J. R. Downey, D. J. Frurip, R. A. McDonald, and A. N. Syverud. NIST-JANAF thermochemical tables. http://kinetics.nist.gov/janaf/janbanr.html, 1986.

[7] S. S. Wilson, J. P. Bosco, Y. Tolstova, D. O. Scanlon, G. W. Watson, and H. A. Atwater. Interface stoichiometry control to improve device voltage and modify band alignment in ZnO/Cu_2O heterojunction solar cells. *Energy and Environmental Science*, 7(11):3606–3610, 2014.

[8] T. Minami, Y. Nishi, and T. Miyata. Heterojunction solar cell with 6% efficiency based on an n-type aluminum–gallium–oxide thin film and p-type sodium-doped Cu_2O sheet. *Applied Physics Express*, 8(2):022301, 2015.

[9] T. Minami, Y. Nishi, and T. Miyata. High-Efficiency Cu_2O-based heterojunction solar cells fabricated using a Ga_2O_3 thin film as n-type layer. *Applied Physics Express*, 6(4):044101, 2013.

[10] Y. S. Lee, D. Chua, R. E. Brandt, S. C. Siah, J. V. Li, J. P. Mailoa, S. W. Lee, R. G. Gordon, and T. Buonassisi. Atomic layer deposited gallium oxide buffer layer enables 1.2 V open-circuit voltage in cuprous oxide solar cells. *Advanced Materials*, 26(27):4704–4710, 2014.

[11] R. E. Brandt, M. Young, H. H. Park, A. Dameron, D. Chua, Y. S. Lee, G. Teeter, R. G. Gordon, and T. Buonassisi. Band offsets of n-type electron-selective contacts on cuprous oxide (Cu2O) for photovoltaics. *Applied Physics Letters*, 105(26):263901, 2014.

[12] W. Niu, M. Zhou, Z. Ye, and L. Zhu. Photoresponse enhancement of Cu_2O solar cell with sulfur-doped ZnO buffer layer to mediate the interfacial band alignment. *Solar Energy Materials and Solar Cells*, 144:717–723, 2016.

[13] T. Minami, Y. Nishi, and T. Miyata. Efficiency enhancement using a $zn_{1-x}ge_xo$ thin film as an n-type window layer in cu_2o-based heterojunction solar cells. *Applied Physics Express*, 9(5):052301, 2016.

[14] R. Scheer and H. W. Schock. *Chalcogenide Photovoltaics: Physics, Technologies, and Thin Film Devices*. Wiley-VCH, 2011.

[15] A. Klein. Energy band alignment in chalcogenide thin film solar cells from photoelectron spectroscopy. *Journal of Condensed Matter Physics*, 27:134201, 2015.

[16] Clas Persson, Charlotte Platzer-Björkman, Jonas Malmström, Tobias Törndahl, and Marika Edoff. Strong valence-band offset bowing of $zno_{1-x}s_x$ enhances p-type nitrogen doping of zno-like alloys. *Phys. Rev. Lett.*, 97:146403, 2006.

[17] M. A. Herman, W. Richter, and H. Sitter. *Epitaxy: Physical Principles and Technical Implementation*. Springer-Verlag, Berlin, 2004.

[18] U. W. Pohl. *Epitaxy of Semiconductors*. Springer-Verlag, Berlin, 2013.

[19] J. A. Venables. *Introduction to Surface and Thin Film Processes*. Cambridge University Press, Cambridge, UK, 2000.

[20] J. E. Ayers. *Heteroepitaxy of Semiconductors*. CRC Press, New York, 2007.

[21] D. L. Smith. *Thin Film Deposition: Principles and Practice*. McGraw-Hill, New York, 1995.

[22] R. T. Brewer. *Quantitative biaxial texture analysis with reflection high-energy electron diffraction for ion beam-assisted deposition of MgO and heteroepitaxy of perovskite ferroelectrics*. PhD thesis, California Institute of Technology, 2004. http://resolver.caltech.edu/CaltechETD:etd-08182003-150957.

[23] T. P. White, N. N. Lal, and K. R. Catchpole. Tandem solar cells based on high-efficiency c-Si bottom cells: top cell requirements for >30% efficiency. *IEEE Journal of Photovoltaics*, 4(1):208–214, 2014.

[24] K. Kawaguchi, R. Kita, M. Nishiyama, and T. Morishita. Molecular beam epitaxy growth of CuO and Cu_2O films with controlling the oxygen content by the flux ratio of Cu/O^+. *Journal of Crystal Growth*, 143(3):221–226, 1994.

[25] D. S. Darvish and H. A. Atwater. Epitaxial growth of Cu_2O and ZnO/Cu_2O thin films on MgO by plasma-assisted molecular beam epitaxy. *Journal of Crystal Growth*, 319(1):39–43, 2011.

[26] J. Li, Z. Mei, D. Ye, H. Liang, Y. Liu, and X. Du. Growth of single-crystalline Cu_2O (111) film on ultrathin MgO modified α-Al_2O_3 (0001) substrate by molecular beam epitaxy. *Journal of Crystal Growth*, 353(1):63–67, 2012.

[27] Z. G. Yin, H. T. Zhang, D. M. Goodner, M. J. Bedzyk, R. P. H. Chang, Y. Sun, and J. B. Ketterson. Two-dimensional growth of continuous Cu_2O thin films by magnetron sputtering. *Applied Physics Letters*, 86(6):061901, 2005.

[28] K. Matsuzaki, K. Nomura, H. Yanagi, T. Kamiya, M. Hirano, and H. Hosono. Epitaxial growth of high mobility Cu_2O thin films and

application to p-channel thin film transistor. *Applied Physics Letters*, 93(20):202107, 2008.

[29] A. Soon, M. Todorova, B. Delley, and C. Stampfl. Thermodynamic stability and structure of copper oxide surfaces: A first-principles investigation. *Physical Review B*, 75(12):125420, 2007.

[30] W. Seiler, E. Millon, J. Perrière, R. Benzerga, and C. Boulmer-Leborgne. Epitaxial growth of copper oxide films by reactive cross-beam pulsed-laser deposition. *Journal of Crystal Growth*, 311(12):3352–3358, 2009.

[31] Y. Fu, H. Lei, X. Wang, D. Yan, L. Cao, G. Yao, C. Shen, L. Peng, Y. Zhao, Y. Wang, and W. Wu. Fabrication of two domain Cu_2O (011) films on MgO (001) by pulsed laser deposition. *Applied Surface Science*, 273(12):19–23, 2013.

[32] A. Ichimiya and P. I. Cohen. *Reflection High Energy Electron Diffraction*. Cambridge University Press, Cambridge, UK, 2004.

[33] V. E. Heinrich and P. A. Cox. *The Surface Science of Metal Oxides*. Cambridge University Press, New York, 1994.

[34] C. Gatel, P. Baules, and E. Snoeck. Morphology of Pt islands grown on MgO(001). *Journal of Crystal Growth*, 252(1-3):424–432, 2003.

[35] J. Galipaud, C. Roy, M. H. Martin, S. Garbarino, L. Roue, and D. Guay. Electrooxidation of ammonia at tuned (100)Pt surfaces by using epitaxial thin films. *ChemElectroChem*, 2(8):1187–1198, 2015.

[36] R. T. Brewer and H. A. Atwater. Rapid biaxial texture development during nucleation of MgO thin films during ion beam-assisted deposition. *Applied Physics Letters*, 80(18):3388–3390, 2002.

[37] C. T. Campbell. Ultrathin metal films and particles on oxide surfaces: Structural, electronic and chemisorptive properties. *Surface Science Reports*, 27(1-3):1–111, 1997.

[38] P. C. McIntyre, C. J. Maggiore, and M. Nastasi. Epitaxy of Pt thin films on (001)MgO-II: Orientation evolution from nucleation through coalescence. *Acta Materialia*, 45(2):1–111, 1997.

[39] J. Olander, R. Lazzari, J. Jupille, B. Mangili, J. Goniakowski, and G. Renaud. Size- and temperature-dependent epitaxy for a strong film-substrate mismatch: The case of Pt/MgO(001). *Physical Review B*, 76(7):075409, 2007.

[40] G. R. Harp and S. S. P. Parkin. Epitaxial growth of metals by sputter deposition. *Thin Solid Films*, 288(1-2):315–324, 1996.

[41] B. M. Lairson, M. R. Visokay, R. Sinclair, S. Hagstrom, and B. M. Clemens. Epitaxial Pt(001), Pt(110), and Pt(111) films on MgO(001), MgO(110), MgO(111), and Al_2O_3(0001). *Applied Physics Letters*, 61(12):1390–1392, 1992.

[42] B. Gilles, A. Marty, and J. Eymery. Molecular beam epitaxial growth of Au (110) layers on MgO (110) substrates. *Applied Physics Letters*, 68(2):203–207, 1993.

[43] J. M. Cowley and K. D. Neumann. The alignment of gold particles on MgO crystal faces. *Surface Science*, 145(2-3):301–312, 1984.

[44] H. Sato and S. Shinozaki. Morphology of nuclei and epitaxial behavior of Au and Ag on MgO. *Journal of Vacuum Science and Technology*, 8(1):159–163, 1971.

[45] M. Xue, J. Guo, and Q. Guo. Effect of polar surface on the growth of Au. *RSC Advances*, 5(15):11109–11114, 2015.

[46] B. N. Chapman. *Glow Discharge Processes: Sputtering and Plasma Etching*. John Wiley & Sons, New York, 1980.

[47] J. E. Mahan. *Physical Vapor Deposition of Thin Films*. John Wiley & Sons, New York, 2000.

[48] E. H. Kennard. *Kinetic Theory of Gases*. McGraw-Hill, New York, 1938.

[49] S. S. Perry and P. B. Merrill. Preparation and Characterization of MgO (100) surfaces. *Surface Science*, 383:268–276, 1997.

[50] C. Mariéchal, E. Lacaze, W. Seiler, and J. Perrière. Growth mechanisms of laser deposited BiSrCaCuO films on MgO substrates. *Physica C*, 294(1-2):23–32, 1998.

[51] K. H. Ahn, S. Baik, and S. S. Kim. Change of growth orientation in Pt films epitaxially grown on MgO (001) substrates by sputtering. *Journal of Materials Research*, 17(9):2334–2338, 2002.

[52] T. Abe, B. Sundman, and H. Onodera. Thermodynamic Assessment of the Cu-Pt System. *Journal of Phase Equilibria and Diffusion*, 26:5–13, 2006.

[53] W. Cao, Y. A. Chang, J. Zhu, S. Chen, and W. A. Oates. Thermodynamic modeling of the Cu-Ag-Au system using the cluster/site approximation. *Intermetallics*, 15:1438–1446, 2007.

[54] A. Grimm, J. Just, D. Kieven, I. Lauermann, J. Palm, A. Neisser, T. Risson, and R. Klenk. Sputtered Zn(O,S) for junction formation in chalcopyrite-based thin film solar cells. *Physica Status Solidi RRL*, 4:109–111, 2010.

[55] S. S. Hegedus and W. N. Shafarman. Thin-film solar cells: device measurements and analysis. *Progress in Photovoltaics: Research and Applications*, 12:155–176, 2014.

[56] B. R. Strohmeier and D. M. Hercules. Surface spectroscopic characterization of the interaction between zinc ions and γ-alumina. *Journal of Catalysis*, 86:266–279, 1984.

[57] National Institute of Standards and Technology. NIST X-ray Photoelectron Spectroscopy Database, Version 4.1. http://srdata.nist.gov/xps/, 2012.

[58] M. Yamaguchi, A. Yamamoto, and Y. Itoh. Effect of dislocations on the efficiency of thin-film GaAs solar cells on Si substrates. *Journal of Applied Physics*, 59:1751–1753, 1986.